Functional Connectivity in Nonhuman Primate Brain Using Blood Oxygenation Level-Dependent Functional Magnetic Resonance Imaging and Electrophysiology

By
Zhaoyue Shi

Dissertation
Submitted to the Faculty of the
Graduate School of Vanderbilt University
in partial fulfillment of the requirements
for the degree of
DOCTOR OF PHILOSOPHY
in
Biomedical Engineering

December 16, 2017
Nashville, Tennessee

Approved:
John C. Gore, Ph.D.
Li Min Chen, M.D., Ph.D.
Adam W. Anderson, Ph.D.
D. Mitchell Wilkes, Ph.D.
Baxter P. Rogers, Ph.D.

ACKNOWLEDGEMENTS

First, I would like to start by thanking my amazing advisor Dr. John Gore for all the research guidance, support, encouragement for pursuing science, and the brilliant insights he provided over the past four years. My Ph.D. journey, contributions to the science community and great passion towards research would not have been possible without his strong leadership and remarkable mind. I sincerely appreciate that he provided me with the best working equipment, full technical support, and supported me to present research in various conferences, which truly opened my eyes on world-wide science progresses and made my research life so much more interesting. I also truly appreciate his efforts in guiding my research and preparing me to become an independent researcher with the great desire for innovative ideas. His brilliance, confidence, modesty, kindness, amazing writing and talking skills always inspired me to explore my potential and improve myself in every aspect. He is absolutely a visionary, the best mentor I could have ever asked for, and I will forever be grateful for his mentorship.

Second I would like to give my great thank you to Dr. Li Min Chen for all the valuable neuroscience perspective, guidance, and great manuscript editing. It was her frequent advice that provided me the raw material I needed to learn. I would also like to thank Dr. Mitch Wilkes, who thoroughly taught me signal processing. He is born to be an amazing teacher and an awesome professor, I feel so fortunate to have learned from him. I additionally would like to thank Dr. Adam Anderson and Dr. Baxter Rogers for serving in my committee, and providing significant insights into my studies. I want to offer a special thank you to Dr. Victoria Morgan, whose brilliant human studies inspired me to further translate my pre-clinical research to valuable clinical applications. I would specifically like to thank John Nguyen, Jennifer Watchmaker, Samantha By, Zachary Stark, Paula Trujillo, Tung-Lin Wu, Kurt Schilling, Feng Wang and Hua Li for graduate school happiness and joy. My ultimate thank you is to Nancy Hagans. Vanderbilt University Institute of Imaging Science could not go on without her.

Finally, I would like to thank my family for always being there for me. I am so blessed to have their unconditional support and love. I am looking forward to my next journey.

TABLE OF CONTENTS

LIST OF TABLES

Table Page

LIST OF FIGURES

Figure Page

CHAPTER I

INTRODUCTION

The motivation of this dissertation is to evaluate the spatial correspondence between functional magnetic resonance imaging (fMRI) signals and their underlying neural activity in both stimulation and resting state conditions, and to investigate the dynamics of brain functional connectivity in both fMRI and electrophysiological signals.

FMRI is well established as a neuroimaging technique for detecting and delineating regions in the brain that change their levels of activity in response to specific experimental conditions. In addition, the identification of patterns of highly correlated low frequency fMRI signals in resting states potentially provides a powerful approach to assess neural circuits and brain functional organization, in which distributed brain regions work together to achieve different functions. However, fMRI studies rely on detecting hemodynamic changes as revealed by blood oxygenation level-dependent (BOLD) signals to infer underlying local neuronal activity, and these are indirect indicators of neuronal activity. Precise interpretations of fMRI studies require a better understanding of the quantitative relationships between BOLD signal changes and their corresponding electrophysiological signatures. Local field potentials (LFPs) are electrophysiological signals generated by the summed electric currents flowing from a population of nearby neurons within a small volume of the brain around a recording electrode tip. Several previous studies have confirmed that fMRI signals are temporally reliable indicators of associated LFPs. However, no previous study has directly compared the spatial distributions of BOLD and LFP signals in both information processing and their correlation profiles in a resting state. Moreover, LFPs themselves are complex in nature and have specific spectral properties of functional significance. Therefore, this thesis compares the extents and locations of activations and the local correlation profiles between frequency-specific LFPs and submillimeter resolution BOLD at 9.4T within primary somatosensory (S1) cortex in individual monkeys.

Variations over time in resting state correlations in BOLD signals from different cortical areas may indicate changes in brain functional connectivity. Recently, there has been an increasing interest in the detection and characterization of possible dynamic changes in fMRI functional connectivity. However, apparent variations over time may also arise from stationary signals when the sample duration is finite. To identify possible temporal dynamic changes in functional

connectivity, in this thesis, a filtered stationary model and a nonstationary dynamic model were developed to simulate real fMRI functional correlations, and simulated results were compared with the behavior of S1 networks in anesthetized squirrel monkeys at high field (9.4 T), using a sliding window correlation analysis.

Finally, broad band electrophysiological signals most likely reflect contributions of several different neural processing pathways, and are traditionally decomposed and interpreted in the frequency domain. To evaluate the differences in dynamic patterns between fMRI and frequency-specific LFP (delta, theta, alpha, beta, gamma low, gamma high and gamma very high bands) functional connectivity, the time-varying probability distributions between both modalities were quantitatively compared, using a sliding window correlation technique and a Markov chain model-based approach.

Basic Principles of Magnetic Resonance Imaging

Magnetic resonance imaging utilizes the phenomenon of nuclear magnetic resonance (NMR) which was first detected in liquids by Felix Bloch and Edward Purcell [Purcell et al., 1945; Bloch and Hansen, 1946]. In 1973, Lauterbur produced the first MR images of small test tube samples of water by using magnetic field gradients to link spatial position to the NMR frequency [Lauterbur, 1973]. This led to the rapid development of larger imaging systems capable of imaging human subjects. Today, MRI is the main noninvasive imaging method used for studying the human brain.

MRI detects the NMR signals from hydrogen nuclei (protons) mainly contained in water molecules in tissues. Each proton has a small magnetic moment and in the presence of an applied magnetic field they tend to align with the field, which produces a net macroscopic magnetization in the body. MRI maps this net magnetization within a section of the sample.

Nuclear magnetization

Biological tissues are approximately 70 - 80% water [Altman and Dittner, 1964] so they contain a large number of hydrogen protons (pure water is $\approx$ 110 Molar in H nuclei). In the absence of a magnetic field, the magnetic moments of the protons are randomly oriented, so there is no net magnetization.

As many have described [Suetens et al., 2009; Huettel et al., 2004; Brown and Semelka, 2003; McRobbie et al., 2008; NessAiver, 1996; Bushberg and Boone, 2011], hydrogen protons are nuclei with angular momentum or spin = ½, and quantum rules determine that there are only 2 energy levels allowed in the presence of an applied magnetic field, corresponding to spin UP (aligned) and DOWN. The spin UP level is the lowest energy state, so the majority of protons occupy this level which produces a net magnetization along the external magnetic field direction. The direction of the net magnetization in equilibrium is usually termed the z-component or longitudinal component. In a voxel, the net magnetization M_0 is proportional to the number of spins in that voxel. In order to measure the magnetization, a radiofrequency (RF) field at a precise frequency is used to tip the vector to produce a transverse component. The RF frequency is calculated using the Larmor equation (Eq. (1))

$$\omega_{RF} = \gamma B_0 \qquad \text{Eq. (1)}$$

where ω_{RF} is the resonance frequency, and B_0 is the external magnetic field. The RF pulse is applied to excite the nuclei to a higher energy level. The transverse component is the net sum of nuclei which have angular momentum and so their net magnetization rotates about the main field direction. When the RF pulse is removed, the nuclei go back to their original states and the system returns to equilibrium. The transverse component of magnetization decays to zero, and the longitudinal component returns towards the original state before the application of the RF pulse, M_0. This process of the system returning to equilibrium is called relaxation.

Return to dynamic equilibrium: relaxation

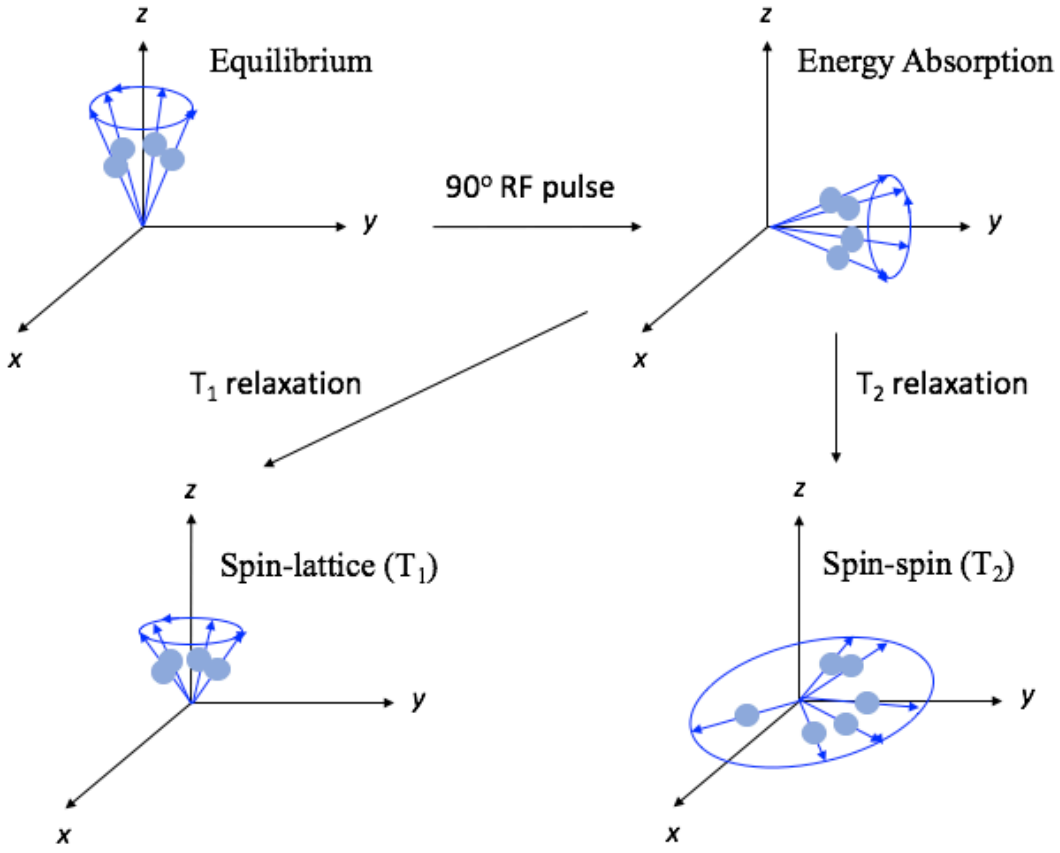

Figure 1 Schematic overview of an MRI relaxation with a 90° RF pulse. The RF pulse generates the transverse component of the net magnetization due to energy absorption. After removing the RF pulse, relaxation of T_1 in the longitudinal direction and T_2 in transverse plane returns the system to equilibrium. Figure adapted from Suetens, 2009.

The drop in the transverse component of the net magnetization vector is caused by the spin-spin relaxation phenomenon as presented in Figure 1. In practice, the spins rotate in phase at the end of the application of the RF pulse, but then gradually, each may experience a slightly different magnetic field and therefore rotate at different angular frequencies. This causes a decrease of the net transverse component magnetization $M_{xy}(t)$ with time constant T_2

$$M_{xy}(t) = M_0\, e^{-t/T2} \qquad \text{Eq. (2)}$$

As many have described, T_2 is the transverse relaxation time required for the transverse component of M_{xy} to decay to 37% of its initial value, and M_0 represents the equilibrium net magnetization immediately before the RF pulse [Brown and Semelka, 2003; Huettel et al., 2004; Suetens, 2009]. The T_2 value depends on the molecular interactions of water in the sample and is highly variable between different tissue types and for different external magnetic field strengths [Wansapura et al., 1999; Barth and Moser, 1997; Meyer et al., 1995; van Zijl et al., 1998; Ogawa et al., 1993a; Yacoub et al., 2001; Lee et al., 1999]. In practice, the main magnetic field that is applied to the tissue sample is inhomogeneous, therefore the transverse component of the net magnetization is dependent on both the T_2 relaxation and the field inhomogeneity. As mentioned in Haacke et al. [1989] and Chavhan et al. [2009], T_2^* is shorter than T_2, and can be defined using Eq. (3):

$$\frac{1}{T2*} = \frac{1}{T2} + \frac{1}{T2'} \qquad \text{Eq. (3)}$$

where $1/T_2' = \gamma \Delta B_i$ represents the relaxation rate contribution attributable to field inhomogeneities across an imaging voxel. As will be discussed later, functional brain imaging relies on detecting changes in the decay constant T_2^* caused by neural activity.

The rate of recovery of the longitudinal component is slower and occurs with a time constant T_1. The behavior of the magnetization after an RF pulse is described by a set of equations first proposed by Bloch [Bloch and Hansen, 1946] and these can be solved to produce expressions for the magnetization as a function of time. T_1 is also a property that varies considerably depending on tissue composition and the external magnetic field strength.

MRI signal detection

As described by Huettel et al. [2004] and Suetens et al., [2009], as the magnetization rotates, currents are induced in conductors near the sample and can be digitized for detection as signals. Specifically, RF coils around a sample can detect the signals $s_x(t)$ and $s_y(t)$ that are produced by the rotating transverse component of the net magnetization following a 90° RF pulse:

$$s_x(t) = M_0 e^{-t/T2} \cos(\omega_0 t) \quad \text{Eq. (4)}$$

$$s_y(t) = M_0 e^{-t/T2} \sin(\omega_0 t) \quad \text{Eq. (5)}$$

If the RF pulse is repeated after a repetition time, TR, the longitudinal component of the net magnetization vector would have already been recovered to a value as described in Eq. (6):

$$M_z(TR) = M_0 (1 - e^{-TR/T1}) \quad \text{Eq. (6)}$$

If the RF pulse is repeated after a repetition time, TR, the longitudinal component of the net magnetization vector may not be fully recovered so the starting magnetization is reduced. The Bloch equations then predict that the detected signal becomes

$$s(t) = M_0 (1 - e^{-TR/T1}) e^{-t/T2} \quad \text{Eq. (7)}$$

[Bloch and Hansen, 1946]. This signal depends on the spin density and relaxation times but provides no information on spatial locations. Imaging requires the use of magnetic field gradients as originally proposed by Lauterbur [Lauterbur, 1973].

Spatial information in MRI

In MRI, a strong and static magnetic field B_0 is used to align the nuclei, and gradient magnetic fields are applied to spatially map their locations. This includes selecting a slice and encoding the nuclei locations within the selected slice. To select a slice of interest that is perpendicular to the z-axis, a gradient magnetic field, G_z, that varies with z in a linear fashion is superimposed onto the main magnetic field, B_0. For small flip angles, the slice profile of magnetization is approximately determined by the Fourier Transform of the RF pulse envelope [Haacke et al., 1999; Berstein et al., 2004]. In order to obtain a rectangular slice profile, the RF pulse must therefore be a sinc function. However, in practice, this is impossible due to the infinite extent of a true sinc function. For this reason, the sinc function is truncated and is thus not perfect. Note that if the center frequency of the RF pulse is changed, then a slice at a different spatial location would be selected.

After exciting the nuclei in a slice, additional gradients $G_x(t)$ and $G_y(t)$ are applied for short times to map the signal locations within the plane. These additional gradients affect the signal and can therefore be used to encode x and y location information. Each gradient affects the signal frequency and phase at each location. The total signal, S(t), acquired from a selected slice after removing the RF pulse is then given by equation 8 [Huettel et al., 2004]:

$$S(t) = \int_x \int_y M(x,y) e^{-i\gamma \int_0^t (Gx(\tau)x + Gy(\tau)y)d\tau} dxdy \qquad \text{Eq. (8)}$$

The signal depends on the gradient amplitudes and their duration. Eq. (8) may be rewritten in a different notation scheme named k-space [Ljunggren, 1983; Twieg, 1983] as described with Eq. (9) and Eq. (10) [Huettel et al., 2004]:

$$k_x(t) = \frac{\gamma}{2\pi} \int_0^t G_x(\tau) d\tau \qquad \text{Eq. (9)}$$

$$k_y(t) = \frac{\gamma}{2\pi} \int_0^t G_y(\tau) d\tau \qquad \text{Eq. (10)}$$

$$S(t) = \int_x \int_y M(x,y) e^{-i2\pi Kx(t)x} e^{-i2\pi Ky(t)y} dxdy \qquad \text{Eq. (11)}$$

Eq. (11) indicates that the MRI signals are detected in k-space as a function of the gradient amplitudes and durations, and k space and MR image space are 2D Fourier transforms of each other. MR images may be reconstructed by inverse Fourier Transform of the measured k-space data acquired for different gradient waveforms [Twieg, 1983].

As described by Brown and Semelka [2003], in a practical study, a gradient magnetic field running along one of the two in-plane dimensions of the slice (e.g. x) is perpendicularly applied to the slice direction during the acquisitions of the signal in order to encode the spin location at that direction via the magnitude of the readout signals and their specific frequencies. The third dimension of the image is encoded by applying another gradient magnetic field that is perpendicular to both the slice selection gradient and the readout gradient. This is known as the phase encoding gradient magnetic field and is applied before signal sampling in the presence of the frequency encoding gradient. In a 2D imaging sequence, the phase encoding gradient is the only gradient that changes magnetic field strength during the data acquisition loop, where the MR images are acquired through continual excitation and signal detection at multiple time points with their own phase encoding gradient amplitude. These signals are each spatially encoded based on their distance from the iso-center of the scanner. The closer the signal is to iso-center, the smaller the incremental phase change will be when comparing signals acquired in each of the phase encoding gradient magnetic fields. Conversely, the further the signal is to iso-center, the absolute magnitude change in the applied gradient magnetic field will be greater.

Pulse sequences

MRI provides images based on the contrast between tissues. These contrast differences are highly dependent on the applied pulse sequences. For example, in the commonly used spin echo (SE) pulse sequence, an 180^{o} refocusing pulse is applied symmetrically in between an excitation RF pulse and signal acquisition (Figure 2). The effect of the 180^{o} pulse is to partially reverse some of the dephasing caused by field inhomogeneities and to produce a spin echo [Haacke et al., 1999; Brown and Semelka, 2003].

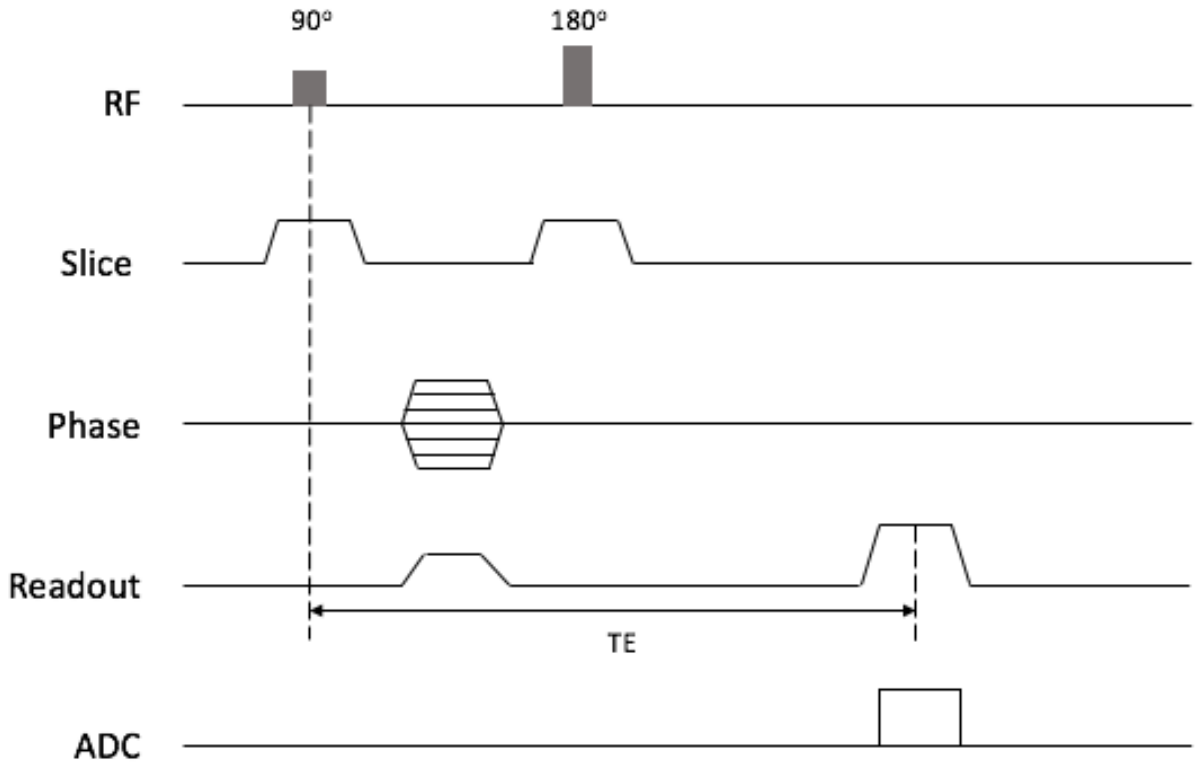

Figure 2 Spin echo sequence timing diagram in a single echo. The RF pulses consist of an excitation pulse and a 180° refocusing pulse. The sequence also contains a regular slice selection gradient field, phase encoding and frequency encoding gradient magnetic fields. The 180° refocusing pulse is applied halfway in between an excitation RF pulse and the echo formation. Figure adapted from Brown and Semelka, 2003.

Another widely used sequence is a gradient echo sequence (Figure 3). A frequency encoding gradient is applied for a short time to cause the transverse magnetization to decay as nuclei dephase, but this dephasing can be reversed by applying the same gradient in the opposite sense to rephase the signal [Elster, 1993; Haacke et al., 1999; Brown and Semelka, 2003]. Each acquisition sequence can be rapidly repeated if the flip angles produced by the excitation RF pulses are much less than 90° [Winker et al., 1988].

In a gradient echo sequence, the time to acquire the image after the RF pulse, TE, is determined by when the gradient pulses have equal area which determines the amount of T_2^* weighting. The amount of T_1 weighting depends on both the flip angle caused by the excitation RF pulse and the TR [Haacke et al., 1999; Brown and Semelka, 2003].

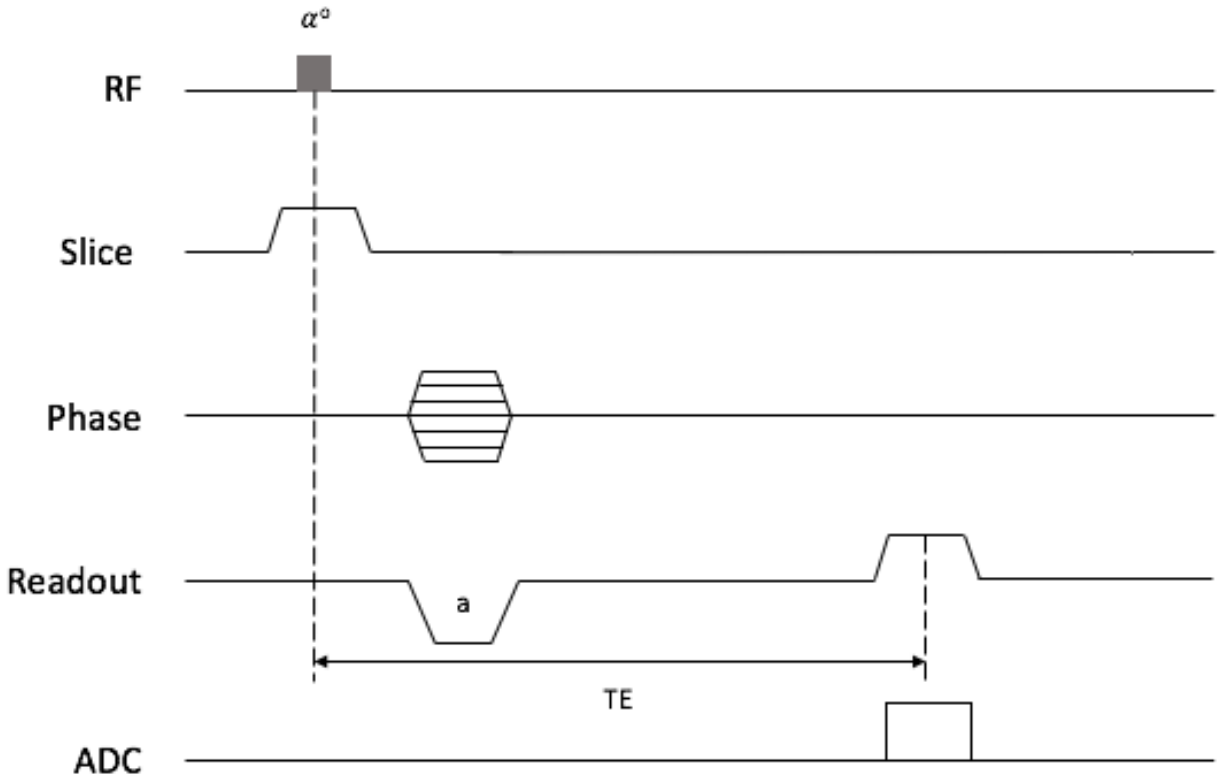

Figure 3 Gradient-echo sequence timing diagram. In the absence of a 180^{o} RF pulse, the orientation of the initial application of the readout dephasing gradient pulse (a) is to the opposite polarity to the readout gradient rephasing pulse applied during signal sampling. Gradient spoiling is demonstrated at the end of the excitation cycle. Figure adapted from Brown and Semelka, 2003.

Another type of commonly used pulse sequence that is also especially relevant for functional MRI is echo planer imaging (EPI). As developed by Sir Peter Mansfield and his colleagues in 1991 [Stehling et al., 1991], EPI creates a set of echo signals caused by the oscillating direction of the readout gradients. Each echo has a different degree of phase encoding so the set of echoes contain a complete range of k-space data. In a single-shot EPI sequence, a whole image is acquired from a single signal sampling in one TR. In multi-shot EPI, all the k-space data are measured with several "shots" in a zig-zag fashion.

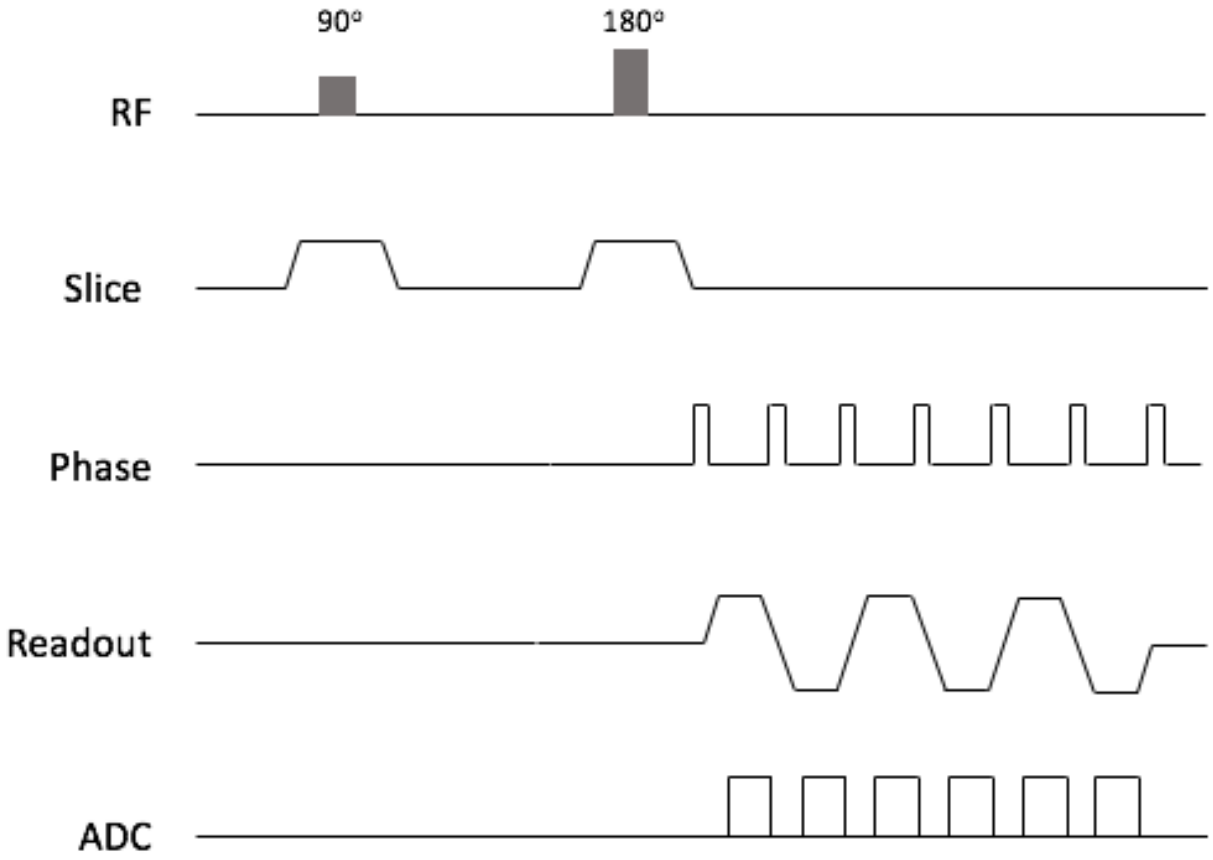

Figure 4 Timing diagrams for a set of echo planar imaging sequences where the continual phase encoding gradient is active during the complete readout period. Each echo's data point has a unique quantity of G_{PE} influence. Figure adapted from Brown and Semelka, 2003.

The development of EPI sequence allows a whole image to be acquired quickly following a single excitation RF pulse and enables the studies of functional MRI (fMRI).

Basic Principles of Blood Oxygenation Level-Dependent fMRI

Functional MRI is well established as a neuroimaging technique for detecting and delineating regions in the brain that change their levels of activity in response to specific experimental conditions [Shi et al., 2017]. The Blood Oxygenation Level-Dependent (BOLD) contrast is the main phenomena measured in fMRI and allows for the imaging of blood flow and oxygenation changes related to the activation of neurons within regions of the brain [Ogawa et al., 1990a; Kwong et al., 1992; Bandettini et al., 1992; Logothetis et al., 2002; Buxton, 2013].

The discovery of BOLD contrast

As reviewed by literature [Logothetis, 2003; Gore, 2003; Faro and Mohamed, 2010; Buxton, 2013], in 1936, the chemist, Linus Pauling, and his student Charles Coryell pursued an in-depth study of the molecular structure of hemoglobin. During their work, they discovered that the magnetic property of the hemoglobin molecule can be changed due to the bound to oxygen. In particular, oxygenated hemoglobin (Hb) has a diamagnetic property while deoxygenated hemoglobin (dHb) has a paramagnetic property [Pauling and Coryell, 1936]. In 1982, Thulborn et al. reported that the T_2 relaxation time of blood is closely related to the amount of bounded oxygen. This laid the physiological foundation for future of fMRI studies [Thulborn et al., 1982]. In 1990, Seiji Ogawa and his colleagues applied a gradient refocused echo (GRE) sequence and observed a decreased signal near the location of apparent blood vessels in the neocortex of rat brain using surface coils at high magnetic fields (7T and 8.4T) with ultra-high spatial resolution ($65 \times 65 \times 700\ \mu m^3$) [Ogawa et al., 1990a]. They further studied the mechanism behind the phenomena and first described BOLD contrast that can reveal blood oxygenation levels because of its sensitivity to the susceptibility effects of deoxygenated blood when measured using a GRE pulse sequence [Ogawa et al., 1990a, b]. This work confirmed that oxygenated hemoglobin carries diamagnetic properties while deoxygenated hemoglobin has paramagnetic properties that distorts the surrounding magnetic field. This magnetic distortion can cause the nuclei to lose magnetization faster during T_2^* decay than would be predicted by molecular mechanisms alone. Therefore, MR pulse sequences that are sensitive to T_2^* decay show more MR signals in oxygen-rich blood and less in oxygen-poor blood and can be used to map active brain regions based on local oxygenated blood flow distribution.

It was from this that Ogawa et al. was able to realize that the blood oxygenation mechanism could be combined with conventional MRI to develop a powerful tool to non-invasively examine brain activity. Subsequent BOLD fMRI studies have also been applied in various types of animals, including rodents, rabbits, cats and monkeys [Turner et al., 1991; Ogawa et al., 1993a; Prielmeier et al., 1993; Logothetis, et al., 1999].

Naturally, researchers have attempted to translate Ogawa's BOLD fMRI work from laboratory animal research to applications in human studies. Unlike early studies which utilized a combination of an echo planar imaging pulse sequence and exogenous paramagnetic contrast agents (e.g., gadolinium) to acquire CBV functional MR images, BOLD imaging is advantageous in that it only relies on intrinsic contrast. Scientists have attempted to take the method a step further, and in 1992, three research groups were able to simultaneously and independently acquire human BOLD fMRI images with no exogenous contrast agent injection [Bandettini et al., 1992; Kwong et al., 1992; Blamire et al., 1992]. As many realized [Logothetis, 2003; Buxton, 2013], this breakthrough technique excited the interest of fMRI applications in humans and laid the foundation of fMRI based clinical applications.

Contributions to T_2^* relaxation

As mentioned earlier in Eq. (3), in any real MRI experiment, the transverse magnetization decays faster than would be predicted by molecular mechanisms alone. The observed rate is $R_2^* = 1/T_2^*$. T_2^* and results primarily from inhomogeneities in the main magnetic field. In addition, there are two effects of intrinsic susceptibility variations within tissues that can reduce T_2^* values. These are called the static dephasing and diffusion effects.

Static dephasing regime

In practice, nuclei in different positions experience their local frequencies in a slightly different magnetic environment, which is the main cause of the static dephasing effect. In addition, these different local frequencies in an inhomogeneous magnetic environment can further cause the spins to move out of phase during the periods before and during data acquisition. These accumulated differences result in reversible spin dephasing and the signal that is digitized from the induced currents of the coil would decrease as well. In Eq. (3), $R_2' = 1/ T_2'$, T_2' represents the

relaxation rate contribution attributable to field inhomogeneities across a voxel. Here, $R_2' \approx (\gamma \Delta B)$, where γ is the gyromagnetic ratio and ΔB represents the field change across the voxel of interest. Static effects may arise from presence of large-scale field inhomogeneities such as large veins.

Water diffusion effects on BOLD contrast

During fMRI experiments, water molecules can diffuse with a diffusion coefficient, *D*, within the intercellular spaces between the paramagnetic deoxygenated red blood cells, plasma, and extravascular space. For these, Kennan et al. pointed out that it is necessary to consider both the static field effects and the diffusion of water molecules when investigating the contributions to transverse decay in BOLD contrast imaging as predicted by the Anderson-Weiss mean field theory [Anderson and Weiss, 1953; Kennan et al., 1994]. Specifically, as described in literature, when diffusion is fast, the rate of transverse decay quadratically varies with the magnetic field and the susceptibility. However, when diffusion is slow, the rate of transverse decay increases quadratically with the magnetic field and linearly with diffusion [Majumdar and Gore, 1987; Kennan et al., 1994].

When the diffusion is relatively slow (e.g., around large vessels) differences in SE and GE can become apparent. The relaxation of a GE sequence is faster than that of a corresponding SE sequence since the SE effectively refocuses the reversible spin dephasing caused by the magnetic inhomogeneity in the transverse plane. Therefore, GE is more sensitive to large vessels while SE is more sensitive to small vessels (capillaries). Further Monte Carlo simulations from Ogawa's group have suggested that the effects from water diffusion is strong for capillaries, but is not important for the determination of deoxyhemoglobin-induced signal dephasing within larger venous blood vessels [Ogawa et al., 1993b].

Extravascular and intravascular BOLD effects

Based on the BOLD contrast model, both extra- and intravascular effects contribute to BOLD signals [Zhong et al., 1998; Ugurbil et al., 2000].

T_2^* relaxation rates in the extravascular space can change around blood vessels. In Ugurbil's paper [Ugurbil et al., 2000], it was described that the extravascular effect around large vessels is linearly dependent on the field strengths while the involvement from smaller vessels

quadratically increases with field strength. Their results suggest that the relative contributions from microvascular BOLD signals increases at high magnetic fields [Ugurbil et al., 2000]. It is known that most underlying neuronal activities occur closer to the capillary sites than large vessels [Lai et al., 1993; Menon et al., 1993]. Therefore in this thesis, a 9.4 T high field strength MRI scanner was used to closely monitor actual neural activity. This was then compared with "gold standard" electrophysiological signals in order to demonstrate the intrinsic limit of BOLD fMRI.

The transverse relaxation rate of blood is dependent on intravascular water diffusion and magnetic field strengths while blood effects are dependent on the T_2 of blood and tissues.

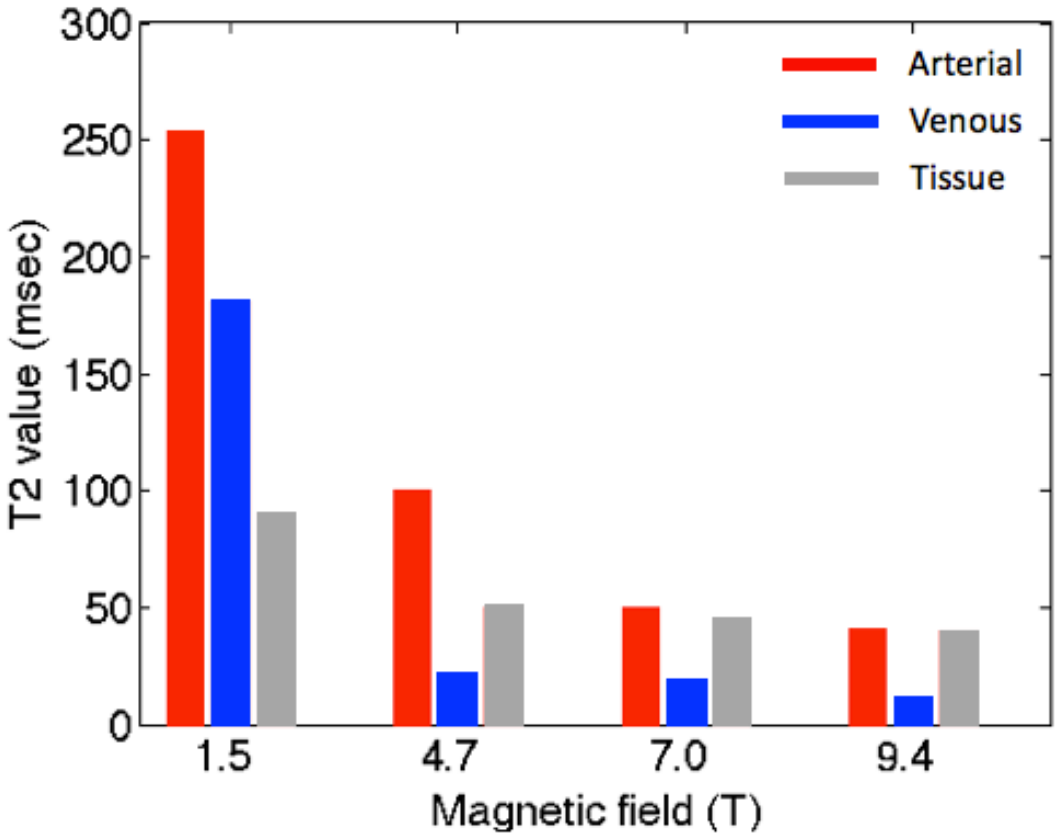

Figure 5 T_2 values of arterial, venous blood and gray matter of the brain in different magnetic field strengths. Data adapted from [Barth and Moser, 1997; Meyer et al., 1995; van Zijl et al., 1998; Ogawa et al., 1993a; Yacoub et al., 2001; Lee et al., 1999].

At a high magnetic field strength, the relative contribution from intravascular effects is substantially diminished due to the very fast T_2 relaxation of venous blood (Figure 5). In particular,

at the 9.4 T magnetic field that is used predominantly in this thesis, the T_2 of venous blood is less than 10 msec. The contribution from the intravascular effects of very high resolution gradient echo images can be suppressed by selecting relatively long TE (e.g., 16 msec).

In summary, neuronal activities are always closely tied to microvascular effects than to larger vessel effects [Kim et al., 1994; Duong et al., 2000]. Therefore, accurate acquisitions of functional maps require diminished contributions of both intravascular signals and the effects of larger vessel dephasing to the overall fMRI signal changes. The key to acquiring BOLD fMRI signals that closely reflect the underlying neuronal activity is to utilize high-resolution studies at high fields with minimized contributions from both intravascular and extravascular effects. At high fields, the relative contributions of both intravascular signals and the effects of larger vessels dephasing to the overall fMRI signal changes are substantially diminished.

Submillimeter resolution fMRI studies at high magnetic fields

BOLD fMRI signals are dependent on the hemoglobin oxygen levels and are caused by changes in the magnetic field that surround red blood cells and vasculature. As mentioned earlier, BOLD contrast is intrinsic as the T_2 and T_2^* relaxation times of the intra- and extra vascular blood are modulated by local gradients which cause intravoxel dephasing. Acquisitions using GE pulse sequences can be used to detect BOLD signals as a GE MRI pulse sequence is sensitive to both T_2 and T_2^* relaxation. At lower magnetic fields commonly used for human applications, such as 1.5 T and 3 T, the T_2^* contrast from venules may be predominant. At higher magnetic fields, such as 7 T and 9.4 T, diffusion dephasing contributes more to the BOLD signal. Through the use of spin echo MRI pulse sequences, BOLD signals can provide higher spatial specificity that is sensitive enough to detect capillaries. However, at lower magnetic fields (e.g., 1.5 T), the BOLD activations in SE sequences are still more dependent upon the signal contribution from large vessels than microvasculature.

BOLD fMRI has been widely used to map large scale networks in human studies. This is not only because most researchers have been interested in clinical applications to understand neurological diseases, but also because the inadequate spatial specificity and low SNR of BOLD have limited the functional mapping of localized brain architecture within small neuronal circuits. In most BOLD fMRI studies, researchers typically use a spatial resolution of $3 \times 3 \times 3$ mm^3 to map the activations of specific tasks. This is inadequate to explore brain functional organization on the

millimeter and submillimeter spatial scale. In addition, the spatial correspondence between the fMRI signal and the actual neuronal activity is built upon the theory that neuronal activity and hemodynamic and metabolic responses are tightly coupled with each other. In order to validate the reproducibility of functional mapping and bolster the confidence in applying functional imaging techniques, many studies have compared functional mapping using different imaging modalities including BOLD fMRI, PET, CBF, CBV, and perfusion MRI, and have reported that the cortical activation locations from different imaging techniques were fairly consistent [van Zijl et al., 1998; Zhu et al., 1998; Kinahan and Noll, 1999].

A number of researchers have used fMRI with higher magnetic fields to improve the spatial specificity and SNR of images. Theoretically, at high fields, the relative contributions of both the intravascular signals and the effects of larger vessels on extravascular dephasing to the overall fMRI signal changes are substantially diminished. Recent studies have successfully implemented fMRI in animal and human laboratory research at very high magnetic fields (e.g. 7 T and 9.4 T) and found that the signal contribution from microvascular effects at high magnetic fields can be detected much more robustly than at low field strengths. Moreover, fMRI at very high fields can achieve higher SNR, which consequently reduces partial volume effects and provides higher spatial specificity. High magnetic field fMRI is promising for mapping brain activation at finer submillimeter scales such as the columnar level. It can be used to potentially detect and investigate the brain functional architecture from large scale networks to small neuronal circuits that are the basic units of information processing. So far, it is one of the most reliable and commonly used neuroimaging approaches to map brain large-scale cognitive systems (several centimeters or even the entire brain) and finer cortical columns (hundreds of micrometers). Submillimeter resolution BOLD at very high magnetic fields also makes it possible to reduce partial volume effects and more closely approach the intrinsic limits of BOLD.

High resolution fMRI studies in nonhuman primates

Rodents are the most commonly used animals in laboratory research as they are affordable and not difficult to handle. However, unlike rodents and other animals, the functional organization of the non-human primate brain shares much greater homology with humans. As electrophysiology is an invasive method that records signals directly from neurons and is considered a more direct indicator of the underlying neuronal activity than BOLD, studies conducted upon monkeys (e.g.,

macaque, squirrel monkeys) using electrophysiology can be used to conveniently bridge the gap between animal research and human fMRI studies. In laboratory animal studies, functional activation maps at a columnar level can be acquired through spiking activity or extracellularly recorded LFP. This is important as cortical columns are believed to be the fundamental building blocks of cerebral cortex functions. FMRI is usually used to investigate the characteristics of the net activity of a large population of neurons at relatively low spatial resolution, based on the blood oxygenation mechanism, which is a secondary response to metabolism driven by the underlying neuronal activity. However, this limitation can potentially be resolved using submillimeter resolution at high magnetic fields to identify individual columns of small neural circuits and achieve the same mapping resolution as electrophysiology. A large amount of work will be required if one wants to translate such studies in human subjects.

After the identification of various large scale networks (e.g., the visual cortex, the motor cortex, the language system, the default mode network, etc.) in the human brain, nearly all previous submillimeter fMRI studies (both human and animal research) have investigated the visual system at both large and finer millimeter scales [Yacoub et al., 2001; Shmuel and Leopold, 2008; Friedman et al., 2011; Wang and Roe, 2012; Chen et al., 2013]. Several studies from different research groups independently have reported the spatial specificity of the BOLD response at different spatial resolution at different magnetic fields in human visual cortex, and their results were reasonably consistent with each other [Engel et al., 1997; Parkes et al., 2005; Yacoub et al., 2001]. However, it is unclear to what degree these findings of the visual cortex can be generalized to other brain networks.

In this thesis, we studied the single digit representation regions in subregions 3b and 1 of S1 cortex of squirrel monkeys at 9.4 T. This alternative and well-organized experimental model allows for the quantitative studies of brain activation and correlation at a columnar level with several advantages. First, single digit representation is an example of classical modular functional structures, which are the basic information processing units of neocortex. A quantitative characterization of the spatial relationships between BOLD and LFP signals at this mesoscopic spatial scale provides insight at a basic information processing level. Secondly, the orderly topographic map of S1 cortex serves as an anchor for our understanding of cortical organization. This orderly map is especially reflected in the hand region which is characterized by a lateral to medial representation of individual digits in three subregions: 3a, 3b and 1. Each area has distinct

stimulus preferences, suggesting their different roles in specific somatosensory functions. This has been well established by studies of neuronal receptive field properties and of the effects of preferred stimuli and histological characterizations [Chen et al., 2011; Wang et al., 2013; Zhang et al., 2007; Shi et al., 2016]. In addition, unlike the visual cortex, stimulus evoked activations in the single digit hand region can reliably be detected and quantified in "single condition" maps. This type of quantification eliminates unnecessary ambiguities in designing orthogonal stimuli that are commonly used to reveal modular structures in the visual system. Thirdly, Wang et al. have previously mapped the functional organization of this region at sub-millimeter scale for touch processing and have demonstrated that single digit fMRI activations can be reliably mapped, that their responses scale with the magnitude of the vibrotactile stimuli, and that digit activations are organized in a somatotopic manner. Finally, the subregions (3a, 3b, and 1) of S1 cortex have been intensively mapped with electrophysiological and histological methods in this species.

Brief summary on the limitations of BOLD fMRI

With the development and improvement of fMRI techniques in the last two decades, fMRI has been widely used to noninvasively study human and nonhuman primate brain functional architecture. BOLD contrast is a complex neurovascular response modulated by several variables and conditions, which not only depends on blood oxygenation but also on cerebral blood flow and volume. Researchers have devoted years to investigating the relationship between hemodynamic changes and their underlying neuronal activity and to quantitatively understanding the different aspects of what BOLD signals truly measure. Unfortunately, the spatial and temporal resolutions of fMRI signals are currently not equivalent to "gold standard" electrophysiology methods. All fMRI studies, especially those with spatial in-plane resolution over a millimeter, suffer from partial volume effects. The BOLD fMRI signal measures at a given voxel reflects the sum of its entire volume, which includes multiple types of cells and tissues each contributing to the total signal. Additionally, the noninvasive advantage of fMRI technique also inevitably limits its precision due to the fact that fMRI measures a surrogate signal considered to be an indirect indicator of actual neuronal activity.

Therefore, in this thesis, we aimed to demonstrate the spatial correspondence between high resolution BOLD fMRI signals at high magnetic field and underlying neural activity in both

stimulation and resting state conditions (including their activation locations and spatial extents) in S1 cortex of nonhuman primate.

Resting State Functional Connectivity

Brain connectivity

Brain connectivity includes anatomical connectivity, functional connectivity, and effective connectivity between distinct brain regions. Anatomical connectivity is structurally based, while functional connectivity (also known as functional correlations) is the temporal relationship between brain networks and can be quantified in terms of Pearson's correlation coefficients. Other measurements include cross-correlations and coherence. Finally, the effective connectivity (also known as causal interactions) refers to the casual relationships of information flow. It is very important to evaluate the brain connectivity as it reveals how populations of neurons process information to achieve various functions.

Neuroscientists have been studying brain connectivity patterns since 1909 [Cajal, 1909; Brodmann, 1909]. In this thesis, the functional connectivity within S1 cortex at the mesoscale provides insight into the connections within and between neuronal columns. We quantitatively compared brain functional connectivity at a columnar level using high resolution BOLD fMRI at high field and electrophysiology signals. This study focuses on a basic information processing level and explores the intrinsic spatial limits of BOLD fMRI.

Resting state BOLD functional connectivity

Low frequency fluctuations in BOLD fMRI signals may occur spontaneously in areas of the cortex in the absence of any specific task [Biswal et al., 1995; Shi et al., 2016]. Functional connectivity is derived from correlations between signal changes from brain regions that share functional properties. Resting state fMRI (rsfMRI) is an extension of functional brain imaging that evaluates regional interactions using spontaneous fluctuations when a subject is not performing a task [Biswal et al., 1995; Cordes et al., 2000]. The resting state approach is an effective method for investigating intrinsic brain circuits and to examine whether or not brain functional connectivity would be altered by psychiatric diseases. A great advantage of resting state studies over stimulus-evoked studies is that it does not require subjects to perform any task, as it is often difficult for patients to follow specific task instructions. For this reason, there has been an increasing interest in studying resting state in recent years. Resting state research has excited a great number of publications and has been investigated with multi-modalities, such as, perfusion

imaging, PET [Raichle et al., 2001], magnetoencephalography (MEG), electroencephalography (EEG), and local field potential (LFP), however, the most common approach is fMRI as it is noninvasive and does not require the use of contrast agents [Lowe et al., 1998; Cordes et al., 2000]. Figure 6 shows the number of publications per 5-year period related to a PubMed search of "resting state brain connectivity".

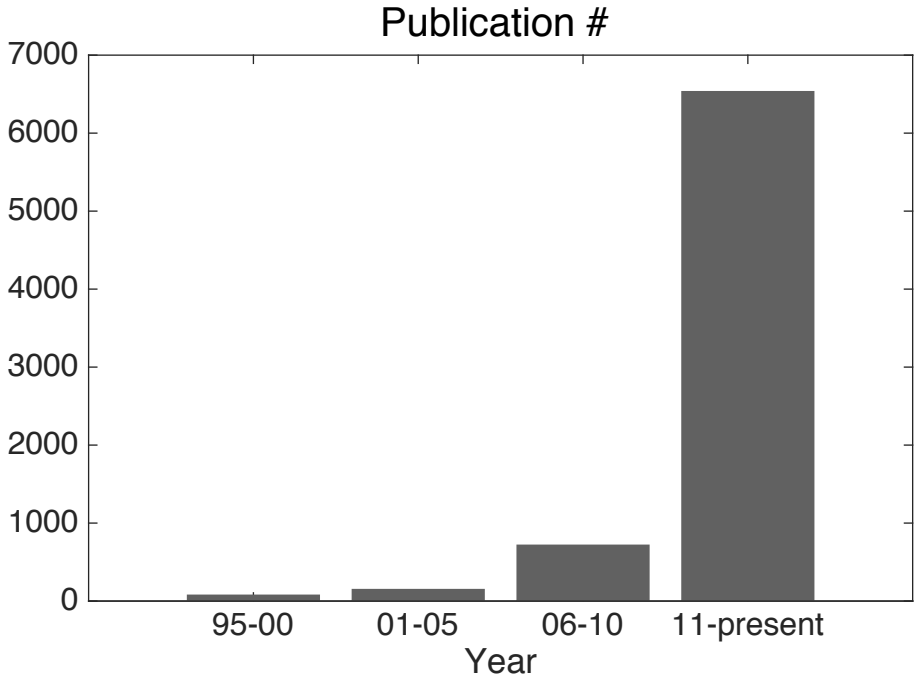

Figure 6 The increase in the number of publications per 5-year period related to a PubMed search of "resting state connectivity".

Resting state fMRI has received much attention since 1995. Biswal et al. first reported the fMRI functional correlations between the left and right motor cortices when the brain was in a resting state [Biswal et al., 1995; Shi et al., 2016]. They applied a seed-based analysis to investigate resting state functional connectivity, and as described in their paper, specific region of interest (ROI) seeds were selected in the left somatosensory cortex according to block design stimulus-evoked fMRI in a separate scanning run during which the same subjects were instructed to perform bilateral finger tapping. They computed the Pearson's correlation coefficients between the BOLD time series of the identified ROI seed and those of the other voxels in the brain and found high correlations between the left somatosensory cortex and homologous areas in the right

somatosensory cortex. This high correlation showed the existence of synchronized spontaneous signal fluctuations in the contralateral hemisphere, and opened the door for exploring intrinsic functional organization of the brain. Subsequent studies have identified several consistent resting-state networks, including motor, auditory, visual, attention, and default mode [Lowe et al., 1998; Beckmann et al., 2005; Damoiseaux et al., 2006; Yeo et al., 2011; Shi et al., 2016].

The bandwidths of resting state fMRI signals

Fluctuations in resting state BOLD fMRI signals have been found to be correlated across distributed brain regions, predominantly in the low-frequency range between 0.01 and 0.1 Hz [Biswal et al., 1995; Lowe et al., 2000; Cordes et al., 2001]. In general, it is widely accepted that in human studies, resting state BOLD fMRI fluctuations are filtered in this specific low frequency range from 0.01 to 0.1Hz partly to avoid the noise caused by normal physiological functions present in BOLD fMRI signals [Murphy et al., 2013]. These include, for example, the respiration signal between 0.2 and 0.3 Hz and the cardiac signals around or beyond 1 Hz [Brooks et al., 2013]. Despite that the heart rate of animals (< 300 beats per minute) is always much higher than humans, a similar low frequency band is also applied to animal fMRI research [Kannurpatti et al., 2008; Hutchison et al., 2010; Gohel et al., 2015]. In addition, numerous studies in the past have reported that in resting state BOLD signals, functional connectivity between brain regions that are less than 0.1 Hz contributed significantly more than those between 0.1 and 1 Hz. This supports the rational for applying the lowpass filter in the BOLD preprocessing steps [Cordes et al., 2001; Gohel et al., 2015].

It is essential to remove artifacts in resting state fMRI preprocessing procedures [Jo et al., 2013; Power et al., 2014; Griffanti et al., 2015]. Common steps include temporal bandpass filtering of the resting state BOLD fMRI signals between 0.01 and 0.1 Hz as described above. In addition, RETROICOR has been widely used to remove the physiological noises [Glover et al., 2000] and is also used as a preprocessing step in this thesis. In this method, low order Fourier series whose frequencies and phases are derived from measurements made in explicitly recorded cardiac and respiratory signals are retrospectively corrected in resting state BOLD images [Birn et al., 2006; Murphy et al., 2013]. However, despite how effective this approach is to eliminate the effects of physiological noises, it can be inconvenient in certain studies as it requires the simultaneous recording of cardiac respiratory signals [Glover et al., 2000; Yan et al., 2009].

The dynamics of functional connectivity

Most fMRI studies in the past have assumed that the correlations between brain regions in resting-state experiments are constant throughout the time series of the entire scan [Greicius et al., 2003; Fox et al., 2005; Fransson, 2005; Power et al., 2011]. This assumption simplifies not only the analysis methods but also the interpretation of connectivity results. However, it is natural to speculate that the brain functional organization is dynamic since different networks work together in a non-linear and non-stationary manner to achieve all sorts of functions [Hansen et al., 2015]. As the statistical approaches and computational modeling become more accurate and creative, analysis methods built upon the dynamic feature of functional connectivity have excited more researchers' interest and produced literature expanding our view and knowledge of dynamic connectivity.

More recently, there has been an increasing interest in the detection and characterization of possible dynamic changes in functional connectivity [Chang and Glover, 2010; Allen et al., 2014; Hutchison et al., 2013a, b; Shi et al., 2016]. Apparent temporal dynamic changes in functional connectivity may provide better insight and understanding of the fundamental features of brain systems [Chang et al., 2013; Hutchison et al., 2013]. However, there is hardly any straightforward explanation and interpretation for the dynamics of functional connectivity [Bastos et al., 2016]. Variations in the degree of coupling between different networks would seem to be a plausible feature of neural systems, and the nature of temporal changes in such couplings could be an important aspect of brain function. However, the unambiguous detection and quantification of dynamic changes in correlations are not trivial and are similar to the well-known difficulties in classifying data as statistically stationary or non-stationary. It is critical to know whether or not the observed dynamic changes in correlations between distinct brain regions over time show significantly greater variability than would be expected if the underlying correlation coefficient between the two signals were stationary [Shi et al., 2016].

Current techniques for assessing functional connectivity network

In addition to the seed based approach described above, a variety of analytical methods have been used to derive functional connectivity to reveal functionally related brain regions [Beckmann et al., 2005; Yeo et al., 2011]. Even though dynamic functional connectivity is

currently widely accepted, stationary techniques for assessing resting state functional connectivity network are still of great value. For example, seed-based ROI analysis, in which the time course of a seed ROI is used as a regressor to identify regions of similar temporal behavior elsewhere in the brain, can be used to quantify the relationship between two ROIs as a single correlation coefficient calculated from the entire scan duration. However, this single value approach cannot detect possible temporal variations over time [Shi et al., 2016].

Independent component analysis

Several data-driven methods have been developed to quantify functional connectivity. These include independent component analysis (ICA) and principle components analysis (PCA) [Li et al., 2009; Hawellek et al., 2011]. ICA is a model-free mathematical technique that optimizes the statistical independence between its components [Herault and Jutten, 1986; McKeown et al., 1998]. This method decomposes the fMRI time courses into a prescribed number of components with maximal spatial independence [Calhoun et al., 2009]. While this strategy avoids the inconvenience and possible inaccuracy from selecting specific seed regions, it does not account for the possible changes in inter-regional interactions over time. In addition, the interpretation of different components, especially the selection of component criterion in such analyses, is often difficult. Moreover, there is hardly any straightforward criterion to separate higher order components from non-neuronal physiological noise. However, even though the computational processes of the seed-based analysis and ICA are different, several research groups showed that there is no significant difference in the results that are analyzed from both methods [Joel et al., 2011].

Graph theory

Another common approach for analyzing the functional connectivity is a graph theory method, which was recently proposed and can serve as an alternative to a seed-based analysis and ICA approach [Bullmore and Sporns, 2009; Wang et al., 2010]. In this method, resting state networks are treated as a group of nodes that are connected by edges [Hagmann et al., 2008]. ROIs are considered as nodes and correlations between different ROIs serve as edges. Here, the researchers are interested in computing the average path length and a quantitative measure of how

well different ROIs are connected to each other [Lang et al., 2012]. The latter is quantified by the average length of the shortest pathway between all pairs of nodes. The clustering coefficient is another important quantification in this method [van den Heuvel et al., 2008; Fallani et al., 2014]. Similar to the average path length, the clustering coefficient is a quantitative measure of how well a ROI is connected with its neighboring nodes, which can then be used to generate several smaller subgraphs. Literature suggests that the brain might potentially present a small world topology when analyzed using the graph theory as described above [Sporns et al., 2007]. Small world subgraphs with high clustering coefficients usually indicate tighter relationships within local connections [Leskovec et al., 2008]. In general, these short average path lengths also imply a short distance between any two nodes [Fronczak et al., 2004].

Clustering

Another popular method for analyzing rsfMRI data is clustering, which categorizes different ROIs into groups. One commonly used algorithm is hierarchical clustering, which seeks to build a hierarchy of all members using variables such as distance, Pearson correlation coefficients, and etc [Cordes, et al., 2002]. Another clustering method is based on the k-means clustering algorithms [Golland et al., 2008] in which all voxels are characterized to one of many clusters according to their measured distances from the cluster centers. This algorithm can iteratively update itself and will present a final set of clusters when convergence is reached. Self-organized mapping is another variation of clustering techniques in which anatomical maps and correlation values in functional connectivity can be used as clustering criterion [Mishra et al., 2014]. However in this approach, a pre-defined number of clusters is needed and can lead to biased results.

Electrophysiology

Local field potentials

Electrophysiology is an invasive (and sometimes noninvasive as in the case of EEG) technology for the purpose of directly studying the electrical properties of cells and tissues. Electrophysiological studies date back to 1875, when Caton first reported electrical signals from the brain surfaces of living rabbits [Caton, 1875]. Electrophysiology typically measures electrical voltage changes or electrical current flows from single ion (e.g., sodium, potassium, etc.) channel proteins on the membrane to whole tissues (e.g., heart, brain, etc.). Electrophysiology recordings include intracellular and extracellular recordings. Intracellular recording usually refers to the electrical voltage and current signals when the cell is under non-equilibrium conditions and current is flowing through the cell (Figure 7). On the other hand, the extracellular field is comprised of excitable membrane and transmembrane currents and thus represents a cumulative superposition of the total ionic potentials at that particular brain location [Buzsaki et al., 2012]. Extracellular recordings can be acquired with amplification using an electrode that is inserted into a brain region of a living animal. The tip of an electrode can detect the electrical voltage generated by the neurons in a small area close to the tip (the diameter of a few hundred micrometers).

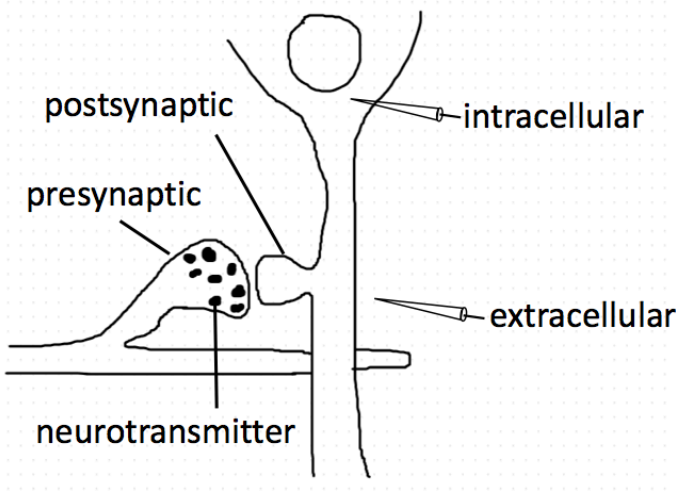

Figure 7 A schematic diagram showing a field potential recording from monkey somatosensory cortex, including presynaptic terminal and postsynaptic neuron. An intracellular electrode is inserted inside the cell body, to record the voltage and current changes across the membrane of the cell, an extracellular electrode was placed outside the cell body, to record local field potential signals.

Local field potentials are electrophysiological voltages generated by the summed electric currents flowing from populations of neurons within small volumes of nervous tissue around the recording electrode tips [Legatt et al, 1980]. These voltages generated by the action potentials across the cell membrane can be recorded by an inserted microelectrode and often consists of a population of neurons within a radius of a few hundred micrometers of the microelectrode tip [Linden et al., 2011]. Because neurons form interdependencies with one another through chemical and electrical synapses (Figure 7), LFPs are also a measurement of the low frequency activity (< 300 Hz) across the neuron population, including a combination of pre- and post-synaptic activities. The LFP signals are thought to represent the synchronized input of neuronal signals to a particular brain region [Buzsaki et al., 2012]. During signal pre-processing for LFP signal analysis, a band pass filter is used to pass only low-frequency fluctuations below 300 Hz related to peri-synaptic activity. Anything higher than 300 Hz is not relevant as these fluctuations in the LFP differences are mostly the result of current spikes within action potentials [Berens et al., 2010]. In general, LFPs represent the slow neuronal fluctuation waveforms and reflect the input of neuronal signals into a particular cerebral cortical region [Buzsaki et al., 2012; Herreras et al., 2016].

Mechanism of neural oscillations

Neuroscientists have always been very interested in subdivided neuronal signal bands, as the characteristics of the electrophysiological signal waveform are dependent on the involvement of many sources and properties of the brain. Broad band electrophysiological signals most likely reflect contributions of several different neural processing pathways and are typically decomposed and analyzed in the frequency domain [Magri et al., 2012; Einevoll et al., 2013].

Historically, the neuronal fluctuations are classified within a set of specific frequency ranges first introduced in the electroencephalography (EEG) literature [Bullock et al., 1997; Volgushev et al., 2006; Harmony, 2013]. Previous studies have acquired EEG signals when the subject is in different brain states and have subdivided rhythmic EEG into seven frequency bands: delta (1-4 Hz), theta (5-8 Hz), alpha (9-14 Hz), beta (15-30 Hz), gamma low (31-50 Hz), gamma high (51-100 Hz), and gamma very high (101-150 Hz) [Leopold et al., 2003; Tort et al., 2010; Ray and Maunsell, 2011; Belluscio et al., 2012; Wilson et al., 2016]. Delta waves are always detected during unconsciousness and dreamless deep sleep [Sanders et al., 2012]. Theta waves usually

appear in a dream sleep "rapid eye movement sleep" condition or meditation. Alpha waves can be observed when an experimental subject is daydreaming or in an eyes-closed relaxed state, and beta waves are indicators of analytical thinking and often appears when a subject eyes are open [Bazanova, 2012]. In summary, the oscillatory activities in these subdivided electrophysiological bands are associated with a balance of thalamo-cortical and cortico-cortical loops [Buzsaki et al., 2012].

Delta oscillations

Studies on a range of LFP frequency bands can be dated back to 1937 when Berger first discovered delta waves in rat brains [Berger, 1937]. Since then, LFP delta oscillations have been studied extensively and are believed to be related the unconscious brain state such as during deep sleep or deep sedation [Krishnan et al., 2016]. It is widely accepted that delta oscillations mostly originate from thalamocortical cells due to the spherical symmetry of the neurons [Lorente de No, 1947; Timofeev et al., 2012; Neske et al., 2016]. From a cellular point of view, the firing of cortical and thalamic cells is usually associated with slow neuronal oscillations. Steriade et al. first reported this finding when subjects under anesthesia were observed to drift into a natural sleep brain state [Steriade et al., 1993]. However, some recent studies suggested that delta waves may also occur during decision making, and most likely reflect the relationship between parietal and frontal neural circuits [Nacher et al., 2013].

Theta oscillations

Theta-band oscillations have been observed in the prefrontal cortex and are believed to be contributors to the information selection process [Sirota et al., 2008]. Most studies have reported that theta oscillations are closely associated with active behaviors, for example, researchers reported that theta waves are present during working memory studies in monkeys and humans [Chapman and Lacaille, 1999; Preston and Eichenbaum, 2013; Jutras et al., 2013].

Alpha and beta oscillations

In human electrophysiology, researches have noticed that the shapes of alpha and beta waves can be well approximated as non-sinusoidal patterns in the brain cortical motor region

[Kuhlman, 1978; Salmelin and Hari, 1994; Cole and Voytek, 2017]. Because of the arch-like waveforms that often fluctuate around 10 Hz, these waves were also named after the Greek character, μ [Kuhlman, 1978]. Neuroscientists have observed the arch-like alpha waves in monkey and rodent somatosensory cortex and have proposed similarities to the alpha oscillations in human EEG studies. Separately, beta rhythms have also recorded from the cerebral motor cortex and exhibit some non-sinusoidal features similar to alpha oscillations [Sherman et al., 2016]. As different neuronal oscillations are always associated with distinct brain states, alpha rhythms have often been acquired in perception and behavior while beta rhythms most likely dominate the waking consciousness state [Buzsaki and Draguhn, 2004].

Gamma oscillations

Gamma rhythms are one of the most widely measured waves in distributed brain regions during both awake and sleep conditions and have been comprehensively studied using various techniques [Bragin et al., 1995; Sirota et al., 2008; Ray and Maunsell, 2012].

Gamma waves commonly emerge within a fine neural circuit and there is little evidence showing that gamma oscillations interact in distant brain regions [Buzsaki and Wang, 2012]. However, many studies have applied the cross-frequency phase-phase coupling (CF_{PP}) technique and reported that gamma oscillations usually interact with other lower bands within or across structures [Buzsaki et al., 1983; Lakatos et al., 2005; Colgin et al., 2009; Palva et al., 2005; Wang et al., 2012]. Cross-frequency coupling analysis has revealed subdivided gamma bands [Tort et al., 2008; Canolty et al., 2010]. In the hippocampal region, wavelet analysis has been applied to distinguish three gamma sub-bands including gamma low (30-50 Hz), gamma high (50-100 Hz), and gamma very high (100-150 Hz) [Tort et al., 2010; Belluscio et al., 2012]. The origins of these three sub-bands are well supported by the distinct spatial spreads in various depths of the hippocampal pyramidal layer [Belluscio et al., 2012].

To date, there have been consistent reports of close temporal relationships between BOLD signals and electrophysiological activity in gamma oscillations during stimulation in distributed brain regions [Logothetis et al., 2002; Nir et al., 2007]. However, there is no consensus about what LFP frequencies correspond to resting state fMRI signals. While some studies have reported that lower frequency fluctuations in LFP signals may correspond most to variations in resting state BOLD signals [Lu et al., 2007; Wang et al., 2012; Wilson et al., 2016], others have suggested that

the slow oscillations in the LFP gamma band power may contribute most to the resting state BOLD signal variations [Leopold et al., 2003; Nir et al., 2008]. Moreover, dynamic changes of fMRI functional connectivity may represent different levels of neural modulation [Magri et al., 2012], but few studies have directly compared the temporal variations of functional connectivity observed in spontaneous fMRI with corresponding LFP signals [Pan et al, 2011; Thompson et al., 2015]. Therefore in this thesis, we investigate the spatial and temporal relationships between resting state BOLD fMRI signals and spontaneous frequency-specific LFPs within primary somatosensory areas 3b and 1, and from there, evaluate the frequency ranges of LFP coherences that most parallel the dynamic features of resting state BOLD functional connectivity at a submillimeter cortical meso-scale.

Goal

The overall goal of this dissertation is to evaluate whether inter-regional correlations in resting state fluctuations of functional magnetic resonance imaging (fMRI) signals from the brain reliably measure functional connectivity between regions, and to investigate the dynamic nature of functional connectivity in both fMRI and frequency-specific electrophysiological signals.

First, to demonstrate the spatial distributions of BOLD and LFP signals in both information processing and their correlation profiles in a resting state, this thesis directly compares the spatial extents and locations of activations and the local correlation profiles between LFPs and submillimeter resolution BOLD at 9.4T within S1 cortex in individual monkeys.

Second, to identify possible temporal dynamic changes in functional connectivity, a filtered stationary model that generates statistically stationary time series from random data with a single prescribed correlation coefficient, is developed to simulate real fMRI functional correlations. In addition, a dynamic model is developed, which is better able to replicate changes in real fMRI connectivity estimated from monkey brain studies than the stationary model.

Finally, to evaluate the differences in dynamic patterns between fMRI and frequency-specific LFP functional connectivity, the time-varying probability distributions between both modalities were quantitatively compared, using a sliding window correlation technique and a Markov chain model-based approach.

Specific Aims

Specific aim 1: Demonstrate the spatial correspondence between BOLD fMRI and underlying neural activity in stimulations. Stimulus-evoked BOLD fMRI data at 9.4T using vibrotactile stimuli to identify areas 3b and 1 in SI cortex of nonhuman primate brains, will be compared to invasive electrophysiological measurements in the same animals. From there, the degree of spatial overlap between electrophysiologically defined neuronal response maps and stimulus-evoked BOLD response maps may be determined by directly comparing the activation foci and their corresponding spatial profiles.

Specific aim 2: Spatially investigate the measurements of functional connectivity from resting state BOLD fMRI signals by direct comparisons with quantitative electrophysiology. Using the same monkey SI cortex model in aim 1, resting state BOLD fMRI data and electrophysiological signals will be acquired from the same animals separately. These may be used to (a) measure the local intrinsic point spread functions of resting-state BOLD correlations; (b) determine the degree of correspondence between electrophysiological inter-electrode connectivity maps and resting state BOLD inter-voxel correlation maps; (c) directly compare the spatial extents of stimulated activations and the local profiles of intervoxel resting-state correlations for both BOLD and electrophysiological signals.

Specific aim 3: Investigate the variations of functional connectivity from resting state BOLD fMRI and frequency-specific electrophysiological signals using stationary, nonstationary models and Markov model-based approach. Correlations in fMRI data will be shown to be non-stationary, and differences in the resting-state connectivity from fMRI and frequency-specific electrophysiological signals will be quantified. We then will (a) simulate the behavior of the temporal correlations between different SI subregions using stationary and non-stationary models; (b) quantitatively compare simulated results to the behaviors of real functional connectivity in monkey brains using a sliding window technique and a variant of the Kolmogorov-Smirnov (K-S) statistic; (c) using a Markov model-based approach, determine which frequency range of spontaneous electrical recordings from identified regions show dynamic patterns of correlation similar to resting state BOLD fMRI.

References

Allen, E.A., Damaraju, E., Plis, S.M., Erhardt, E.B., Eichele, T. and Calhoun, V.D. (2014) Tracking whole-brain connectivity dynamics in the resting state. *Cereb Cortex,* **24**, 663–676.

Altman, P.L. and Dittmer, D.S. (1964) Biology data book. Fed. *Amer. Soc. exp. Biol., Washington DC*.

Anderson, P.W. and Weiss, P.R. (1953) Exchange narrowing in paramagnetic resonance. *Rev. Mod. Phys.,* **25**, 269-276.

Bandettini, P. A., Wong, E. C, Hinks, R. S., Tikofsky, R. S., and Hyde, J. S. (1992). Time course EPI of human brain function during task activation. *Magn. Reson. Med.,* **25**, 390-397.

Barth, M. and Moser, E. (1997) Proton NMR relaxation times of human blood samples at 1.5 T and implications for functional MRI. *Cell. Mol. Biol.,* **43**(5), 783-91.

Bastos, A.M. and Schoffelen, J.M. (2016) A tutorial review of functional connectivity analysis methods and their interpretational pitfalls. *Frontiers in systems neuroscience*, **9**, 175.

Bazanova, O. (2012) Comments for current interpretation EEG alpha activity: A review and analysis. *Journal of Behavioral and Brain Science,* **2**, 239.

Beckmann, C.F., DeLuca, M., Devlin, J.T. and Smith, S.M. (2005) Investigations into resting-state connectivity using independent component analysis. *Philos Trans R Soc Lond B Biol Sci.,* **360**, 1001-1013.

Belluscio, M.A., Mizuseki, K., Schmidt, R., Kempter, R. and Buzsaki, G. (2012) Cross-frequency phase-phase coupling between theta and gamma oscillations in the hippocampus. *J. Neurosci.,* **32**, 423–35.

Berens, P., Logothetis, N.K. and Tolias, A.S. (2010) Local field potentials, BOLD and spiking activity–relationships and physiological mechanisms. *Nat. Prec*.

Berger, H. (1937) About the human's electroencephalogram. *European Archives of Psychiatry and Clinical Neuroscience,* **106**, 165-187.

Bernstein, M.A., King, K.F. and Zhou, X.J. (2004) Handbook of MRI pulse sequences. *Elsevier*, 1st edition.

Birn, R.M., Diamond, J.B., Smith, M.A. and Bandettini, P.A. (2006) Separating respiratory-variation-related fluctuations from neuronal-activity-related fluctuations in fMRI. *Neuroimage*, **31**, 1536–1548.

Biswal, B., Yetkin, F.Z., Haughton, V.M. and Hyde, J.S. (1995) Functional connectivity in the motor cortex of resting human brain using echo-planar MRI. *Magn Reson Med.,* **34**, 537–541.

Blamire, A.M., Ogawa, S., Ugurbil, K., Rothman, D., McCarthy, G., Ellermann, J.M., Hyder, F., Rattner, Z. and Shulman, R.G. (1992) Dynamic mapping of the human visual cortex by high-speed magnetic resonance imaging. *Proc. Natl. Acad. Sci. USA,* **89**, 11069-11073.

Bloch, F., Hansen, W. W., and Packard, M. (1946) Nuclear induction. *Phys. Rev*., **69**, 127.

Bragin, A., Jando, G., Nadasdy, Z., Hetke, J., Wise, K. and Buzsaki, G. (1995) Gamma (40-100 Hz) oscillation in the hippocampus of the behaving rat. *J. Neurosci.,* **15**, 47–60.

Brodmann, K. (1909) Vergleichende Lokalisationslehre der Grosshirnrinde in ihren Prinzipien dargestellt auf Grund des Zellenbaues. J.A. Barth, Leipzig.

Brooks, J.C., Faull, O.K., Pattinson, K.T., and Jenkinson, M. (2013) Physiological noise in brainstem FMRI. *Frontiers in human neuroscience*, **13**, 7.

Brown, M.A. and Semelka, R.C. (2003) MRI: Basic Principles and Applications. *John Wiley & Sons,* 3rd edition.

Bullmore, E. and Sporns, O. (2009) Complex brain networks: graph theoretical analysis of structural and functional systems. *Nat Rev Neurosci*., **10**, 186–98.

Bullock, T.H., Achimowicz, J.Z., Duckrow, R.B., Spencer, S.S. and Iragui-Madoz, V.J. (1997) Bicoherence of intracranial EEG in sleep, wakefulness and seizures. *Electroencephalography and clinical Neurophysiology*, **103**, 661-678.

Bushberg, J. T. and Boone, J. M. (2011) The essential physics of medical imaging. *Lippincott Williams & Wilkins,* 3rd edition.

Buxton, R. B. (2013) The physics of functional magnetic resonance imaging (fMRI). *Reports on Progress in Physics*, **76**, 096601.

Buzsáki, G. and Wang, X.J. (2012) Mechanisms of gamma oscillations. *Annual review of neuroscience*, **35**, 203-225.

Buzsáki, G., Anastassiou, C.A. and Koch, C. (2012) The origin of extracellular fields and currents—EEG, ECoG, LFP and spikes. *Nature reviews neuroscience*, **13**, 407-420.

Buzsaki, G., Draguhn, A. (2004) Neuronal Oscillations in Cortical Networks. *Science,* **304**, 1926-1929.

Buzsaki, G., Leung, L.W. and Vanderwolf, C.H. (1983) Cellular bases of hippocampal EEG in the behaving rat. *Brain Res.,* **287**, 139–71.

Cajal, SR. (1909) Histologie du systéme nerveux de l'homme et des vertebras. Maloine, Paris. English translation by N. and L. Swanson, *Oxford University Press*, 1995.

Calhoun, V.D., Liu, J. and Adali, T. (2009) A review of group ICA for fMRI data and ICA for joint inference of imaging, genetic, and ERP data. *Neuroimage*, **45**, 163-S172.

Canolty, R.T. and Knight, R.T. (2010) The functional role of cross-frequency coupling. *Trends Cogn. Sci.,* **14**, 506-15.

Caton, R. (1875) The electrical currents of the brain. *British Medical Journal,* **2**, 278.

Chang, C and Glover, G.H. (2010) Time-frequency dynamics of resting- state brain connectivity measured with fMRI. *Neuroimage,* **50**, 81–98.

Chapman, C.A. and Lacaille, J.C. (1999) Cholinergic induction of theta frequency oscillations in hippocampal inhibitory interneurons and pacing of pyramidal cell firing. *J Neurosci.,* **19**, 8637–8645.

Chavhan, G.B., Babyn, P.S., Thomas, B., Shroff, M.M. and Haacke, E.M. (2009) Principles, techniques, and applications of T_2^*-based MR imaging and its special applications. *Radiographics*, **29**, 1433-1449.

Chen, G., Wang F., Gore J. C. and Roe A. W (2013) Layer-specific BOLD activation in awake monkey V1 revealed by ultra-high spatial resolution functional magnetic resonance imaging. *Neuroimage,* **64**, 147-55.

Cole, S.R. and Voytek, B. (2017) Brain oscillations and the importance of waveform shape. *Trends in cognitive sciences*., **21**, 137-49.

Colgin, L.L., Denninger, T., Fyhn, M., Hafting, T. and Bonnevie, T. (2009) Frequency of gamma oscillations routes flow of information in the hippocampus. *Nature,* **462**, 353–57.

Cordes, D., Haughton, V., Carew, J.D., Arfanakis, K. and Maravilla, K. (2002) Hierarchical clustering to measure connectivity in fMRI resting-state data. *Magn Reson Imaging*, **20**, 305–17.

Cordes, D., Haughton, V.M., Arfanakis, K., Carew, J.D., Turski, P.A., Moritz, C.H., Quigley, M.A. and Meyerand, M.E. (2001) Frequencies contributing to functional connectivity in the cerebral cortex in "resting-state" data. *American Journal of Neuroradiology*, **22**, 1326-1333.

Cordes, D., Haughton, V.M., Arfanakis, K., Wendt, G.J., Turski, P.A., Moritz, C.H., Quigley, M.A. and Meyerand, M.E. (2000) Mapping functionally related regions of brain with functional connectivity MR imaging. *AJNR Am J Neuroradiol.,* **21**, 1636–1644.

Dirac, P. (1958) The Principles of Quantum Mechanics. *Oxford: Clarendon Press,* 4th edition.

Duong, T.Q., Silva, A.C., Lee, S.P. and Kim, S.G. (2000) Functional MRI of Calcium-Dependent Synaptic Activity: Cross Correlation with CBF and BOLD measurements. *Magn Reson Med.,* **43**, 383-392.

Einevoll, G.T., Kayser, C., Logothetis, N.K. and Panzeri, S. (2013) Modelling and analysis of local field potentials for studying the function of cortical circuits. *Nature Reviews Neuroscience*, **14**, 770-785.

Elster, A.D. (1993) Gradient-echo MR imaging: techniques and acronyms. *Radiology*, **186**, 1-8.

Engel, S.A., Glover, G.H. and Wandell, B.A. (1997) Retinotopic organization in human visual cortex and the spatial precision of functional MRI. *Cerebral Cortex,* **7**, 181–192.

Fallani, F.D.V., Richiardi, J., Chavez, M. and Achard, S. (2014) Graph analysis of functional brain networks: practical issues in translational neuroscience. *Phil. Trans. R. Soc. B.*, **369**, 20130521.

Faro, S. H., Mohamed, F. B., Law, M. and Ulmer, J. T. (2011) Functional neuroradiology: principles and clinical applications. *Springer Science & Business Media*.

Fox, M.D., Snyder, A.Z., Vincent, J.L., Corbetta, M., Van Essen, D.C. and Raichle, M.E. (2005) The human brain is intrinsically organized into dynamic, anticorrelated functional networks. *Proc Natl Acad Sci USA,* **102**, 9673–9678.

Fransson, P. (2005) Spontaneous low-frequency BOLD signal fluctuations: An fMRI investigation of the resting-state default mode of brain function hypothesis. *Hum Brain Mapp.,* **26**, 15–29.

Friedman, R.M., Chen, L.M. and Roe, A.W. (2008) Responses of areas 3b and 1 in anesthetized squirrel monkeys to single- and dual-site stimulation of the digits. *J Neurophysiol.,* **100**, 3185–3196.

Friedman, R.M., Dillenburger, B.C., Wang, F., Avison, M.J., Gore, J.C., Roe, A.W. and Chen, L.M (2011) Methods for fine scale functional imaging of tactile motion in human and nonhuman primates. *Open Neuroimag J.,* **5**, 160-71.

Fronczak, A., Fronczak, P. and Hołyst, J.A. (2004) Average path length in random networks. *Physical Review E.,* **70**, 056110.

Glover, G.H., Li, T.Q., Ress, D. (2000) Image-based method for retrospective correction of physiological motion effects in fMRI: RETROICOR. *Magn Reson Med.,* **44**, 162–167.

Gohel, S.R. and Biswal, B.B. (2015) Functional integration between brain regions at rest occurs in multiple-frequency bands. *Brain connectivity*, **5**, 23-34.

Golland, Y., Golland, P., Bentin, S. and Malach, R. (2008) Data-driven clustering reveals a fundamental subdivision of the human cortex into two global systems. *Neuropsychology,* **46**, 540–53.

Gore, J. C. (2003) Principles and practice of functional MRI of the human brain. *Journal of Clinical Investigation*, **112**, 4.

Greicius, M.D., Krasnow, B., Reiss, A.L. and Menon, V. (2003) Functional connectivity in the resting brain: A network analysis of the default mode hypothesis. *Proc Natl Acad Sci USA,* **100**, 253–258.

Griffanti, L., Dipasquale, O., Laganà, M.M., Nemni, R., Clerici, M., Smith, S.M., Baselli, G. and Baglio, F. (2015) Effective artifact removal in resting state fMRI data improves detection of DMN functional connectivity alteration in Alzheimer's disease. *Frontiers in human neuroscience*, **9**.

Haacke EM, Brown RW, Thompson MR and Venkatesan R. (1999) Magnetic Resonance Imaging, Physical Principles and Sequence Design. *Wiley-Liss,* 2nd edition.

Haacke EM, Tkach JA and Parrish TB. (1989) Reduction of T_2^* dephasing in gradient field-echo imaging. *Radiology,* **170**, 457–462.

Hagmann, P., Cammoun, L., Gigandet, X., Meuli, R., Honey, C.J., Wedeen, V.J. and Sporns, O. (2008) Mapping the structural core of human cerebral cortex. *PLoS biology*, **6**, 159.

Hansen, E.C., Battaglia, D., Spiegler, A., Deco, G. and Jirsa, V.K. (2015) Functional connectivity dynamics: modeling the switching behavior of the resting state. *Neuroimage*, **105**, 525-535.

Harmony, T. (2013) The functional significance of delta oscillations in cognitive processing. *Frontiers in integrative neuroscience*, **7**.

Hawellek, D.J., Hipp, J.F., Lewis, C.M., Corbetta, M. and Engel, A.K. (2011) Increased functional connectivity indicates the severity of cognitive impairment in multiple sclerosis. *Proc Natl Acad Sci USA,* **108**, 19066-19071.

Herault, J. and Jutten, C. (1986) Space or time adaptive signal processing by neural network models. *AIP conference proceedings,* **151**, 206-211.

Herreras, O. (2016) Local Field Potentials: Myths and Misunderstandings. *Frontiers in neural circuits*, **10**.

Huettel, S.A., Song, A.W. and McCarthy, G. (2004) Functional magnetic resonance imaging (Vol. 1). *Sunderland: Sinauer Associates*.

Hutchison, R.M., Mirsattari, S.M., Jones, C.K., Gati, J.S. and Leung, L.S. (2010) Functional networks in the anesthetized rat brain revealed by independent component analysis of resting-state FMRI. *Journal of neurophysiology*, **103**, 3398-3406.

Hutchison, R.M., Womelsdorf, T., Allen, E.A., Bandettini, P.A., Calhoun, V.D., Corbetta, M., Della Penna, S., Duyn, J.H., Glover, G.H., Gonzalez-Castillo, J., Handwerker, D.A., Keilholz, S., Kiviniemi, V., Leopold, D.A., de Pasquale, F., Sporns, O., Walter, M. and Chang, C. (2013a) Dynamic functional connectivity: Promise, issues, and interpretations. *Neuroimage,* **80**, 360–378.

Hutchison, R.M., Womelsdorf, T., Gati, J.S., Everling, S., Menon, R.S. (2013b) Resting-state networks show dynamic functional connectivity in awake humans and anesthetized macaques. *Hum Brain Mapp.,* **34**, 2154–2177.

Jo, H.J., Gotts, S.J., Reynolds, R.C., Bandettini, P.A., Martin, A., Cox, R.W. and Saad, Z.S. (2013) Effective preprocessing procedures virtually eliminate distance-dependent motion artifacts in resting state FMRI. *Journal of applied mathematics*.

Joel, S.E., Caffo, B.S., van Zijl, P. and Pekar, J.J. (2011) On the relationship between seed-based and ICA-based measures of functional connectivity. *Magn Reson Med.,* **66**, 644-657.

Jutras, M.J., Fries, P. and Buffalo, E.A. (2013) Oscillatory activity in the monkey hippocampus during visual exploration and memory formation. *Proc Natl Acad Sci USA*, **110**, 13144-13149.

Kannurpatti, S.S., Biswal, B.B., Kim, Y.R. and Rosen, B.R. (2008) Spatio-temporal characteristics of low-frequency BOLD signal fluctuations in isoflurane-anesthetized rat brain. *Neuroimage*, **40**, 1738-1747.

Kennan, R.P., Zhong, J. and Gore, J.C. (1994). Intravascular susceptibility contrast mechanisms in tissue. *Magn. Reson. Med*., **31**, 9–31.

Kim, S.G., Hendrich, K., Hu, X., Merkle, H. and Ugurbil, K. (1994) Potential pitfalls of functional MRI using conventional gradient-recalled echo techniques. *NMR in Biomed.,* **7**, 69-74.

Kinahan, P.E., Noll, D.C. (1999) A direct comparison between whole-brain PET and BOLD fMRI measurements of single-subject activation response. *NeuroImage*, **9**, 430-438.

Krishnan, G.P., Chauvette, S., Shamie, I., Soltani, S., Timofeev, I., Cash, S.S., Halgren, E. and Bazhenov, M. (2016) Cellular and neurochemical basis of sleep stages in the thalamocortical network. *Elife*, **5**, 18607.

Kuhlman, W.N. (1978) Functional topography of the human mu rhythm. Electroencephalogr. *Clin. Neurophysiol*., **44**, 83–93.

Kwong K. K., Belliveau J. W., Chesler D. A., Goldberg I. E., Weisskoff R. M., Poncelet B. P., Kennedy D. N., Hoppel B. E., Cohen M. S., Turner R., et al. (1992). Dynamic magnetic resonance imaging of human brain activity during primary sensory stimulation. *Proc. Natl. Acad. Sci. USA,* **89**, 5675-5679.

Lai, S., Hopkins, A.L., Haacke, E.M., Li, D., Wasserman, B.A., Buckley, P., Friedman, H., Meltzer, H., Hedera and Friedland, R. (1993) Identification of vascular structures as a major source of signal contrast in high resolution 2D and 3D functional activation imaging of the motor cortex at 1.5T: preliminary results. *Magn Reson Med.,* **30**, 387-392.

Lakatos, P., Shah, A.S., Knuth, K.H., Ulbert, I., Karmos, G. and Schroeder, C.E. (2005) An oscillatory hierarchy controlling neuronal excitability and stimulus processing in the auditory cortex. *J. Neurophysiol.,* **94**, 1904–11.

Lang, E.W., Tomé, A.M., Keck, I.R., Górriz-Sáez, J.M. and Puntonet, C.G. (2012) Brain connectivity analysis: a short survey. *Computational intelligence and neuroscience*, **8**.

Lauterbur, P. C. (1973) Image formation by induced local interactions: Examples employing nuclear magnetic resonance. *Nature,* **242**, 190-191.

Lee, S.P., Silva, A.C., Ugurbil, K. and Kim, S.G. (1999) Diffusion-weighted spin-echo fMRI at 9.4 T: microvascular/tissue contribution to BOLD signal changes. *Magn Reson Med.,* **42**, 919-928.

Legatt, A.D., Arezzo, J. and Vaughan. H.G., Jr (1980) Averaged multiple unit activity as an estimate of phasic changes in local neuronal activity: effects of volume-conducted potentials. *Journal of neuroscience methods,* **2,** 203–17.

Leopold, D.A., Murayama, Y. and Logothetis, N.K. (2003) Very slow activity fluctuations in monkey visual cortex: implications for functional brain imaging. *Cereb. Cortex,* **13**, 423–433.

Leskovec, J., Lang, K.J., Dasgupta, A. and Mahoney, M.W. (2008) Statistical properties of community structure in large social and information networks. *In Proceedings of the 17th international conference on World Wide Web*, **17**, 695-704.

Li, K., Guo, L., Nie, J., Li, G. and Liu, T. (2009) Review of methods for functional brain connectivity detection using fMRI. *Computerized Medical Imaging and Graphics*, **33**, 131-139.

Linden, H., Tetzlaff, T., Potjans, T.C., Pettersen, K.H., Grun, S., Diesmann, M. and Einevoll, G.T. (2011) Modeling the spatial reach of the LFP. *Neuron,* **72**, 859 –872.

Ljunggren, S. (1983) A simple graphical representation of Fourier-based imaging methods. *Journal of Magnetic Resonance*, **54**, 338-343.

Logothetis, N. K. (2002) The neural basis of the blood–oxygen–level–dependent functional magnetic resonance imaging signal. *Philosophical Transactions of the Royal Society of London B: Biological Sciences*, **357**, 1003-1037.

Logothetis, N.K. (2003) The underpinnings of the BOLD functional magnetic resonance imaging signal. *J. Neurosci. Off. J. Soc. Neurosci*., **23**, 3963–3971.

Logothetis, N.K., Guggenberger, H., Peled, S. and Pauls, J. (1999) Functional imaging of the monkey brain. *Nature Neurosci*., **2**, 555–562.

Lorente de Nó, R. (1947) A study of nerve physiology. *Studies from the Rockefeller Institute for Medical Research Part I, Vol. 131 (The Rockefeller Institute for Medical Research).*

Lowe, M.J., Mock, B.J. and Sorenson, J.A. (1998) Functional connectivity in single and multislice echoplanar imaging using resting-state fluctuations. *Neuroimage,* **7**, 119–132.

Lu, H., Zuo, Y., Gu, H., Waltz, J.A., Zhan, W., Scholl, C.A., Rea, W., Yang, Y. and Stein, E.A. (2007) Synchronized delta oscillations correlate with the resting-state functional MRI signal. *Proc Natl Acad Sci USA,* **104**, 18265–18269.

Magri, C., Schridde, U., Murayama, Y., Panzeri, S. and Logothetis, N.K. (2012) The amplitude and timing of the BOLD signal reflects the relationship between local field potential power at different frequencies. *J. Neurosci. Off. J. Soc. Neurosci.,* **32**, 1395–1407.

Majumdar, S. and Gore, J.C. (1987) Studies of diffusion in random fields produced by variations in susceptibility. *J. Magn. Reson*., **78**, 41-55.

McKeown, M.J., Makeig, S., Brown, G.G., Jung, T.P., Kindermann, S.S., Bell, A.J. and Sejnowski, T.J. (1997) Analysis of fMRI data by blind separation into independent spatial components (*No. NHRC-REPT-97-42*).

McRobbie, D.W., Moore, E.A., Graves, M.J. and Prince, M.R. (2008) MRI from Picture to Proton. *Cambridge university press*, 2nd edition.

Menon, R.S., Ogawa, S., Tank, D.W. and Ugurbil, K. (1993) 4 Tesla Gradient Recalled Echo Characteristics of Photic Stimulation-Induced Signal Changes in the Human Primary Visual Cortex. *Magn Reson Med.,* **30**, 380-386.

Mishra, A., Rogers, B.P., Chen, L.M. and Gore, J.C. (2014) Functional connectivity-based parcellation of amygdala using self-organized mapping: A data-driven approach. *Hum Brain Mapp.,* **35**, 1247–1260.

Murphy, K., Birn, R.M., and Bandettini, P.A. (2013) Resting-state fMRI confounds and cleanup. *Neuroimage*, **80**, 349-359.

Nácher, V., Ledberg, A., Deco, G. and Romo, R. (2013) Coherent delta-band oscillations between cortical areas correlate with decision making. *Proc Natl Acad Sci USA*, **110**, 15085-15090.

Neske, G.T. (2016) The slow oscillation in cortical and thalamic networks: mechanisms and functions. *Frontiers in neural circuits*, **9**, 88.

NessAiver, M. (1996) All you really need to know about MRI physics. *University of Maryland, Medical Center.*

Nir, Y., Fisch, L., Mukamel, R., Gelbard-Sagiv, H., Arieli, A., Fried, I. and Malach, R. (2007) Coupling between neuronal firing rate, gamma LFP, and BOLD fMRI is related to inter-neuronal correlations. *Curr. Biol.,* **17**, 1275–1285.

Nir, Y., Mukamel, R., Dinstein, I., Privman, E., Harel, M., Fisch, L., Gelbard-Sagiv, H., Kipervasser, S., Andelman, F., Neufeld, M.Y., Kramer, U., Arieli, A., Fried, I. and Malach, R. (2008) Interhemispheric correlations of slow spontaneous neuronal fluctuations revealed in human sensory cortex. *Nat Neurosci.,* **11**, 1100–1108.

Ogawa, S., Lee, T.M. and Barrere, B. (1993a) The sensitivity of magnetic resonance image signals of a rat brain to changes in the cerebral venous blood oxygenation. *Magn. Reson. Med.,* **29**, 205–210.

Ogawa, S., Lee, T.M., Kay, A.R. and Tank, D.W. (1990b) Brain magnetic resonance imaging with contrast dependent on blood oxygenation. *Proc Natl Acad Sci USA,* **87**, 9868-9872.

Ogawa, S., Lee, T.M., Nayak, A.S. and Glynn, P. (1990a) Oxygenation-sensitive contrast in magnetic resonance images of rodent brain at high magnetic fields. *Magn. Reson. Med.,* **14**, 68–78.

Ogawa, S., Menon, R.S., Tank, D.W., Kim, S.G., Merkle, H., Ellermann, J.M. and Ugurbil, K. (1993b) Functional brain mapping by blood oxygenation level-dependent contrast magnetic resonance imaging. *Biophys. J.,* **64**, 800–12.

Palva, J., Palva, S. and Kaila, K. (2005) Phase synchrony among neuronal oscillations in the human cortex. *J. Neurosci.,* **25**, 3962–72.

Pan, W.J., Thompson, G., Magnuson, M., Majeed, W., Jaeger, D. and Keilholz, S. (2011) Broadband local field potentials correlate with spontaneous fluctuations in functional magnetic resonance imaging signals in the rat somatosensory cortex under isoflurane anesthesia. *Brain Connect,* **1**, 119–131.

Parkes, L.M., Schwarzbach, J.V., Bouts, A.A., Deckers, R.H.R., Pullens, P., Kerskens, C.M., Norris, D.G (2005) Quantifying the spatial resolution of the gradient echo and spin echo BOLD response at 3 Tesla. *Magn. Reson. Med.,* **54**, 1465–1472.

Pauling, L. and Coryell, CD. (1936) The magnetic properties and structure of hemoglobin, oxygenated hemoglobin, and carbonmonoxygenated hemoglobin. *Proc. Natl. Acad. Sci. U.S.A.,* **22**, 210-236.

Power, J.D., Cohen, A.L., Nelson, S.M., Wig, G.S., Barnes, K.A., Church, J.A., Vogel, A.C., Laumann, T.O., Miezin, F.M., Schlaggar, B.L. and Petersen, S.E. (2011) Functional network organization of the human brain. *Neuron*, **72**, 665–678.

Preston, A.R. and Eichenbaum, H. (2013) Interplay of hippocampus and prefrontal cortex in memory. *Current Biology*, **23**, 764-773.

Prielmeier, F., Merboldt, KD., Hänicke, W. and Frahm, J. (1993) Dynamic high-resolution MR imaging of brain deoxygenation during transient anoxia in the anesthetized rat. *J. Cereb. Blood Flow Metab.,* **13**, 889–894.

Purcell, E. M., Torrey, H. C, and Pound, R. V. (1945) Resonance absorption by nuclear magnetic moments in a solid. *Phys. Rev*., **69**, 37-38.

Raichle, M.E., MacLeod, A.M., Snyder, A.Z., Powers, W.J., Gusnard, D.A. and Shulman, G.L. (2001) A default mode of brain function. *Proc. Natl. Acad. Sci. USA*, **98**, 676–82.

Ray, S. and Maunsell, J.H. (2012) Differences in gamma frequencies across visual cortex restrict their possible use in computation. *Neuron,* **67**, 885–896.

Salmelin, R. and Hari, R. (1994) Spatiotemporal characteristics of sensorimotor neuromagnetic rhythms related to thumb movement. *Neuroscience,* **60**, 537–550.

Sanders, R.D., Tononi, G., Laureys, S. and Sleigh, J.W. (2012) Unresponsiveness ≠ unconsciousness. *Anesthesiology: The Journal of the American Society of Anesthesiologists,* **116**, 946-959.

Sherman, M.A., Lee, S., Law, R., Haegens, S., Thorn, C.A., Hämäläinen, M.S., Moore, C.I. and Jones, S.R. (2016) Neural mechanisms of transient neocortical beta rhythms: Converging evidence from humans, computational modeling, monkeys, and mice. *Proc Natl Acad Sci USA*, **16**, 04135.

Shmuel, A. and Leopold, D.A. (2008) Neuronal correlates of spontaneous fluctuations in fMRI signals in monkey visual cortex: Implications for functional connectivity at rest. *Hum Brain Mapp*., **29**, 751–761.

Sirota, A., Montgomery, S., Fujisawa, S., Isomura, Y., Zugaro, M. and Buzsaki, G. (2008) Entrainment of neocortical neurons and gamma oscillations by the hippocampal theta rhythm. *Neuron*, **60**, 683–697.

Sirota, A., Montgomery, S., Fujisawa, S., Isomura, Y., Zugaro, M. and Buzsaki, G. (2008) Entrainment of Neocortical Neurons and Gamma Oscillations by the Hippocampal Theta Rhythm. *Neuron*, **60**, 683-697.

Sporns, O., Honey, C.J. and Kotter, R. (2007) Identification and classification of hubs in brain networks. *PLoS One*, **2**, 1049.

Stehling M. K., Turner R., and Mansfield P. (1991). Echo-planar imaging: Magnetic resonance imaging in a fraction of a second. *Science***, 254**, 43-50.

Steriade, M., Nunez, A. and Amzica, F. (1993) A novel slow (< 1 Hz) oscillation of neocortical neurons *in vivo*: depolarizing and hyperpolarizing components. *J. Neurosci.,* **13**, 3252–3265.

Suetens, P. (2009) Fundamentals of medical imaging. *Cambridge university press,* 2nd edition.

Thompson, G.J., Pan, W-J. and Keilholz, S.D. (2015) Different dynamic resting state fMRI patterns are linked to different frequencies of neural activity. *Journal of Neurophysiology*, **114**, 114-24.

Thulborn, KR., Waterton, JC., Mattews, PM. and Radda, GK. (1982) Oxygenation Dependence of the Transverse Relaxation Time of Water Protons in Whole Blood at High Field. *Biochem Biophys Acta*., **714**, 265-270.

Timofeev, I., Bazhenov, M., Seigneur, J. and Sejnowski, T. (2012) Neuronal synchronization and thalamocortical rhythms in sleep, wake and epilepsy. *Jasper's Basic Mechanisms of the Elilepsies [Internet],* 4th edition.

Tort, A.B., Komorowski, R., Eichenbaum, H. and Kopell, N. (2010) Measuring phase-amplitude coupling between neuronal oscillations of different frequencies. *J. Neurophysiol.,* **104**, 1195–210.

Tort, A.B., Kramer, M.A., Thorn, C., Gibson, D.J. and Kubota, Y. (2008) Dynamic cross-frequency couplings of local field potential oscillations in rat striatum and hippocampus during performance of a T-maze task. *Proc. Natl. Acad. Sci. USA,* **105**, 20517–22.

Turner, R., LeBihan, D., Moonen, C.T.W., DesPres, D. and Frank, J. (1991) Echo-planar time course MRI of cat brain oxygenation changes. *Magn. Reson. Med.,* **22**, 159–166.

Twieg D (1983) The k-trajectory formulation of the NMR imaging process with applications in analysis and synthesis of imaging methods. *Medical Physics*, **10**, 610–21.

Uğurbil, K., Adriany, G., Andersen, P., Chen, W., Gruetter, R., Hu, X., Merkle, H., Kim, D.S., Kim, S.G., Strupp, J. and Zhu, X.H. (2000) Magnetic resonance studies of brain function and neurochemistry. *Annual review of biomedical engineering*, **2**, 633-660.

van den Heuvel, M.P., Stam, C.J., Boersma, M. and Hulshoff Pol, H.E. (2008) Small-world and scale-free organization of voxel-based resting-state functional connectivity in the human brain. *Neuroimage,* **43**, 528–39.

van Zijl, P.C.M., Efefe, S.M., Ulatowski, J.A., Oja, J.M.E., Ulug, A.M., Traystman, R.J. and Kauppinen, R.A. (1998) Quantitative assessment of blood flow, blood volume and blood oxygenation effects in functional magnetic resonance imaging. *Nat. Med.,* **4**, 159–167.

Volgushev, M., Chauvette, S., Mukovski, M. and Timofeev, I. (2006) Precise long-range synchronization of activity and silence in neocortical neurons during slow-wave oscillations. *J. Neurosci.,* **26**, 5665–5672.

Wang, J., Zuo, X. and He, Y. (2010) Graph-based network analysis of resting-state functional MRI. *Frontiers in systems neuroscience*, **4**.

Wang, L., Saalmann, Y.B., Pinsk, M.A., Arcaro, M.J. and Kastner, S. (2012) Electrophysiological low-frequency coherence and cross-frequency coupling contributes to BOLD connectivity. *Neuron,* **76**, 1010–1020.

Wang, Z. and Roe, A.W. (2013). Columnar specificity of microvascular oxygenation and blood flow response in primary visual cortex: evaluation by local field potential and spiking activity. *J Cereb Blood Flow Metab.,* **32**, 6-16.

Wang, Z., Chen, L.M., Negyessy, L., Friedman, R.M., Mishra, A., Gore, J.C. and Roe, A.W. (2013) The relationship of anatomical and functional connectivity to resting-state connectivity in primate somatosensory cortex. *Neuron,* **78**, 1116–1126.

Wilson, G.H., 3rd, Yang, P.F., Gore, J.C. and Chen, L.M. (2016) Correlated inter-regional variations in low frequency local field potentials and resting state BOLD signals within S1 cortex of monkeys. *Hum Brain Mapp.,* **37**, 2755–2766.

Winkler, M. L., Ortendahl, D. A., Mills, T. C., Crooks, L. E., Sheldon, P. E., Kaufman, L. and Kramer, D. M. (1988) Characteristics of partial flip angle and gradient reversal MR imaging. *Radiology*, **166**, 17-26.

Yacoub, E., Shmuel, A., Pfeuffer, J., Van De Moortele, P., Adriany, G., Andersen, P., Vaughan, J., Merkle, H., Ugurbil, K., Hu, X. (2001) Imaging brain function in humans at 7 Tesla. *Magn Reson Med.,* **45**, 588-594.

Yan, C., Liu, D., He, Y., Zou, Q., Zhu, C., Zuo, X., Long, X. and Zang, Y. (2009) Spontaneous brain activity in the default mode network is sensitive to different resting-state conditions with limited cognitive load. *PloS one*, **4**, 5743.

Yeo, B.T., Krienen, F.M., Sepulcre, J., Sabuncu, M.R., Lashkari, D., Hollinshead, M., Roffman, J.L., Smoller, J.W., Zollei, L., Polimeni, J.R., Fischl, B., Liu, H. and Buckner, R.L. (2011) The organization of the human cerebral cortex estimated by intrinsic functional connectivity. *J Neurophysiol.,* **106**, 1125–1165.

Zhang, N., Gore, J.C., Chen, L.M. and Avison, M.J. (2007) Dependence of BOLD signal change on tactile stimulus intensity in SI of primates. *Magn Reson Imaging,* **25**, 784–794.

Zhong, J., Kennan, R.P., Fulbright, R.K. and Gore, J.C. (1998) Quantification of intravascular and extravascular contributions to BOLD effects induced by alteration in oxygenation or intravascular contrast agents. *Magn Reson Med.,* **40**, 526-536.

Zhu, X.H, Kim, S.G., Andersen, P., Ogawa, S., Ugurbil, K. and Chen, W. (1998) Simultaneous oxygenation and perfusion imaging study of functional activity in primary visual cortex at different visual stimulation frequency: Quantitative correlation between BOLD and CBF changes. *Magn. Reson. Med.* 1998, **40**, 703–711.

CHAPTER II

HIGH SPATIAL CORRESPONDENCE BETWEEN BOLD AND LFP IN STIMULATION

Abstract

Functional MRI studies rely on detecting hemodynamic changes as revealed by BOLD signals to infer underlying changes in local neuronal activity. The local spatial specificity and resolution are dependent on limitations introduced by non-neuronal factors. LFPs are electrophysiological signals generated by the summed electric currents flowing from populations of neurons within small volumes of nervous tissue around the recording electrode tips, and are considered more direct indicators of neuronal activity. Understanding how BOLD signals are related to electrical activity of neuron populations is essential for the quantitative interpretation of fMRI data. Here, we evaluated the spatial extents of LFPs in functionally distinct areas 3b and 1 of S1 cortex in new world monkeys, using two 49-channel multi-electrode arrays, and in separate experiments we performed fMRI at very high field strength (9.4T) to obtain very high resolution spatial extents of stimulated activations. Images of both modalities were co-registered within 0.10 mm accuracy. We are thereby able to relate fMRI data directly to a 'gold standard' electrophysiological measurements LFPs with good sensitivity and spatial resolution. The spatial extents of BOLD and LFP responses of S1 cortex were fitted with Gaussian point spread functions (PSFs). We found that the mean full-width at half maximum (FWHM) of the fitted PSFs in both LFP and very high resolution BOLD fMRI responses at stimulus condition were around 1 mm, in which stimulus responses in area 3b were stronger and more mediolateral focal than those in area 1. In addition, our results showed that the PSFs of the BOLD response in very high resolution (0.274×0.274 mm^2) were significantly narrower than those in relatively lower resolution imaging (0.547×0.547 mm^2), due to partial volume effects, indicating that data acquisition methods for higher resolution functional images increase the spatial specificity of BOLD fMRI. Finally, Wilcoxon signed-rank test showed that there was no significant difference on PSFs between LFP and very high resolution BOLD fMRI at 9.4 T in the stimulus condition, and the reproducibility and stability of stimulus-evoked activation locations within and across both modalities were robust.

Introduction

FMRI is well established as a neuroimaging technique for the detection and delineation of regions in the brain that change their level of activation in response to specific experimental conditions [Ogawa et al., 1990; Bandettini et al., 1992; Kwong et al., 1992]. The dominant form of fMRI uses the BOLD contrast, which detects functional hemodynamic changes in the brain based on the differences in magnetic properties between oxygen-rich and oxygen-poor blood, and is considered an indirect indicator of changes in neuronal activity. Specifically, BOLD measurements are driven by blood flow, blood volume and oxygenation changes that are secondary to metabolic changes and energy use caused by neural activity [Buxton, 2013]. Stimulus-evoked fMRI responses usually rely on detecting BOLD signal changes, which reflect hemodynamic processes, and thus are indirect indicators of neuronal activity. The measured extents of BOLD activations depend on the integrated contributions from the intrinsic spatial distributions of the neural activity involved, the effects of converting neural electrical activity to spatial distributions of metabolic and hemodynamic changes that then affect MRI signals, and the effects of image acquisitions and reconstruction with limited resolution, but the relative contributions of these to detected signals remain obscure. Precise interpretations of fMRI studies require a better understanding of the quantitative relationships between BOLD signal changes and their corresponding electrophysiological signatures [Shi et al., 2017]. On the other hand, local field potentials are electrophysiological signals generated by the summed electric currents flowing from populations of neurons within small volumes of nervous tissue around the recording electrode tips [Legatt et al, 1980].

Although the exact relationship between the measured fMRI signals and the underlying neuronal activity remains elusive at multiple levels, there is consensus that local field potential activity contributes the most to the fMRI signal [Logothetis et al., 2001; Logothetis et al., 2003; Nir et al., 2007]. The most effective way to investigate such relationship is to simultaneously acquire fMRI signals and electrophysiological recordings. Most research in the past has studied the temporal relationships among BOLD fMRI signals, LFPs and spike activity, using single or multiple electrodes [Leopold and Maier, 2012; Scholvinck et al., 2013; Shmuel and Leopold, 2008; Magri et al., 2012]. More recently, there has been an increasing interest in conducting multi-channel electrode array experiments to reveal the local functional architecture of the brain and further investigate the spatial relationships between fMRI and electrophysiological signals

[Chernov et al., 2016]. Extending electrode recording technique using multi-channel electrode array recording for quantitative comparisons of spatial extents between LFP and BOLD fMRI responses has the potential to better understand how BOLD signals are related to electrical activity of neuron populations, and to quantitatively interpret fMRI data.

The purpose of this study was to evaluate the spatial extents of BOLD fMRI with very high resolution at very high field strength (9.4T) in the stimulated condition, in the primary somatosensory cortex of non-human primate, and to compare with those of local field potentials to the same conditions and the same brain region. To this end, we utilized two 7×7 multi-channel electrode arrays to map signal fluctuations in LFPs in response to 8 Hz vibrotactile stimulation of single digits in functionally distinct areas 3b and 1 of S1 cortex in anesthetized squirrel monkeys, and evaluated the spatial extents of single digit LFP response fields by quantifying their power spectrum. In separate experiments, we performed BOLD fMRI at 9.4 T to obtain very high resolution spatial extents of BOLD signals at stimulus-evoked condition. We estimated that the mean FWHM of the fitted PSFs of BOLD and LFP responses in S1 cortex of new world monkey at stimulus-evoked condition were around 1 mm, in which stimulus responses in area 3b were stronger and more mediolaterally focal than those in area 1. In addition, we found that the PSFs of the BOLD response in very high resolution (in plane resolution of 0.274 × 0.274 mm^2) were significantly narrower than those in relatively lower resolution images (in plane resolution of 0.547 × 0.547 mm^2) due to partial volume effects. Our results showed no difference on PSFs between LFP and BOLD fMRI with very high resolution at 9.4 T at both stimulus and resting-state conditions. Activation maps of both modalities were co-registered within 0.10 mm accuracy. The mean distance of activation centers between BOLD and LFP was around 0.35 mm. The high spatial correspondence between BOLD and LFP are consistent with findings regarding the great contribution of LFP activity to the fMRI signal [Logothetis et al., 2001; Logothetis et al., 2003; Nir et al., 2007; Shmuel and Leopold, 2008; Magri et al., 2012], suggesting that BOLD fMRI with very high resolution at very high field spatially directly reflects the neuronal activity.

Methods

Animal Preparation

Six squirrel monkeys (Saimiri bolivians) were included in this study and all underwent functional MR imaging scans. Four of the six monkeys underwent microelectrode electrophysiological mapping and 98-channel microelectrode array recording sessions. Animals were pre-anesthetized with ketamine hydrochloride (10 mg/kg)/atropine (0.05 mg/kg) and then anesthetized with 0.5-1.2% of isoflurane to maintain a stable physiological condition for both MRI scans and electrophysiological experiments. Although the actual level may vary across experiments, we typically maintained light anesthesia around 0.7-0.8% during our functional MRI and electrophysiology data acquisitions. The anesthetized animals were intubated and artificially ventilated. After intubation, each animal was placed in a custom-designed MR cradle with its head secured using ear bars and an eye bar. Lactated Ringer's solution was infused intravenously (2-3 ml/h/kg) to prevent dehydration during the course of the study. Arterial blood oxygen saturation and heart rate (Nonin, Plymouth, MN), electrocardiogram, end-tidal CO_2 (ET-CO_2; 22–26 mmHg; Surgivet, Waukesha, WI), and respiration (SA Instruments, Stony Brook, NY) were externally monitored and maintained. Body temperature was monitored (SA Instruments) and maintained between 37.5 and 38.5°C via a circulating water blanket (Gaymar Industries, Orchard Park, NY). Real-time monitoring was maintained from the time of induction of anesthesia until full recovery. Detailed procedures have been described in previous publications [Shi et al., 2016]. All experimental procedures were in compliance with and approved by the Institutional Animal Care and Use Committee of Vanderbilt University, and followed the guidelines of the National Institutes of Health Guide for the care and use of laboratory animals.

Stimulus Presentation Protocol

Each animals' fingers were secured by gluing small pegs to the fingernails and fixing these pegs firmly in plasticine, leaving the glabrous surfaces available for vibrotactile stimulation by a rounded plastic probe (2 mm diameter) connected to a piezoelectric device (Noliac, Kvistgaard, Denmark), which was driven by a Grass S48 square wave stimulator (Grass-Telefactor, West Warwick, RI). For fMRI data acquisitions, vertical indentations (0.34 mm displacement) of a probe at 8 Hz rate (with 20 ms pulse duration) were presented as blocks of 30 sec on and then 30 sec off.

Seven blocks were typically presented within one imaging run. The timing of the presentation of stimuli was externally controlled by the MR scanner and was synchronized to image acquisition. The same stimulus presentation paradigm was applied during later electrophysiological recordings. Each stimulation trial consisted of 20 repeats of 30 sec on/off blocks. Typically, 10 trials were collected for each digit.

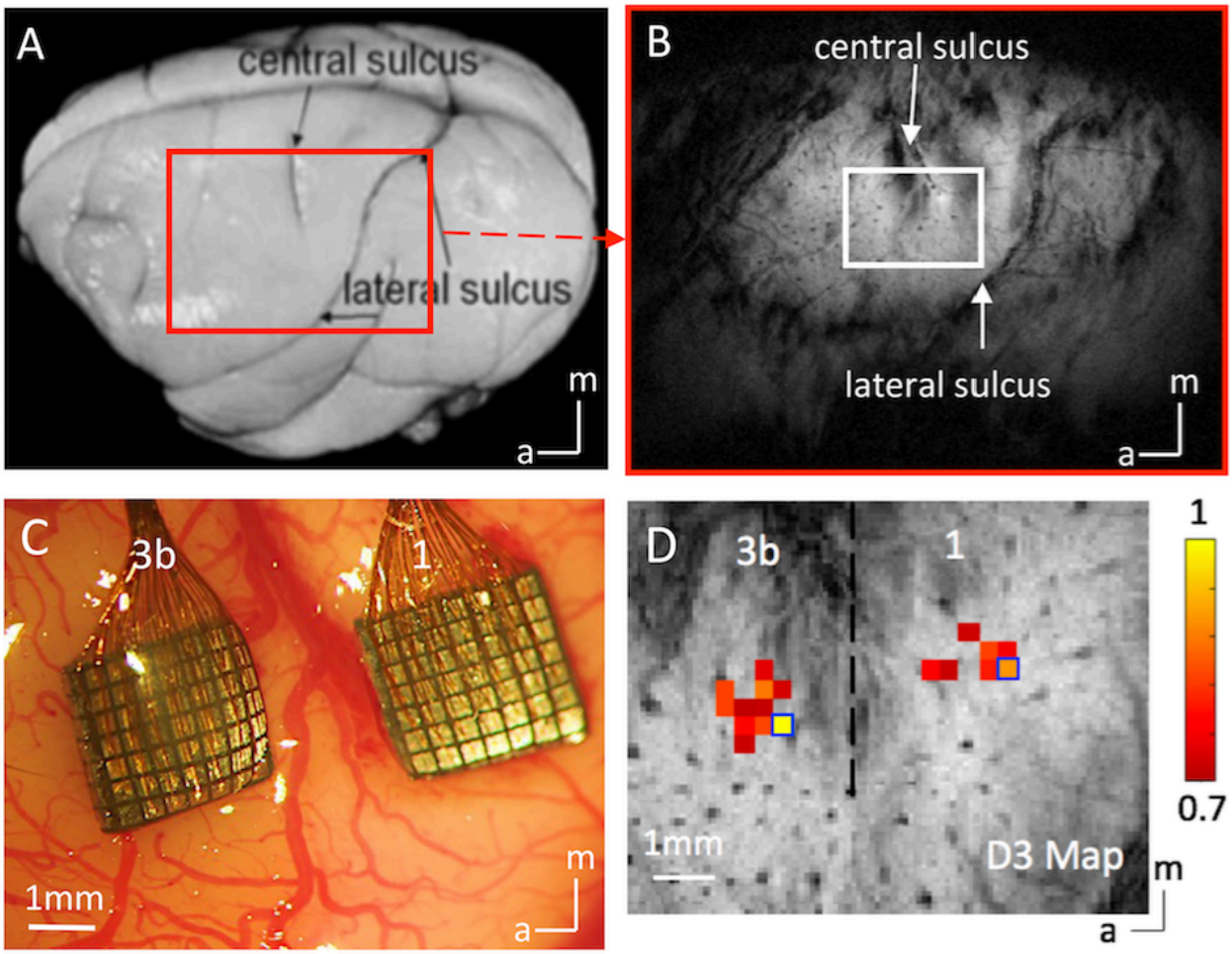

Figure 8 Experimental set up for mapping areas 3b and 1 of S1 cortex with sub-millimeter resolution fMRI and 98 channel Utah array. (A) Major landmarks used to identify digit regions in areas 3b and 1 of S1 are visible on the postmortem squirrel monkey brain. The red box indicates the imaging field of view. (B) In an oblique coronal image acquired with T_2^* weighting, sulci and surface and trans-cortical vessels appear as dark lines and dots. (C) Blood vessel map shows the two 7×7 multi-channel electrode arrays were inserted in the digit regions of areas 3b and 1 under surgical microscope in one representative monkey. (D) Corresponding BOLD fMRI activation map to vibrotactile stimulation of the D3 distal finger pad in areas 3b and 1 of S1 cortex. Normalized % signal change maps were thresholded at 0.7. Dotted black line indicates the approximate border between areas 3b and 1. Blue boxes show the selected seed voxels used in resting state functional connectivity analysis. Scale bar, 1 mm; a, anterior; m, medial.

FMRI Data Acquisition and analysis

MR imaging was performed with a 9.4 T 21 cm bore Varian Inova magnet (Varian Medical Systems, Palo Alto, CA), using a 3-cm surface transmit–receive coil secured over the somatosensory cortex. Scout images obtained using a fast gradient-echo sequence were used to define a volume covering the primary somatosensory cortex in which static magnetic field homogeneity was optimized, and to plan oblique slices for structural and functional EPI imaging (Figure 8A-B). T_2^*-weighted gradient-echo structural images [repetition time (TR) = 200 ms, echo time (TE) = 16 ms, four slices, FOV = 35 × 35 mm^2, 512 × 512 matrix, spatial resolution = 0.068 × 0.068 × 2 mm^3, number of excitations = 6] were acquired to identify venous structures on the cortical surface to help locate S1 cortex, and as structural features for co-registration of fMRI images. Within each imaging session, multiple runs (up to 6) of stimulus evoked fMRI data were acquired with identical image acquisition sequences (gradient echo-planar image, GE-EPI), parameters (TR =750 ms, TE =16 ms) and slice placement. All images were obtained at two different imaging resolutions: 0.547 × 0.547 × 2 mm^3 (low resolution, number of excitations = 2) and 0.274 × 0.274 × 2 mm^3 (high resolution, number of excitations = 4). Each low resolution stimulation run contains 300 continuous image volumes, while each high resolution run contains 150 continuous volumes (Figure 9A). MR Images were reconstructed on the MR console (Varian VnmrJ) and exported to Matlab (Mathworks, Natick, MA) for analysis.

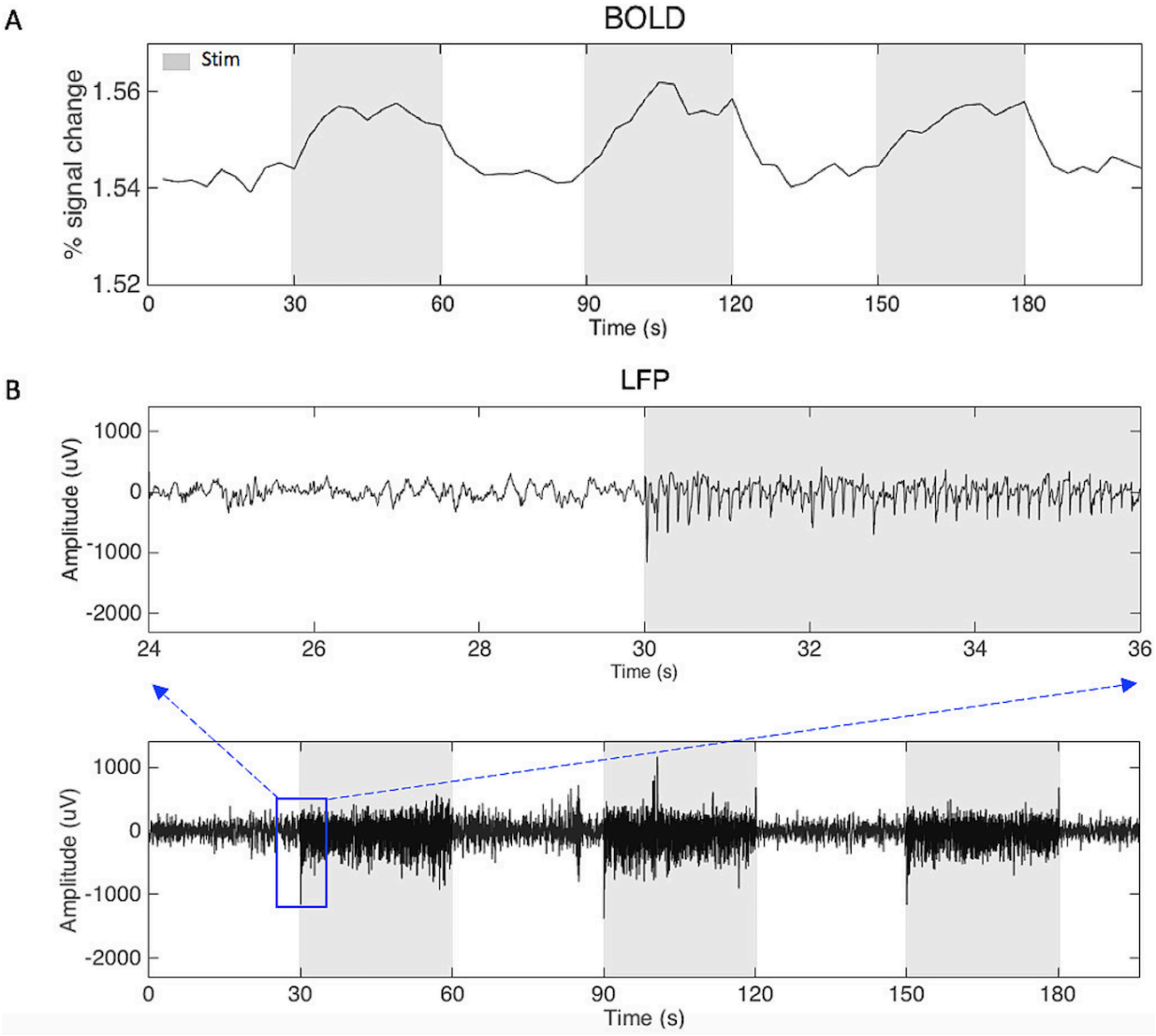

Figure 9 Representative BOLD and local field potential signal changes to vibrotactile stimuli. (A) Time series of BOLD signal changes to 8 Hz vibrotactile stimuli of single digit extracted from area 3b voxel. (B) Recordings of raw broadband local field potential in response to the identical tactile stimulation as applied in BOLD mapping experiment shown in A. Blue box shows the sampling window.

Standard preprocessing steps were applied to the raw fMRI signals. Slice timing correction was performed following slice-by-slice motion correction. Six translation and rotation parameters were used to regress out temporal variations caused by motion. Time courses were drift corrected using a linear model fitted to each time course. The RETROICOR method [Glover et al., 2000] was used to correct for physiological noise using the respiration pattern recorded during the scan. No spatial smoothing was applied.

For stimulation runs, we computed activation maps based on the percentage of BOLD signal change between pre-stimuli periods (seven out of ten imaging volumes prior to stimulus onset) and stimuli presentation periods (10 image volumes). The activation response map was then up-sampled to the anatomic MRI image (0.068×0.068 mm^2) for further sub-voxel processing and display. Within each fMRI stimulation run, the percentage of BOLD signal change in each of the cortical areas (areas 3b and 1) was normalized to its own maximum value. Normalized percentage BOLD signal changes were then used in the group analyses.

Electrophysiological mapping and recording

Under anesthesia, a craniotomy was performed over the imaged region to expose the cortex for microelectrode mapping and recordings. During the initial electrophysiological mapping session, a series of single electrode penetrations were placed around the cortex surrounding the central sulcus for characterizing the neural preferred stimulus (e.g., light touch or stroke), response (e.g. short or long lasting), and their receptive fields properties (e.g., digit 1-5 or face). In each animal, areas 3b and 1 were systematically mapped. Single epoxylite-coated tungsten microelectrodes (FHC Inst, Bowdoinham, ME) with exposed standard sharp tip (< 3 μm) of ~1 M Ω impedance penetrated ~800 μm deep into the cortex of areas 3b and 1. Receptive fields of neurons were identified by palpating skin areas on the contralateral hand to the recording side while listening to the audio amplifier for spike activity and viewing traces of action potentials on a display. After completing the mapping, we were able to identify areas 3b and 1 and areal borders based on the characteristics of receptive field properties and somatotopic organization of the digits [Kaas et al., 1984; Friedman et al., 2008]. These initial qualitative mapping results then guided the placements of two 7×7 channel Utah micro-electrode arrays in each animal (Figure 8C).

We determined the array placement targets in areas 3b and 1 by co-registering high-resolution optical blood vessel images with the MRI anatomic images using anatomical land-marks and surface blood vessel pattern. Guided by MRI maps and blood vasculature pattern, two 7×7 multi-channel Utah electrode arrays (98 channels in total, spacing between each electrode = 400 μm) were carefully inserted into areas 3b and 1 cortex. Once the arrays were inserted, we allowed the cortex to recover from insult for at least two hours before our recording session started. Broad band electrical signals were recorded using a Multi-channel Cerebus Neural Signal Processor system (Black Rock, Millard county, Utah) in which signals were passed through a unit-gain head-stage and a preamplifier through which each input channel was separated into two output channels that underwent different analog filtering, with one channel recording the higher frequencies of neuronal spikes and the other channel recording the lower frequencies of LFPs. In all cases, voltages were measured against a local reference inside the chamber. For single digit LFP stimulus recordings, a total of 6-8 trials were recorded for each subject. Within each trial, 10 stimuli (each 30 sec duration) were presented.

Local Field Potentials Analysis

Local field potential signals were sampled at 500 Hz, and then band-pass filtered between 1 Hz (two pole Butterworth filter) and 150 Hz (four pole Butterworth filter) for quantification. Figure 9B shows an example of LFP broadband (1-150 Hz) raw data, including 30 sec of pre-stimulus (rest) period and 30 sec of stimulus presentation. A time-frequency analysis was conducted to illustrate the temporal structure of the LFP signals and their stimulus response preferences. A Fourier transform was performed on single trials and the resulting single-trial spectrograms were averaged. Computed spectrograms of stimulus-evoked LFPs under stimulus conditions were transformed into a dB scale ($10 \times \log_{10}$) and used for further analysis. To estimate more accurately the mean power of the steady-state LFP responses, we excluded the data from the first 10 sec after the stimulus onset in our calculation, according to previous observations [Snyder, 1992].

Measurements of the Point spread Function of BOLD fMRI signals in stimulation

The PSFs of the single digit tactile stimulation evoked BOLD fMRI activation maps were measured in both areas 3b and 1. We first identified activation foci in areas 3b and 1, whose shapes could be well approximated as elliptical. In each animal, activation maps of three different digit tips were typically obtained. A threshold of 0.7 was used to identify the center of mass in each ROI. The axis along the individual digit activation centers was then determined as the lateral to medial axis within each area (3b and 1). The perpendicular anterior-posterior direction of this axis was then determined along the digit bottom to tip representation. From the fitting, the center of mass, coordinates and the major (in the lateral to medial direction) and minor (in the anterior to posterior direction) axes of the ellipse were determined, and all values above 0.2 along the major and minor axes within the subregion were used in the subsequent Gaussian fitting. The voxel-to-voxel spatial distributions of percentage of BOLD signal changes along the major and minor axes were fit with Gaussian functions. The full-width of half maximum (FWHM) of each fitted Gaussian point-spread function was then computed.

Quantification of the Point spread Function of Local Field Potentials in Stimulation

The same spatial ellipsoid fitting method was used to quantify the PSFs of LFP signals. To estimate the spatial extents of LFP responses in the stimulus condition, we began by examining the mean LFP power spectral density from all 98 channels together for the three brain states (pre-stimulus, stimulus presentation and resting-state). Multi-channel electrode array response maps were computed based on the percentages of signal power changes between 20 sec of stimuli presentations and 20 sec of the pre-stimuli periods for single digit stimulations. Activation maps were then resampled at higher resolution (0.10×0.10 mm^2) for further sub-voxel processing. Within each LFP stimulus run, the percentages of signal power changes of cortical activation areas were normalized to their maximum values during each run. A similar approach as described above was used to compute the point-spread functions of stimulus local field potential responses of areas 3b and 1 in S1 cortex.

Comparison of locations of BOLD versus LFP activations

To examine how reproducible the activation centers (of area 3b and area 1) were across BOLD and LFP acquisitions under stimulus conditions, we used a group analysis based on the mean and standard deviation of the center distances across all subjects and study sessions. Coregistrations of fMRI activation maps with LFP activation maps were accomplished using anatomical land-marks, surface blood vessel patterns, and a point-based co-registration algorithm. Forty to 80 pairs of reference points were used as landmarks in the 2D geometric nonlinear transformation. Apparent black dots on the T_2^* MR structural images were caused by transcortical vessels. Their corresponding landmarks were visible on the LFP blood vessel maps as well. After coregistration, the point-to-point spatial offsets (square distances) of the predefined 40-80 reference pairs were computed as coregistration accuracy. For both BOLD and LFP foci, the stabilities of the activation centers were quantified by the spatial shifts (distance) between the centers from all stimulus runs within each session. One x-y coordinate was computed for each experimental session (day) by averaging coordinates of centers across all stimulus runs within that day. We then quantitatively compared the mean activation center coordinates between BOLD and LFP.

Results

Comparable Spatial Profiles of BOLD and LFP Responses to Stimulation in Areas 3b and 1

To compare spatial response profiles to external stimuli between fMRI and LFPs, we estimated the FWHMs along the major and minor axes and the area and ratio of axes for each BOLD activation and the corresponding LFP responses. Figure 10A-D shows examples of fMRI and LFP activation maps to D3 tactile stimulation in both areas 3b and 1 of the same subject. Figure 10C and D shows 3D plots of the overall activation patterns in areas 3b and 1 and their local spatial profiles. By comparing measurements across all studies, we found no significant differences between BOLD and LFP estimates of the FWHMs along major and minor axes (Figure 10E and G), areas (Figure 10F), or major/minor axis ratio (Figure 10H, comparing blue and green columns in Figure 10E-H) in both area 3b and area 1. For both BOLD and LFP responses, activation foci in area 3b have an elongated oval shape, with the major axis orientated in a lateral to medial direction that is along the line of digit tip-to-tip representations. In contrast, activation foci in area 1 are aligned in an anterior to posterior direction, along the line distinguishing digit bottom from top and orthogonal to the inter-areal border.

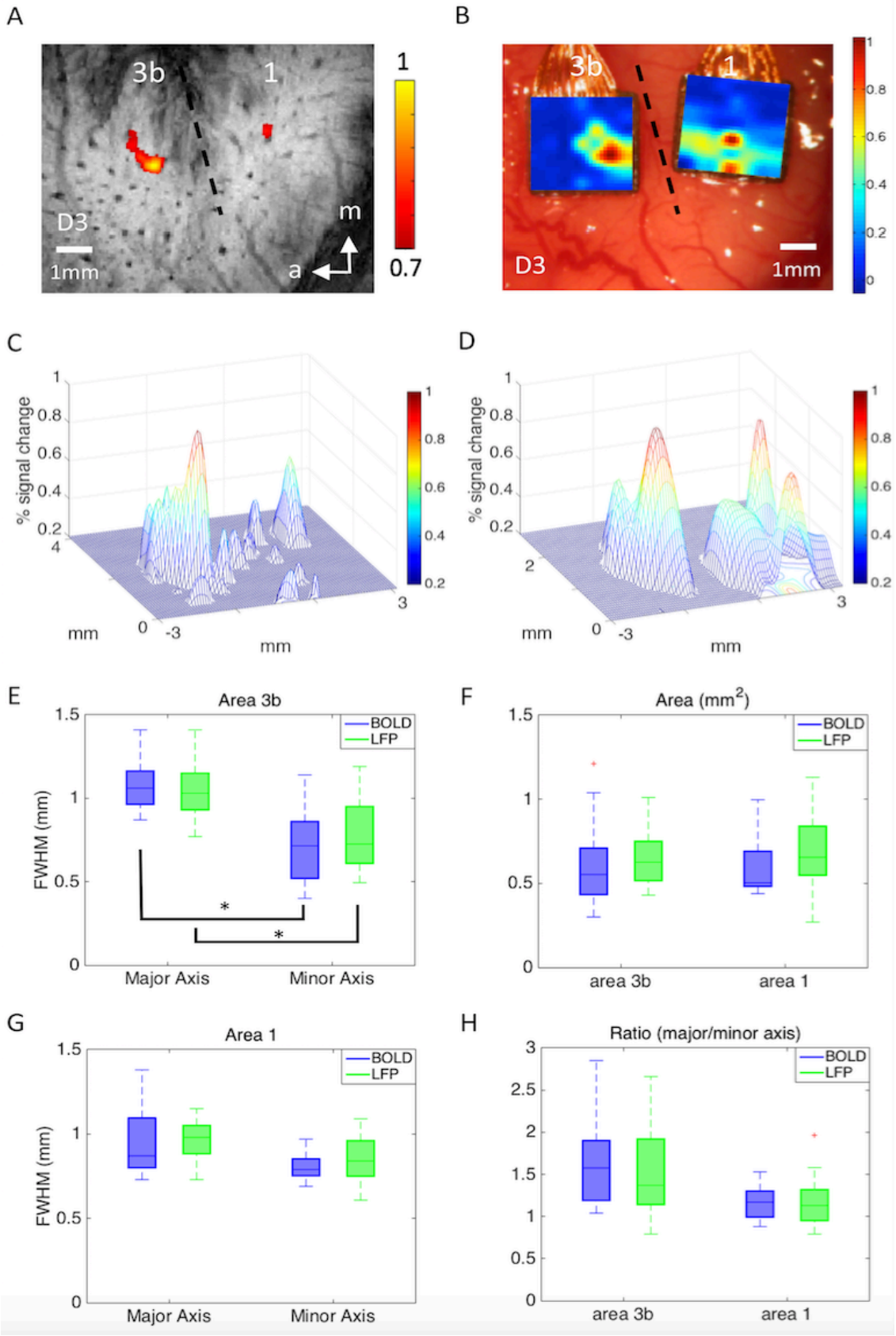
A
3b
1
1
0.7
D3
1mm
m
a
B
3b
1
D3
1mm
C
% signal change
mm
mm
D
% signal change
mm
mm
E
Area 3b
FWHM (mm)
BOLD
LFP
Major Axis
Minor Axis
F
Area (mm2)
BOLD
LFP
area 3b
area 1
G
Area 1
FWHM (mm)
BOLD
LFP
Major Axis
Minor Axis
H
Ratio (major/minor axis)
BOLD
LFP
area 3b
area 1

Figure 10 Spatial extents of tactile stimulus evoked BOLD activation in areas 3b and 1. One case is shown in A-D; entire population data are given in E-H. (A) BOLD activations in response to vibrotactile stimulation of digit 3 distal fingertip in areas 3b and 1. Activation map is thresholded at 0.7 of normalized % signal changes, with a peak value of 1. Dotted line represents estimated inter-areal border between areas 3b and 1. (B) Corresponding LFP activation map in response to identical stimulation used in fMRI experiment shown in A. (C) 3D illustration of the BOLD activation map shown in A. The x and y axes represent the location of the voxel in mm whereas the z axis represents the normalized percentage of signal change between the pre-stimulus and stimulus periods. (D) 3D illustration of the LFP activation map shown in C. (E) FWHM of area 3b, significance at * $p<0.001$ (Wilcoxon signed-rank test). (F) The area values of 3b and 1. (G) FWHM of area 1. (H) The ratio of major and minor axis of 3b and 1. A total of 30 runs from 6 monkeys were acquired for BOLD measurements, and 30 runs from 4 monkeys were acquired for LFP measurements.

For BOLD responses (n = 6 subjects), the FWHM of the major axis (1.08 ± 0.13 mm) of single-digit activation in area 3b was statistically significantly ($P < 0.001$, Wilcoxon signed-rank test) larger than that of the minor axis (0.71 ± 0.21 mm), whereas the FWHM of the major axis (0.95 ± 0.21 mm) in area 1 was not significantly different ($P > 0.05$) from that of the minor axis (0.81 ± 0.09 mm). For stimulus-evoked LFP responses (n = 4 subjects), the FWHM of the major axis (1.07 ± 0.16 mm) was statistically significantly ($P < 0.001$) larger than that of the minor axis (0.78 ± 0.20 mm) in area 3b; again, in area 1, the FWHM of the major axis (0.96 ± 0.12 mm) was not significantly different ($P > 0.05$) from that of the minor axis (0.84 ± 0.16 mm). Activation areas of area 3b (BOLD: 0.61 ± 0.23 mm^2; LFP: 0.69 ± 0.15 mm^2) and area 1 (BOLD: 0.61 ± 0.18 mm^2; LFP: 0.68 ± 0.23 mm^2) did not differ ($P > 0.05$). For both BOLD and LFP signals, Table 1 summarizes these results.

Table 1 FWHM from all subjects for stimulated BOLD and LFP

Modality	area 3b (mm)		area 1 (mm)	
	Major axis**	Minor axis**	Major axis	Minor axis
BOLD	1.08±0.13	0.71±0.21	0.95±0.21	0.81±0.09
LFP	1.07±0.16	0.78±0.20	0.96±0.12	0.84±0.16

** indicates significance ($p<0.001$) between major and minor axes of area 3b of both modalities in stimulations.

Reproducibility and Spatial Agreement Between Activation Locations Measured by BOLD and LFP

We then examined the reproducibility of the activation centers of area 3b and area 1 of stimulus-evoked BOLD and LFP across runs and the spatial relationships between BOLD and LFP activation maps in each individual animal. Within each fMRI session, we determined the center of mass of each activation focus and then calculated the means and SDs of distances between corresponding centers on separate stimulus runs for all runs within each session and looked at the variation across study sessions and subjects (n = 6 animals, 30 runs). The inter-center distance variation for BOLD was 0.23 ± 0.05 mm for area 3b, and 0.24 ± 0.05 mm for area 1. The spatial variation of activation centers was thus close to the size of one voxel (in-plane resolution of 0.274 × 0.274 mm^2). For stimulus-evoked LFP activation maps (n = 4 animals, 30 runs), the inter-center distance was 0.10 ± 0.03 mm for area 3b and 0.12 ± 0.04 mm for area 1, respectively. The inter-center distance was smaller than the spatial spacing (0.4 mm) between two adjacent electrodes. Direct comparisons between BOLD and LFP maps revealed that the inter- center distance variation between modalities was 0.32 ± 0.06 mm for area 3b and 0.35 ± 0.09 mm for area 1. The spatial agreement was close to the range of a single BOLD (0.274 × 0.274 mm^2) and LFP (0.40 × 0.40 mm^2) mapping voxel. Anatomic images of both modalities were coregistered within 0.10 mm accuracy.

Discussion

This study aimed to determine to what extent the local spatial profile of BOLD fMRI signals corresponds to underlying neuronal activity at a submillimeter, cortical modular scale. We compared the spatial extents (FWHMs of major and minor axes, area, and major/minor axis ratio) and activation center locations of BOLD signal changes with those of 'gold standard' electrophysiological LFP measurements during tactile stimulation, in the primary somatosensory cortex of new world monkeys. Using 0.274×0.274 mm^2 in-plane resolution BOLD fMRI at 9.4 T and LFP recordings with 98-channel (two 7×7) microelectrode arrays (0.40×0.40 mm^2 in spacing), we compared BOLD and LFP measures in two cases: stimulus-evoked BOLD versus LFP responses, and areas 3b versus 1. We found that the FWHM of PSFs of BOLD and LFP responses to tactile stimuli were comparable and around 1 mm, which is the size of one single digit representation. Both modalities captured elongated stimulus responses in the lateral to medial direction in area 3b, a feature that was absent in area 1. Moreover, variation in activation centers for repeated measurements by BOLD was less than 0.25 mm and was smaller for LFPs, whereas the separation of activation centers between modalities was very similar, indicating the stability and reproducibility of stimulus activation locations within and across two modalities. Extending previous observations of the closely correlated signal increases of LFP and BOLD signals to stimuli [Logothetis et al., 2001], here we provide further evidence of a close and strong spatial correspondence between BOLD and LFP signals in response to stimulation. The strong agreement between BOLD and LFP in stimulation indicates that local extents of activation are constrained by neuronal properties, and not other factors. BOLD fMRI at high field and at submillimeter resolution directly and faithfully reflects the spatial distribution of underlying neural activity.

Implications for High-Resolution BOLD fMRI at High Field

The PSF of BOLD mapping signals sets the theoretical limits of spatial specificity and resolution of functional imaging. The width of the measured BOLD PSF is a convolution of the contributions from the intrinsic spatial distribution of the neural activity involved, the effects of converting neural electrical activity to a spatial distribution of metabolic and hemodynamic changes that affect MRI signals, and the effects of image acquisition and reconstruction with finite resolution. The PSF that we report in S1 cortex is narrower than those reported previously (3.5 mm at 1.5 T [Engel et al., 1997], 3.9 mm at 3 T [Parkes et al., 2005], and 2 mm at 7 T [Shmuel et al., 2007]). We attribute this difference to the effects of magnetic field on the functional mapping signals used and to our use of relatively high-resolution acquisitions. The BOLD response at lower magnetic fields (e.g., 1.5 T) may be dominated by signals from larger draining veins with little contribution from microvasculature. At high fields, the relative contributions of both intravascular signals and the effects of larger vessels on extravascular dephasing to the overall fMRI signal changes are substantially diminished [Yacoub et al., 2001; Ugurbil et al., 2003]. The increase in the intrinsic width of the PSF of BOLD signals at 1.5 T and 3 T may be attributed to the presence of greater large vessel contributions to signal dephasing of the extravascular water at those lower fields [Kennan et al., 1994; Duong et al., 2003]. Moreover, it is likely that measurements acquired at lower field and resolution also reflected the intrinsic resolution limitations of the image acquisitions. The higher resolution that we used made it possible to reduce partial volume effects and more closely approach the intrinsic limits of BOLD. Functional images acquired with an in-plane resolution of 0.547×0.547 mm^2 yielded PSFs significantly wider than those obtained from higher-resolution functional images with an in-plane resolution of 0.274×0.274 mm^2, indicating that partial volume averaging may broaden regions of activation even at this scale, and confirming that higher-resolution functional images increase the spatial specificity of BOLD fMRI so that the intrinsic BOLD PSF need not be a limiting feature in practice. This suggests that the spatial specificity of submillimeter resolution BOLD fMRI at high magnetic field provides a reliable tool for the investigation of cortical micro-organization.

Spatial Extents of Stimulus-Evoked BOLD and LFP Signals in S1 Cortex

In this study, we pushed the fMRI spatial resolution to submillimeter (0.274×0.274 mm^2) and compared it directly with LFP recordings from the same region with a resolution of 0.40×0.40 mm^2. We found that the FWHMs of BOLD activations at 9.4 T were around 1 mm, which is four times the acquired voxel size. We found excellent spatial agreement between stimulus-evoked BOLD and LFP responses in both area 3b and area 1. The close coupling between columnar structures and local microvasculature likely contributed to the high spatial agreement between two modalities [Sheth et al., 2004]. The tactile stimulus we used is subtle and activates only a small (~1 mm) piece of cortex compared with much broader activation previously reported in the visual cortex [Kim et al., 2004]. It is very likely the 8-Hz digit stimuli activate only a fraction of each digit column, as this stimulus drives predominantly slow-adapting neurons [Powell and Mountcastle, 1959; Burton and Sinclair, 1996].

References

Bandettini, P.A., Wong, E.C, Hinks, R.S., Tikofsky, R.S., and Hyde, J.S. (1992) Time course EPI of human brain function during task activation. *Magn. Reson. Med.,* **25**, 390-397.

Burton, H. and Sinclair, R.J. (1996) Somatosensory cortex and tactile perceptions. *Pain and Touch. Academic Press,* **105**, 177.

Buxton, R. B. (2013) The physics of functional magnetic resonance imaging (fMRI). *Reports on Progress in Physics*, **76**, 096601.

Chernov, M. M, Chen, G., Torre-Healy, L. A., Friedman, R. M. and Roe, A. W (2016) Microelectrode array stimulation combined with intrinsic optical imaging: A novel tool for functional brain mapping. *Journal of Neuroscience Methods,* **263**, 7-14.

Duong, T.Q., Yacoub, E., Adriany, G., Hu, X.P., Ugurbil, K. and Kim, S.G. (2003) Microvascular BOLD contribution at 4 and 7 T in the human brain: Gradient-echo and spin-echo fMRI with suppression of blood effects. *Magn. Reson. Med.,* **49**, 1019–1027.

Engel, S.A., Glover, G.H. and Wandell, B.A. (1997) Retinotopic organization in human visual cortex and the spatial precision of functional MRI. *Cerebral Cortex,* **7**, 181–192.

Friedman, R.M., Chen, L.M., and Roe, A.W. (2008) Responses of areas 3b and 1 in anesthetized squirrel monkeys to single and dual site stimulation of the digits. *J. Neurophysiol.,* **100**, 3185–3196.

Glover, G.H., Li, T.Q. and Ress, D. (2000) Image-based method for retrospective correction of physiological motion effects in fMRI: RETROICOR. *Magn. Reson. Med.,* **44**, 162–167.

Kaas, J.H., Nelson, R.J., Sur, M., Dykes, R.W. and Merzenich, M.M. (1984) The somatotopic organization of the ventroposterior thalamus of the squirrel monkey, Saimiri sciureus. *J. Comp. Neurol.,* **226**, 111–140.

Kennan, R.P., Zhong, J. and Gore, J.C. (1994) Intravascular susceptibility contrast mechanisms in tissues. *Magn Reson Med.,* **31**, 9–21.

Kim, D.S., Ronen, I., Olman, C., Kim, S.G., Ugurbil, K. and Toth, L.J. (2004) Spatial relationship between neuronal activity and BOLD functional MRI. *Neuroimage*. **21**, 876-885.

Kwong K. K., Belliveau J. W., Chesler D. A., Goldberg I. E., Weisskoff R. M., Poncelet B. P., Kennedy D. N., Hoppel B. E., Cohen M. S., Turner R., et al. (1992) Dynamic magnetic resonance imaging of human brain activity during primary sensory stimulation. *Proc. Natl. Acad. Sci. USA,* **89**, 5675-5679.

Legatt, A.D., Arezzo, J. and Vaughan. H.G., Jr (1980) Averaged multiple unit activity as an estimate of phasic changes in local neuronal activity: effects of volume-conducted potentials. *Journal of neuroscience methods,* **2,** 203–17.

Leopold, D.A. and Maier, A. (2012) Ongoing physiological processes in the cerebral cortex. *NeuroImage,* **62**, 2190–2200.

Logothetis, N.K. (2003) The underpinnings of the BOLD functional magnetic resonance imaging signal. *J. Neurosci. Off. J. Soc. Neurosci.,* **23**, 3963–3971.

Logothetis, N.K., Pauls, J., Augath, M., Trinath, T. and Oeltermann, A. (2001) Neurophysiological investigation of the basis of the fMRI signal. *Nature,* **412**, 150–157.

Magri, C., Schridde, U., Murayama, Y., Panzeri, S. and Logothetis, N.K. (2012) The amplitude and timing of the BOLD signal reflects the relationship between local field potential power at different frequencies. *J. Neurosci. Off. J. Soc. Neurosci.,* **32**, 1395–1407.

Nir, Y., Fisch, L., Mukamel, R., Gelbard-Sagiv, H., Arieli, A., Fried, I. and Malach, R. (2007) Coupling between neuronal firing rate, gamma LFP, and BOLD fMRI is related to inter-neuronal correlations. *Curr. Biol.,* **17**, 1275–1285.

Ogawa, S., Lee, T.M., Kay, A.R. and Tank, D.W. (1990) Brain magnetic resonance imaging with contrast dependent on blood oxygenation. *Proc Natl Acad Sci USA*, **87**, 9868-9872.

Parkes, L.M., Schwarzbach, J.V., Bouts, A.A., Deckers, R.H.R., Pullens, P., Kerskens, C.M. and Norris, D.G. (2005) "Quantifying the spatial resolution of the gradient echo and spin echo BOLD response at 3 Tesla." *Magn. Reson. Med.,* **54**, 1465–1472.

Powell, T.P. and Mountcastle, V.B. (1959) Some aspects of the functional organization of the cortex of the postcentral gyrus of the monkey: a correlation of findings obtained in a single unit analysis with cytoarchitecture. *Bull Johns Hopkins Hosp*., **105**, 133–162.

Schölvinck, M.L., Leopold, D.A., Brookes, M.J. and Khader, P.H (2013) The contribution of electrophysiology to functional connectivity mapping. *NeuroImage,* **80**, 297–306.

Sheth, S.A., Nemoto, M., Guiou, M., Walker, M., Pouratian, N., Hageman, N. and Toga, A.W. (2004) Columnar specificity of microvascular oxygenation and volume responses: implications for functional brain mapping. *J. Neurosci*., **24**, 634 – 641.

Shi, Z., Rogers, B.P., Chen, L.M., Morgan, V.L., Mishra, A., Wilkes, D.M. and Gore, J.C. (2016) Realistic models of apparent dynamic changes in resting-state connectivity in somatosensory cortex. *Hum Brain Mapp.,* **37**, 3897–910.

Shi, Z., Wu, R., Yang, P.F., Wang, F., Wu, T.L., Mishra, A., Chen, L.M. and Gore, J.C. (2017) High spatial correspondence at a columnar level between activation and resting state fMRI signals and local field potentials. *Proc Natl Acad Sci USA,* **114**, 5253-5258.

Shmuel, A. and Leopold, D.A. (2008) Neuronal correlates of spontaneous fluctuations in fMRI signals in monkey visual cortex: Implications for functional connectivity at rest. *Hum Brain Mapp*., **29**, 751–761.

Shmuel, A., Yacoub, E., Chaimow, D., Logothetis, N.K. and Ugurbil, K. (2007) Spatio-temporal point-spread function of fMRI signal in human gray matter at 7 Tesla. *Neuroimage,* **35**, 539–552.

Snyder, A.Z. (1992) Steady-state vibration evoked potentials: descriptions of technique and characterization of responses. *Electroencephalogr. Clin. Neurophysiol*., **84**, 257–268.

Ugurbil, K., Toth, L. and Kim, D.S. (2003) How accurate is magnetic resonance imaging of brain function? *Trends in Neurosciences,* **26**, 108–114.

Yacoub, E., Shmuel, A., Pfeuffer, J., Van De Moortele, P. F., Adriany, G., Andersen, P., Vaughan, J. T., Merkle, H., Ugurbil, K. and Hu, X. (2001) Imaging brain function in human at 7 Tesla. *Magn Reson Med*., **45**, 588-94.

CHAPTER III

SPATIAL EXTENTS OF BOLD AND LFP IN RESTING STATES

Abstract

Although BOLD fMRI has been widely used to delineate functional circuits at rest, the extent to which BOLD signals correlate spatially with underlying neuronal activity, the spatial relationships between local correlations of BOLD signals in a resting state, and whether these spatial relationships vary across functionally distinct cortical areas are not known. To address these critical questions, we directly compared the spatial extents of the local profiles of intervoxel resting state correlations for both high-resolution BOLD at 9.4 T and LFPs, using 98-channel microelectrode arrays, in functionally distinct primary somatosensory areas 3b and 1 in nonhuman primates. Anatomic images of LFP and BOLD were coregistered within 0.10 mm accuracy. We found that the PSFs of spontaneous BOLD and LFP fluctuations were comparable in resting states, and both estimates of activations were slightly more spatially constrained than local correlations at rest. Importantly, the spread of BOLD correlations at high field are no greater than the extent of LFP signals. These results demonstrate that high-field fMRI has the ability to delineate brain functional organizations at the columnar level, and the intrinsic resolution of BOLD is not a limiting feature in practice and approaches the intrinsic precision achievable by multielectrode electrophysiology.

Introduction

The discovery and analysis of synchronized fluctuations of low-frequency MRI signals between different brain regions at rest have provided a powerful approach to probe functional connectivity between regions and to delineate functional circuits [Biswal et al., 1995; Lowe et al., 1998; Greicius et al., 2003]. Several previous studies have focused on understanding what types of electrophysiological signals [e.g., spike vs. LFP] drive (or correlate) with fMRI signals and have confirmed that fMRI signals are reliable indicators of associated neuronal activity [Logothetis et al., 2001]. Few studies, however, have examined the relationships between fluctuations of fMRI signals and spontaneous electrophysiological signal variations at rest [Scholvinck et al., 2010; Magri et al., 2012]. No study, to our knowledge, has directly compared the spatial distributions of BOLD and LFP signals in their correlation profiles in a resting state. The ultimate spatial resolution and functional specificity of connectivity metrics depend on the local spread of BOLD signals beyond those of underlying neural activity, especially at the mesoscopic level of functional specialization. Here we report the use of high-resolution fMRI at high field strength (9.4 T) to measure the spatial profiles of single-voxel local correlations in a resting state, in the primary somatosensory cortex of nonhuman primates. We then compare these with the LFP inter-electrode correlations, in the same conditions and the same brain region. Our results shed light on the intrinsic limits of BOLD fMRI at high field and the relationship of BOLD signal changes to underlying electrophysiological activity.

In the experiments described, we directly compared the resting state correlation profiles for high-resolution BOLD at 9.4 T and LFPs, using two 7 × 7 multichannel microelectrode arrays include the digit representation regions of two functionally distinct somatosensory subregions 3b and 1 in individual monkeys. We found that the intervoxel correlation profiles of resting state BOLD and spontaneous LFP signals for individual voxels or electrodes were slightly wider than those produced by stimulation (~ 1 mm). In addition, we found no differences in the widths of the PSFs between LFP and BOLD fMRI at a high resolution at 9.4 T in a resting state condition. BOLD fMRI signals obtained at submillimeter resolution at high field are thus reliable and accurate indicators of underlying neural activity in resting states.

Methods

FMRI Data Acquisition and analysis

MR imaging was performed with a 9.4 T 21 cm bore Varian Inova magnet (Varian Medical Systems, Palo Alto, CA), using a 3-cm surface transmit-receive coil secured over the somatosensory cortex. Scout images obtained using a fast gradient-echo sequence were used to define a volume covering the primary somatosensory cortex in which static magnetic field homogeneity was optimized, and to plan oblique slices for structural and functional EPI imaging. T_2^*-weighted gradient-echo structural images [repetition time (TR) = 200 ms, echo time (TE) = 16 ms, four slices, FOV = 35 × 35 mm^2, 512 × 512 matrix, spatial resolution = 0.068 × 0.068 × 2 mm^3, number of excitations = 6] were acquired to identify venous structures on the cortical surface to help locate S1 cortex, and as structural features for co-registration of fMRI images. Within each imaging session, multiple runs (up to 4) of resting state fMRI data were acquired with identical image acquisition sequences (gradient echo-planar image, GE-EPI), parameters (TR = 750 ms, TE = 16 ms) and slice placement. All images were obtained at two different imaging resolutions: 0.547 × 0.547 × 2 mm^3 (low resolution, number of excitations = 2) and 0.274 × 0.274 × 2 mm^3 (high resolution, number of excitations = 4). For resting-state fMRI runs, 300 continuous image volumes were acquired for both resolutions. MR Images were reconstructed on the MR console (Varian VnmrJ) and exported to Matlab (Mathworks, Natick, MA) for analysis.

Standard preprocessing steps were applied to the raw fMRI signals. Slice timing correction was performed following slice-by-slice motion correction. Six translation and rotation parameters were used to regress out temporal variations caused by motion. Time courses were drift corrected using a linear model fitted to each time course. The RETROICOR method was used to correct for physiological noise using the respiration pattern recorded during the scan. No spatial smoothing was applied. Resting state BOLD signal time series were further filtered with a lowpass filter (0.01-0.1 Hz). The top image slice where areas 3b and 1 reside, was analyzed.

Local field potentials recording and analysis

Guided by MRI maps and blood vasculature patterns, two 7 × 7 multichannel Utah electrode arrays (98 channels in total, spacing between each electrode, 400 μm) were carefully inserted into area 3b and area 1 cortex. LFP signals were sampled at 500 Hz and then band-pass filtered between 1 and 150 Hz for quantification. For LFP resting state coherence analysis, magnitude squared coherence was calculated between each selected seed electrode and the other electrodes [Leopold et al., 2003].

Measurements of the Point spread Function of BOLD fMRI signals in resting states

For resting state fMRI runs, ROI seeds were identified based on the vibrotactile stimulus-evoked activation maps. The voxels with the highest % BOLD signal change were chosen as the seeds for each digit in either areas 3b or 1. Resting state BOLD signal time courses were extracted from the seed voxels and then used as the reference models in subsequent voxel-wise correlation analyses. Correlation coefficients (indicators of resting-state fMRI functional connectivity) were computed for each voxel surrounding the seed, and then local functional connectivity maps were generated for each seed. Identical spatial fitting procedures were applied to derive the FWHM, area and major/minor axis ratio of Gaussian point-spread functions of fitted local correlation profiles [Shi et al., 2017].

Quantification of the Point spread Function of Local Field Potentials in Resting States

For resting-state local field potentials, ROI seeds were identified based on the multi-electrode array stimulus response maps. Electrodes with the largest percentage of signal power change between 20 sec stimuli presentations and 20 sec pre-stimuli periods for single digit stimulations were selected as seeds, from which resting-state LFP electrode-wise functional connectivities were computed for each seed. To evaluate the spatial profiles of resting-state LFP correlations, we first placed one ROI seed (either area 3b or area 1) and computed its functional connectivity map based on functional coherence between this seed and the rest of the electrodes. We then used the same approach as described above to compute the point-spread functions of resting-state LFP correlations of this area within S1 cortex.

Results

Comparable local voxel-voxel correlation profiles of resting state BOLD and LFP signals

We measured the FWHM, area and major/minor axis ratio of intervoxel correlation profiles of resting state BOLD signals for foci of stimulus-evoked activations, and compared these with corresponding resting state LFP signals. We selected single voxels that showed the strongest responses to tactile stimuli as seeds in areas 3b and 1 (Figure 11). Within a single digit representation in areas 3b and 1, the local intrinsic functional connectivity profiles of resting state BOLD and LFP signals are very similar. FWHMs of the major and minor axes of the resting-state intervoxel BOLD correlation profiles were respectively 1.16±0.15 mm and 0.83±0.14 mm in area 3b and 1.07±0.17 mm and 0.90±0.08 mm in area 1. For resting state LFP signals, FWHMs of the major and minor axes of the resting-state intervoxel LFP correlation profiles were 1.19± 0.16 mm and 0.84±0.12 mm in area 3b and 1.12±0.12 mm and 0.98±0.13 mm in area 1. These LFP measures were not significantly different from resting state BOLD estimates.

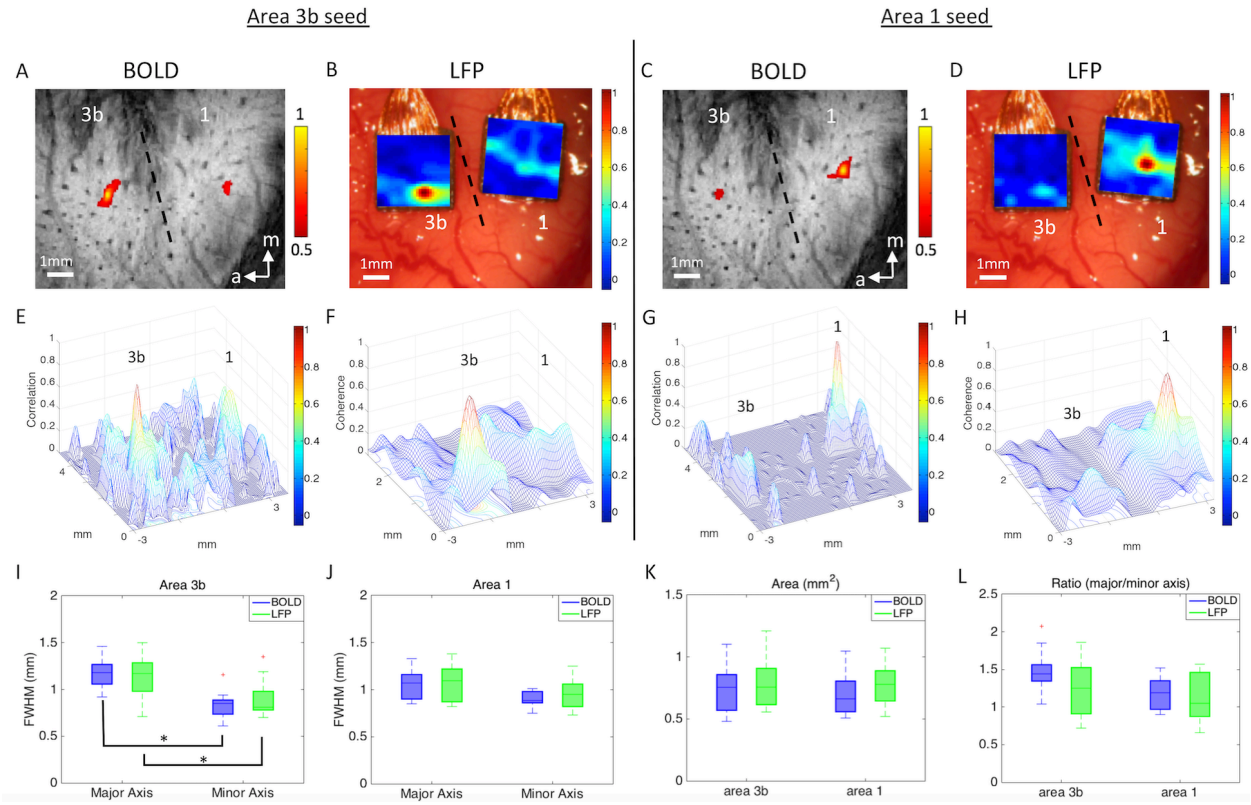

Figure 11 Spatial extent of resting-state fMRI connectivity within areas 3b and 1. One case is shown in A-H, and the entire population data are given in I-L. (A) BOLD correlation map in the resting-state condition. Seed voxel was placed in the digit region in area 3b for voxel-wise correlation analysis. Correlation map was thresholded at r>0.5, with a peak of 1. Dotted line represents estimated inter-areal border between areas 3b and 1. (B) Corresponding LFP correlation map of seed area 3b in the resting-state condition. (C) BOLD correlation map of seed area 1. (D) Corresponding LFP correlation map of seed area 1. (E-H) 3D plots of correlation spatial profiles of BOLD and LFP in areas 3b and 1 with x and y axes representing the location of the voxel (mm) and z axis representing the correlation values. (I) FWHM of area 3b in the resting state condition, significance at * $p<0.001$. (J) FWHM of area 1. (K) The area values of 3b and 1 in the resting-state condition. (L) The major and minor axis ratio of 3b and 1 at rest. A total of 18 runs from 6 animals were acquired for BOLD measurements, and 22 runs from 4 monkeys were acquired for LFP measurements.

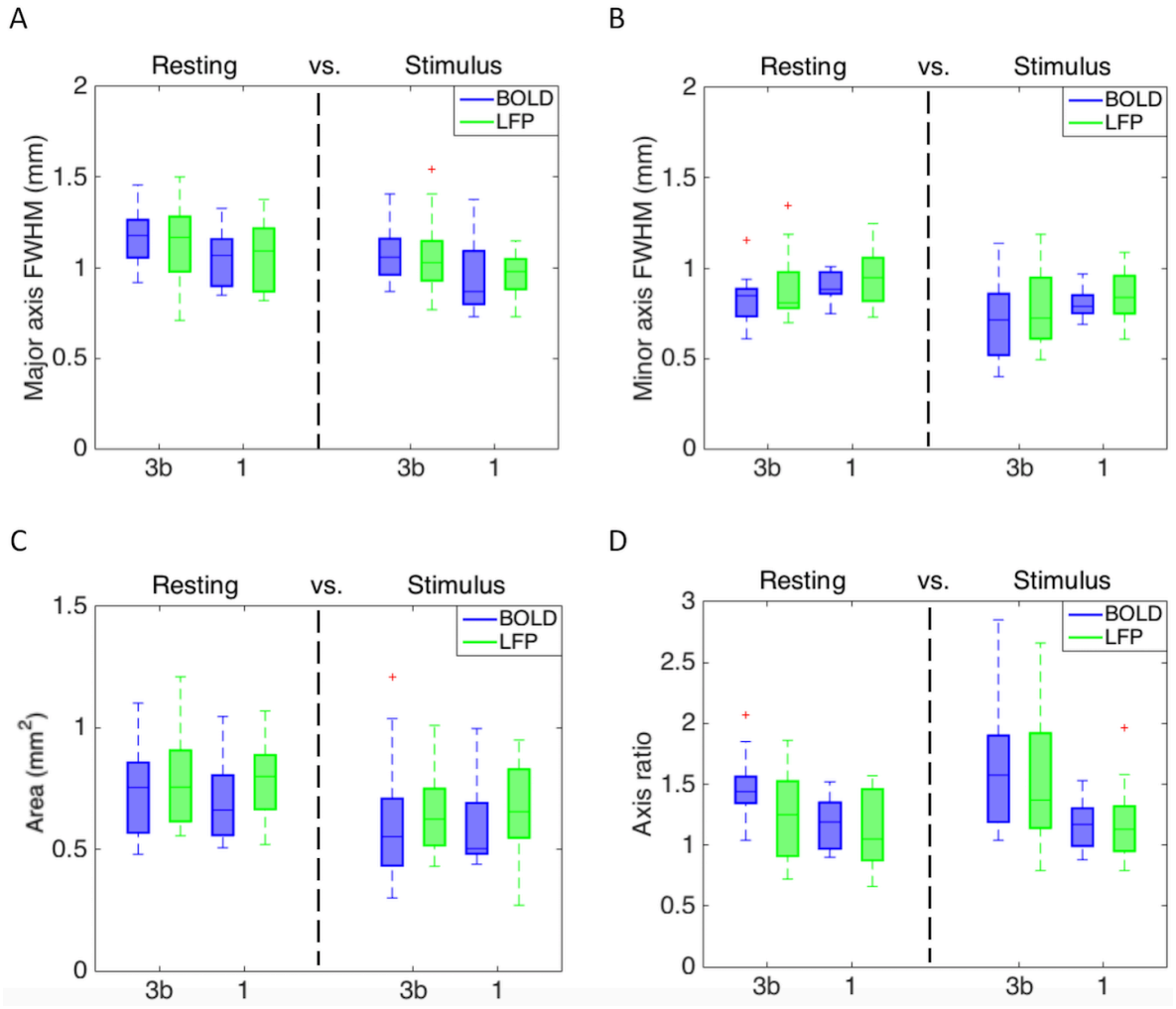

Figure 12 Comparison of point-spread functions of BOLD and LFP signals in areas 3b and 1, between resting-state and stimulation. (A) FWHM of major axis for areas 3b and 1. (B) FWHM of minor axis for both areas. (C) The area values of 3b and 1 in both resting and stimulus conditions. (D) The major and minor axis ratio of 3b and 1 in both conditions.

Local spatial extents of resting state functional connectivity are wider than those of cortical responses to stimuli for BOLD and LFP signals

Direct comparisons of the FWHM measures between stimulation and resting states revealed that the PSF of resting state voxel-voxel correlations is significantly wider than that of stimulation responses (p <0.05, Figure 12), regardless of specific area examined (area 3b or area 1). For example, in both areas 3b and 1, the FWHM of the major axis (1.16±0.15 mm and 1.07±0.17 mm) and that of the minor axis (0.83±0.14 mm and 0.90±0.08 mm) of the resting-state BOLD correlations were larger than both the major axis (1.08±0.13 mm and 0.95±0.21 mm) and minor (0.71±0.21 mm and 0.81±0.09 mm) axes in the stimulated BOLD activation maps. Moreover, in both areas 3b and 1, the FWHM of the major axis (1.19±0.16 mm and 1.12±0.12 mm) and that of the minor axis (0.84±0.12 mm and 0.98±0.13 mm) of the resting-state LFP electrode-electrode coherence were larger than both the major axis (1.09±0.14 mm and 1.01±0.23 mm) and minor (0.65±0.14 mm and 0.83±0.20 mm) axes in the stimulated LFP activation maps. For both BOLD and LFP signals, Table 2 summarizes these results.

Table 2 FWHM from all subjects for stimulated and resting-state BOLD and LFP

Modality	Stimulated *				Resting-state *			
	area 3b (mm)		area 1 (mm)		area 3b (mm)		area 1 (mm)	
	Major axis	Minor axis	Major axis	Minor axis	Major axis	Minor axis	Major axis	Minor axis
BOLD	1.08±0.13	0.71±0.21	0.95±0.21	0.81±0.09	1.16±0.15	0.83±0.14	1.07±0.17	0.90±0.08
LFP	1.07±0.16	0.78±0.20	0.96±0.12	0.84±0.16	1.14±0.20	0.89±0.17	1.11±0.19	0.97±0.16

* indicates significance (p<0.05) between resting-state and stimulated conditions

Discussion

This study aimed to determine to what extent the local correlation profile of BOLD fMRI signals corresponds with underlying neuronal activity in resting states. Using 0.274×0.274 mm^2 in-plane resolution BOLD fMRI at 9.4 T and LFP recordings with 98-channel (two 7×7) microelectrode arrays (0.40×0.40 mm^2 in spacing), we compared BOLD and LFP measures in three cases: (1) resting state BOLD versus spontaneous LFP signal changes; (2) stimulus-evoked versus resting-state maps in each modality; and (3) areas 3b versus 1. We found that resting state BOLD fMRI and LFP signals exhibited very similar intervoxel spatial correlation profiles within single-digit representation columns in the primary somatosensory cortices of areas 3b and 1. In addition, the PSFs of intervoxel local correlation profiles of both resting state BOLD and LFP signals were slightly, but significantly wider (p <0.05), than those of stimulus activations. The elongated spatial profiles of digit representations in area 3b were present in resting state correlations. BOLD fMRI at high field and at submillimeter resolution directly and faithfully reflects the spatial distribution of underlying neural activity.

Spatial Extents of BOLD and LFP Signals in S1 Cortex in resting states

Despite their widespread adoption as measures of functional connectivity, little is known as to how the low-frequency temporal fluctuations of resting state BOLD signals vary locally, and whether correlated fluctuations actually reflect synchronized spontaneous LFP signal variations at rest. Our previous studies in monkeys demonstrated that the strength of resting state BOLD signal correlations between brain regions was related closely to the strength of anatomic connections and whether those areas coactivated to the same stimuli [Wang et al., 2003; Reed et al., 2008]. These observations suggest that neurons that share similar functions and anatomically dense connections exhibit highly synchronized signal fluctuations at rest. A residual question is whether the extent of the activity of functionally homogeneous neurons is accurately reflected by resting state fMRI correlations. In this study, we assessed the spatial relationship between resting state BOLD and LFP measurements and between stimulus response and local correlation profiles in a well-described cortical modular structure, the single-digit representations in areas 3b and 1 in monkeys. Our data demonstrate that the spatial extents of high correlations of both BOLD and LFP signals are constrained tightly to the anatomic boundaries of neurons receiving inputs from the

same digit region-tips in a similar manner. The different PSF shapes identified in area 3b versus area 1 (elongated vs. round) further support the correspondence between neural electrical signals and BOLD signal fluctuation at rest at the submillimeter to millimeter scale. The high degree of agreement between PSFs of BOLD and LFP signals in resting states supports the notion that synchrony within a functionally homogeneous population of neurons determines the strength of local resting state correlation measures in either modality.

If the spontaneous fluctuations in the resting state are driven by common inputs (e.g., from thalamus or cortical-cortical connections [Reed et al., 2008]), then the wider FWHMs for correlation profiles could reflect that more neurons were engaged by these common inputs. What these inputs are and to what extent the differences in common input are reflected in the resting state functional connectivity signals are of great interest for further investigation. Together with our recent findings of the close relationship between interregional BOLD and LFP correlations, the tight local spatial relationship between BOLD and LFP signals shows that resting state BOLD signals are reflective of underlying neuronal electrical activity, and therefore, can be used to probe functional connectivity.

References

Biswal, B., Yetkin, F.Z., Haughton, V.M. and Hyde, J.S. (1995) Functional connectivity in the motor cortex of resting human brain using echo-planar MRI. *Magn Reson Med,* **34**, 537–541.

Greicius, M.D., Krasnow, B., Reiss, A.L. and Menon, V. (2003) Functional connectivity in the resting brain: A network analysis of the default mode hypothesis. *Proc Natl Acad Sci USA,* **100**, 253–258.

Leopold, D.A., Murayama, Y. and Logothetis, N.K. (2003) Very slow activity fluctuations in monkey visual cortex: implications for functional brain imaging. *Cereb. Cortex,* **13**, 423–433.

Logothetis, N.K., Pauls, J., Augath, M., Trinath, T. and Oeltermann, A. (2001) Neurophysiological investigation of the basis of the fMRI signal. *Nature,* **412**, 150–157.

Lowe, M.J., Mock, B.J. and Sorenson, J.A. (1998) Functional connectivity in single and multislice echoplanar imaging using resting-state fluctuations. *Neuroimage,* **7**, 119–132.

Magri, C., Schridde, U., Murayama, Y., Panzeri, S. and Logothetis, N.K. (2012) The amplitude and timing of the BOLD signal reflects the relationship between local field potential power at different frequencies. *J. Neurosci. Off. J. Soc. Neurosci.,* **32**, 1395–1407.

Reed, J.L., Pouget, P., Qi, H.X., Zhou, Z., Bernard, M.R., Burish, M.J., Haitas, J., Bonds, A.B., and Kaas, J.H. (2008) Widespread spatial integration in primary somatosensory cortex. *Proc. Natl. Acad. Sci. USA,* **105**, 10233–10237.

Schölvinck, M.L., Leopold, D.A., Brookes, M.J. and Khader, P.H (2013) The contribution of electrophysiology to functional connectivity mapping. *NeuroImage,* **80**, 297–306.

Schölvinck, M.L., Maier, A., Ye, F.Q., Duyn, J.H. and Leopold, D.A. (2010) Neural basis of global resting-state fMRI activity. *Proc Natl Acad Sci USA,* **107**, 10238–10243.

Shi, Z., Wu, R., Yang, P.F., Wang, F., Wu, T.L., Mishra, A., Chen, L.M. and Gore, J.C. (2017) High spatial correspondence at a columnar level between activation and resting state fMRI signals and local field potentials. *Proc Natl Acad Sci USA,* **114**, 5253-5258.

Wang, Z., L. M. Chen, L. Negyessy, R. M. Friedman, A. Mishra, J. C. Gore and A. W. Roe (2013) The relationship of anatomical and functional connectivity to resting-state connectivity in primate somatosensory cortex. *Neuron,* **78,** 1116-1126.

CHAPTER IV

DYNAMIC CHANGES IN RESTING STATE FUNCTIONAL CONNECTIVITY

Abstract

Variations over time in resting-state correlations in blood oxygenation level-dependent (BOLD) signals from different cortical areas may indicate changes in brain functional connectivity. However, apparent variations over time may also arise from stationary signals when the sample duration is finite. Recently, a vector autoregressive (VAR) null model has been proposed to simulate real functional magnetic resonance imaging (fMRI) data, which provides a robust stationary model for identifying possible temporal dynamic changes in functional connectivity. In this work, we propose a simpler model that uses a filtered stationary dataset. The filtered stationary model generates statistically stationary time series from random data with a single prescribed correlation coefficient that is calculated as the average over the entire time series. In addition, we propose a dynamic model, which is better able to replicate real fMRI connectivity, estimated from monkey brain studies, than the two stationary models. We compare simulated results using these three models with the behavior of primary somatosensory cortex (S1) networks in anesthetized squirrel monkeys at high field (9.4 T), using a sliding window correlation analysis. We found that at short window sizes, both stationary models reproduced the distribution of correlations of real signals well, but at longer window sizes, a dynamic model reproduced the distribution of correlations of real signals better than the stationary models. While stationary models replicate several features of real data, a close representation of the behavior of resting-state data acquired from somatosensory cortex of non-human primates is obtained only when a dynamic correlation is introduced, suggesting dynamic variations in connectivity are real.

Introduction

Low frequency fluctuations in blood oxygenation level-dependent (BOLD) functional magnetic resonance imaging (fMRI) signals may occur spontaneously in functionally related areas of the cortex in the absence of any specific task. Biswal et al. [1995] first reported the correlation in fMRI signal fluctuations between the left and right motor cortices when the brain was in a resting state. Functionally related brain regions can be identified using their synchronous slow fluctuations in signal intensity [Cordes et al., 2000]. Subsequent studies have identified several consistent resting-state networks, including motor, auditory, visual, attention, and default mode [Damoiseaux et al., 2006].

Various techniques have been used to derive functional connectivity to reveal functionally related brain regions. For example, seed-based region-of-interest (ROI) analyses [Biswal et al., 1995], spatial independent component analysis [McKeown et al., 1998], clustering [Mezer et al., 2009], phase relationships [Sun et al., 2005], and graph theory [Achard et al., 2006; Dosenbach et al., 2007]. Most fMRI studies in the past have assumed that the correlations between brain regions are constant throughout the time series of the entire scan in resting-state experiments [Fransson, 2005]. More recently, there has been an increasing interest in the detection and characterization of possible dynamic changes in functional connectivity [Allen et al., 2014; Chang and Glover, 2010; Hutchison et al., 2013]. Variations in the degree of coupling between different networks would seem to be a plausible feature of neural systems, and the nature of temporal changes in such couplings could be an important aspect of brain function. However, whether observed dynamic changes in correlations between distinct brain regions over time show significantly greater variability than would be expected if the underlying correlation coefficient between the two signals were stationary (time-invariant) is a crucial issue. Currently, there is no consensus on which analysis technique is the most effective at characterizing such temporal variations in resting-state fMRI signals. The most commonly used strategy for analyzing dynamic changes in resting-state functional connectivity has been a sliding window correlation approach [Handwerker et al., 2012; Jones et al., 2012], which is intended to identify pairwise variations in inter-regional time courses. The limitations of this approach are clear and further discussed below. Other methods, for example, the PsychoPhysiological Interactions [PPI; Friston et al., 1997] method studies the dynamical feature of functional connectivity under the assumption that the timing of the various contexts or state changes is known. However, it is often difficult to identify or specify the timing and duration

of the psychological processes being studied a priori. Cribben et al. introduced a Dynamic Connectivity Regression technique, which is a data-driven method for detecting functional connectivity change points between brain regions where the number of change points and their locations are unknown in advance [Cribben et al., 2012]. While this strategy avoids the assumption of knowing state changes in advance, it does not estimate details of the dynamic correlation between the brain regions. Various efforts have also been made to replicate real resting-state fMRI data using simulated time series, most notably the vector autoregressive (VAR) null model [Chang and Glover, 2010; Cribben et al., 2013; Shah et al., 2012; Zalesky et al., 2014] which avoids possible confounds from physiological noise or other sources of artifact.

The purpose of this study was to evaluate whether correlations in real fMRI data are stationary, and to investigate the existence of dynamic correlations. Our motivation was to simulate the behavior of the temporal correlations between different sub-regions in S1 cortex of monkey brain over an 18-min resting-state scanning session. We first used a VAR null model and then developed a simpler model that uses a filtered stationary simulation dataset, whose behavior could then be compared to real resting- state fMRI data. The filtered stationary model generates statistically stationary time series from random data with a single prescribed correlation coefficient that is calculated as the average over the entire time series. We then further modified the model to account for the dynamic features in connectivity, and used a variant of the Kolmogorov-Smirnov (K-S) statistic to quantitatively compare all simulated results to the behavior of real networks. We used a very well characterized network for dynamic functional connectivity studies. Our experimental data were obtained from small regions in the somatosensory (S1) networks in anesthetized squirrel monkeys at high field strength (9.4 T). The hand-face region within the S1 cortex of the squirrel monkey has been previously well mapped with functional imaging, electrophysiological and anatomical methods, and the orderly topographic map of the hand region is characterized by a lateral to medial representation of individual digits in three sub-regions of areas 3a, 3b, and 1.

Methods

Animal Preparation

Three squirrel monkeys (three sessions each) were pre-anesthetized with ketamine hydrochloride (10 mg/kg)/ atropine (0.05 mg/kg) and then anesthetized with 0.5-1.5% of isoflurane to maintain a stable physiological condition for MRI scans. Although the actual level may vary across animals, we typically maintained anesthesia under a light stable level around 0.7-0.8% during our functional data acquisition. The anesthetized animals were intubated and artificially ventilated. After intubation, each animal was placed in a custom-designed MR cradle with its head secured using ear bars and an eye bar. Lactated Ringer's solution was infused intravenously (2–3 mL/h/kg) to pre- vent dehydration during the course of the study. Arterial blood oxygen saturation and heart rate (Nonin, Plymouth, MN), electrocardiogram, end-tidal CO_2 (ET-CO_2; 22–26 mm Hg; Surgivet, Waukesha, WI), and respiration (SA Instruments, Stony Brook, NY) were externally monitored and maintained. Temperature (37.5–38.5^{o}C) was monitored (SA Instruments) and maintained via a circulating water blanket (Gaymar Industries, Orchard Park, NY). Real-time monitoring was maintained from the time of induction of anesthesia until full recovery. Detailed procedures have been described in a previous publication [Chen et al., 2007]. All procedures were in compliance with and approved by the Institutional Animal Care and Use Committee of Vanderbilt University.

FMRI Data Acquisition and Preprocessing

MRI imaging was performed on a 9.4 T 21 cm bore Varian Inova magnet (Varian Medical Systems, Palo Alto, CA), using a 3-cm surface transmit–receive coil secured over the sensory cortex. Scout images obtained using a fast gradient-echo sequence were used to define a volume covering primary somatosensory cortex in which static magnetic field homogeneity was optimized, and to plan four oblique slices for structural and functional imaging (Figure 13, only the top slice shown). T_2^*-weighted gradient-echo structural images [repetition time (TR), 200 ms; echo time (TE) = 16 ms, four slices, 512 × 512 matrix; 68 × 68 × 2000 mm^3 resolution; number of excitations = 6] were acquired to identify venous structures on the cortical surface used to help locate S1, and as structural features for coregistration of fMRI images. fMRI data were acquired from the same slice. For each monkey, three runs of 720 continuous functional gradient echo-planar image (EPI)

functional volumes (TE =16 ms; 64 × 64 matrix; 547 × 547 × 2000 mm^3 resolution) were acquired. Acquisition time of each run was 18 min, and the TR was 1.5 s. Images were reconstructed on the MR console (Varian VnmrJ) and imported into Matlab (Mathworks, Natick, MA) for analysis. The raw echo-planar images were spatially smoothed with a 3 × 3-voxel Gaussian window with a standard deviation of 312 mm, and then interpolated to a 256 × 256 matrix for overlay on anatomical images. Time courses were drift corrected using a linear model fitted to each time course and temporally smoothed with a low-pass filter.

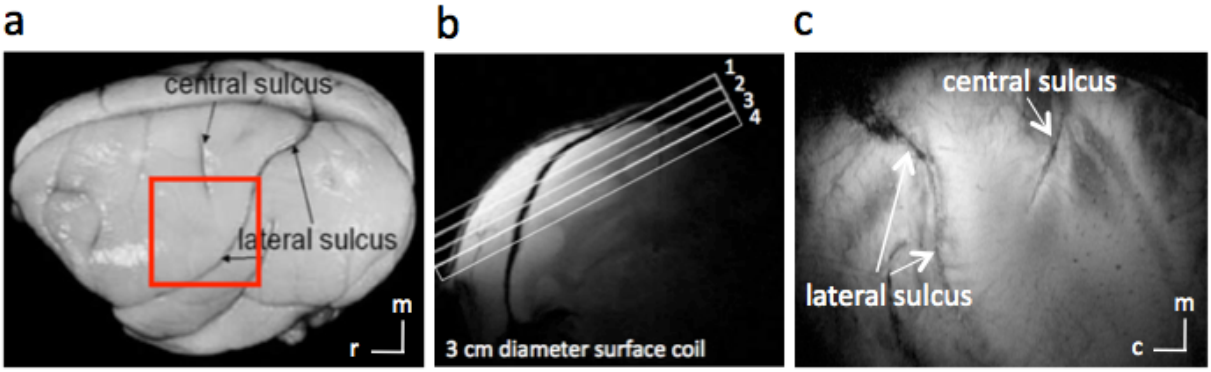

Figure 13 Anatomic images for studying S1. a, Major landmarks (such as central and lateral sulci) used to identify S1 are visible on squirrel monkey brain. The red box indicates the location of ROIs. b, A high-resolution coronal image is collected to locate somatosensory cortices and to guide placement of an oblique slice parallel to the S1 (locations indicated by rectangles, overlaid or coronal scout image). This oblique orientation was used for both high-resolution anatomical and functional imaging. c, In an image acquired with T_2^* weighting, sulci and vascular structures appear dark. Both central and lateral sulci are readily identified in the most superficial slice. c, caudal; m, medial; r, rostra.

Identification of ROI Seeds

Specific ROI seeds were identified according to the vibrotactile stimulus evoked activation maps, which were obtained by separate fMRI runs within the same imaging session. A stimulus-evoked fMRI activation map was used to locate the finger pad regions in areas 3a, 3b, and 1 (see Figure 14). The fingers were secured by gluing small pegs to the fingernails and fixing these pegs firmly in plasticine, leaving the glabrous surfaces available for vibrotactile stimulation by a rounded plastic probe (2 mm diameter) connected to a piezoelectric device (Noliac, Kvistgaard, Denmark). Piezos were driven by Grass S48 square wave stimulators (Grass-Telefactor, West Warwick, RI) at a rate of 8 Hz with 30 ms pulse duration. Stimulation was applied in blocks of 30 s on and then 30 s off. The timing of the presentation of stimuli was externally controlled by the MR scanner. The correlation of each functional EPI time course to a reference waveform was calculated and activation maps were generated by identifying voxels whose correlation with the reference waveform was significant at least at $p < 10^{-4}$ (uncorrected for multiple comparisons). Voxels with the highest p values were chosen as seeds (small blue boxes in Figure 14), from which filtered resting-state fMRI time courses were extracted for the dynamic functional connectivity analysis.

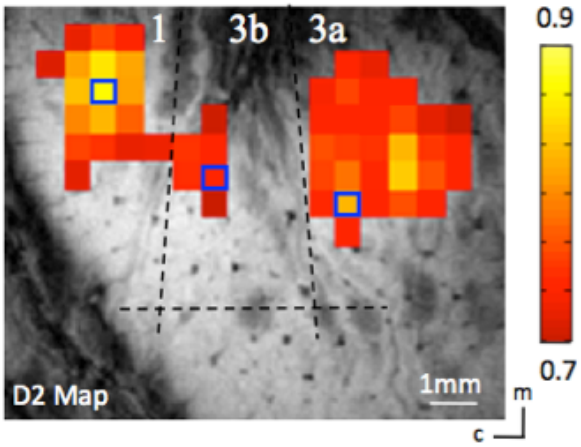

Figure 14 Localization of digit regions with fMRI mapping in the S1 cortex of squirrel monkeys. One case is shown in here. BOLD activation in response to vibrotactile stimulation of the D2 tip. Activated voxels are observed in areas 3a, 3b and 1. Correlation maps were thresholded at r > 0.7, with a peak correlation value of 0.9. Dotted black line indicates approximate inter-area borders. Blue boxes show the seed voxels. Scale bar, 1mm. c, caudal; m, medial.

Vector Autoregressive Null Model

The VAR model used to capture linear interdependencies among multiple time series [Hacker and Hatemi, 2008] is described in the following text [Chang and Glover, 2010]:

Let x and y represent the BOLD signal time series from two different ROIs in S1 cortex. We first fit a (stationary) VAR model to x and y:

$$\begin{cases} x(t) = \sum_{i=1}^{p} a_i^x \; x(t-i) + \sum_{i=1}^{p} b_i^x \; y(t-i) + \varepsilon^x(t) \\ y(t) = \sum_{i=1}^{p} a_i^y \; x(t-i) + \sum_{i=1}^{p} b_i^y \; y(t-i) + \varepsilon^y(t) \end{cases}, \qquad (13)$$

where the optimal model order p (p = 9) is chosen according to the Bayesian information criterion (BIC) score, and t is a time index. Coefficients of the VAR model are estimated using least squares. Next, we generate 1,000 boot-strap time series pairs having the same VAR coefficients (i.e., same stationary relationship) as Eq. (13).

Filtered Stationary (FTS) Null Model

Let x_c represent the common signal in the BOLD signal time series x_1 and x_2 from two different ROIs in S1 cortex. x_c, w_1, and w_2 are stationary Gaussian zero-mean signals, low-pass filtered to contain frequencies only in the BOLD range 0.01-0.1 Hz. Each time course is independent, and contains 720 time points with an effective TR = 1.5 s.

$$\begin{cases} x_1(t) = x_c(t) + b * w_1(t) \\ x_2(t) = x_c(t) + b * w_2(t) \\ corr\big(x_1(t), x_2(t)\big) = r \; (constant) \\ b^2 = \frac{1}{|r|} - 1 \end{cases}, \qquad (14)$$

where the coefficient b is determined by the correlation coefficient between the BOLD signal time series from two different ROIs. Then we generate 1,000 trials based on Eq. (14).

Sliding Window Correlation Analysis

A sliding window correlation analysis is a method for capturing variations in inter-regional synchrony [Hutchison et al., 2013], and is commonly used to investigate dynamic changes in correlations between fMRI time series. In this approach, a time window of fixed length is selected, and data points within that window are used to calculate correlation coefficients between two time series (x and y), which are defined as $r(t) = \text{corr}\,(x^{t+s-1}, y^{t+s-1})$, where s is the window size, x^{t+s-1} and y^{t+s-1} represent the parts of the time series from time t to $t+s-1$, and corr () denotes computation of the Pearson's correlation coefficient. The window is then shifted in time by a fixed number of data points (ranging from a single data point to the length of a window) that defines the amount of overlap between successive windows. The correlations between the time series derived from sub-regions 3a, 3b, and 1 of S1 cortex in monkeys were calculated for window sizes of 30s (20 volumes), 45s (30 volumes), 90s (60 volumes), 135s (90 volumes), 180s (120 volumes), 225s (150 volumes), and 270s (180 volumes). The window was then shifted in time by 1.5s (1 volume) along the entire time series and the correlation coefficient was recalculated. Figure 15 shows an example of the sliding window correlation analysis comparing real fMRI data and two stationary (the VAR and the filtered stationary) null model simulations, with a window size of 60s. This procedure was repeated for all possible window positions within the 720 images of a run. The pairwise sliding window correlations between each of the three sub- regions were calculated for all animals and all scans.

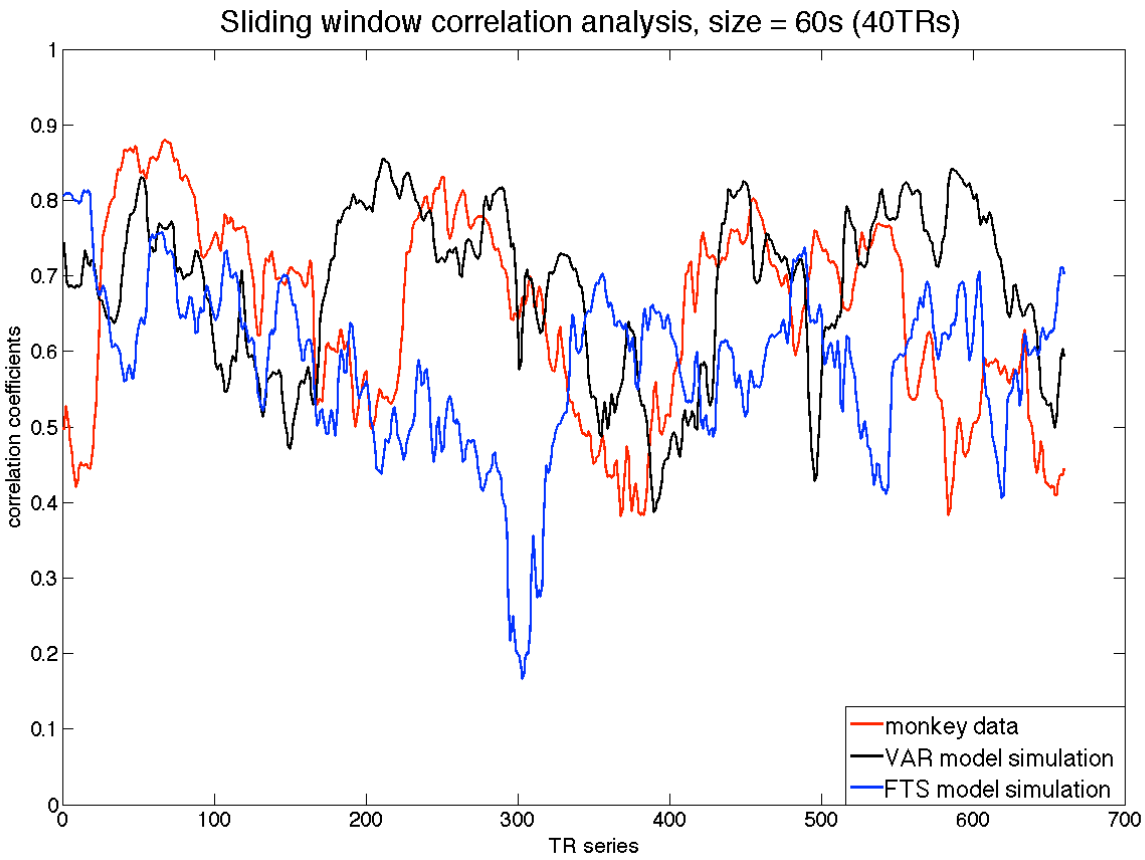

Figure 15 Example of the sliding window correlation analysis comparing real fMRI data and two stationary (the VAR and the filtered stationary) null models, in a window size of 60s (40 TRs).

Underlying Dynamic Null Model

To obtain better approximations than stationary null models of the potential dynamic behavior of real data, we first computed correlation coefficients between two ROIs in monkey brain using a sliding window technique with a window size of 135 sec, and performed a median filtering of the time course of the correlation coefficient. Each time point then contained the median value in the neighborhood of 20 values around the corresponding pixel in the input image. We then fit the smoothed underlying correlations with a sum of 4 sine functions (an example is illustrated in Figure 16). We define this function as an underlying non-stationary correlation function *r(t)* between these two ROIs. Next, we generated 1,000 trials based on Eq. (15). This dynamic simulation can then be compared to the real data.

$$\begin{cases} x_1(t) = x_c(t) + b * w_1(t) \\ x_2(t) = x_c(t) + b * w_2(t) \\ corr\big(x_1(t), x_2(t)\big) = r(t)\ (non-stationary) \\ b(t)^2 = \frac{1}{|r(t)|} - 1 \end{cases}, \tag{15}$$

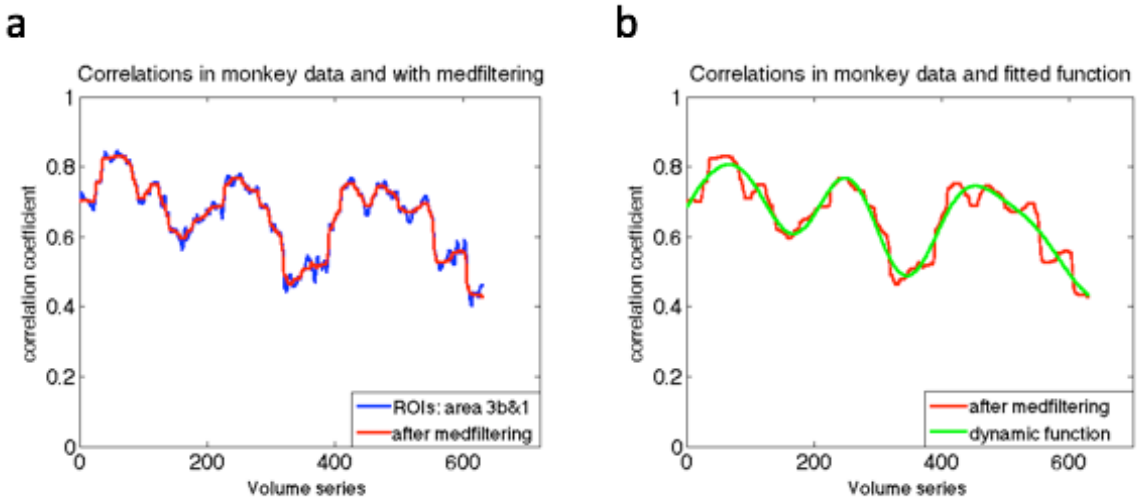

Figure 16 (a) Example of correlations between sub-regions area 3a and 1 in one monkey using sliding window technique in the window size of 135 s, along with a median filtering smoothing. (b) Example of fitted underlying correlation function: a sum of sine, the number of terms is 4.

A Two-Sample Kolmogorov–Smirnov Statistic

Above, we have described the methods to compute the VAR, filtered stationary, and underlying dynamic null model of a given pair of time series. In this section, we quantify the resemblance of the temporal variations in the correlations between the real and simulated data. We perform a sliding window analysis at one window size and construct the empirical cumulative distribution function (ECDF) for each pair of time series. A two-sample Kolmogorov-Smirnov (K-S) statistic [Chakravart, 1967] may be used to evaluate whether two samples come from the same population with a specific distribution, based on measurements of the distance between two ECDFs. It is sensitive to differences in both the location and shape of the ECDFs of the two samples [Marsaglia et al., 2003; Stephens, 1974]. Therefore, lower K-S values between real and simulated data suggest increased accuracy of the model in representing the nature of the real data.

Centering z-Scores

As the sampling distribution of Pearson's *r* is not normally distributed, correlation values were converted to z-scores using Fisher's *z* transform. The K-S results are affected by two main factors, one is the location, and the other is the shape of distribution. To compare distribution shapes, z-scores were centered by subtracting their mean values (Figure 17).

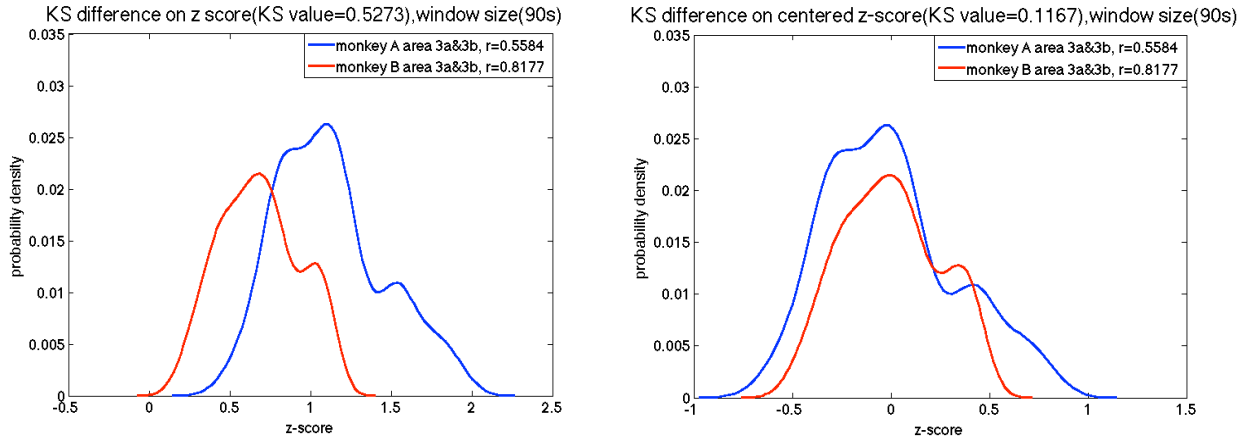

Figure 17 Example of the probability density function of the z-score between sub-regions pair 3a-3b of S1 in two different monkeys before and after centering the z-score.

Illustrative Example of Stationary Models

All sub-region ROI pairs from nine sessions in three monkeys were quantified. Figure 15 and Figure 17 illustrate examples of the results of the sliding window correlation analysis and correlation distributions of actual data and simulated time series, respectively. The correlation coefficient between sub-regions 3b and 1 in S1 cortex of one randomly selected squirrel monkey calculated from the time series of the entire 20-min scan is 0.8144. To simulate fMRI data using the filtered stationary null model, only this correlation coefficient is required. We thus generated two time-series of random signals with correlation coefficient of 0.8144, and used a low-pass filter in the same frequency range as used for BOLD preprocessing (0.01-0.1 Hz). To simulate real data using the VAR null model, we first fit a (stationary) VAR model to the BOLD signal time series from sub-regions 3b and 1 of the same monkey. Then we generated simulated signals using those derived coefficients and performed a sliding window correlation analysis over a range of window sizes (30 s, 45 s, 90 s, 135 s, 180 s, 225 s, 270 s) to both sets of simulated data. The dynamic

behavior of resting-state functional connectivity between sub-regions 3b and 1 of S1 cortex in the monkey was estimated using the same sliding window technique as for the simulated data. Figure 18 shows that the correlation ECDF between sub-regions 3b and 1 in a monkey dataset is similar to the correlation ECDF derived from the filtered stationary null model.

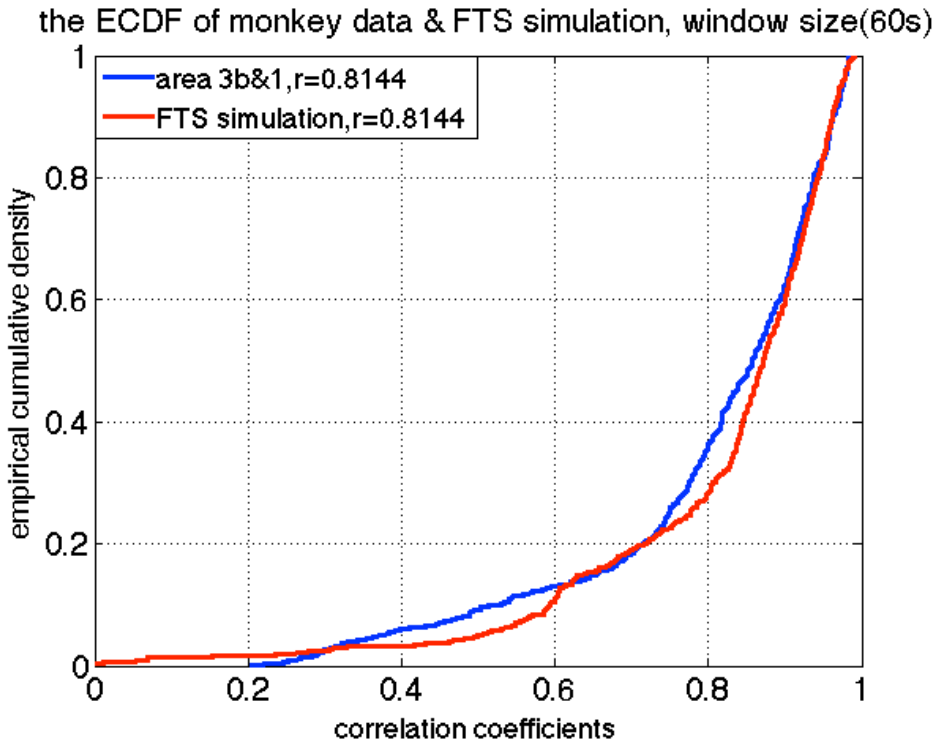

Figure 18 Example of the ECDF of the cross-correlations between two sub-regions of S1 in one monkey, along with the ECDF of the filtered stationary model simulation, KS value = 0.1280.

The Behavior of Connectivity in Different Monkeys

To test whether different monkeys have similar correlation trends in the same ROI pairs, VAR, filtered stationary, and underlying dynamic simulations were conducted on a single random monkey dataset. We then applied a sliding window analysis to both simulated data and the monkeys' real fMRI data over a range of window sizes, and compared the distributions of their z-scores using the two-sample K-S statistic.

Results

Stationary Model Simulations

Pre-processing of resting-state BOLD-fMRI time series usually includes low-pass filtering to remove artifacts and to emphasize frequencies of interest. Such filtering, however, affects the data by introducing autocorrelations in the BOLD time series themselves [Hindriks et al., 2016]. To match the relative strength of this low-pass filtering effect, the filtered stationary null model simulates the low-pass filter performed on the monkey data by matching the BOLD frequency range from 0.01 to 0.1 Hz. We have found this step to be one of the most important for replicating monkey fMRI connectivity in the filtered stationary model (Supporting Information Appendix).

As expected, simulations of stationary random signals show that the variance of correlation coefficients decreases as window size increases [Hutchison et al., 2013]. In addition, the variance decreases for stronger correlation coefficients. The behavior of the correlation coefficients between stationary signals was similar to in vivo monkey data when using smaller window sizes, such as 45 sec. As shown in Figure 19, correlations between functionally related sub-region pairs (e.g., area 3a and area 1 in the same monkey brain) of the monkey data are distributed similarly to the correlations derived from simulated stationary data for short window sizes, but depart substantially for larger window sizes such as 180s (smaller K-S value indicates less difference).

Figure 20 shows the K-S statistic for group of cross-correlations between two functionally related sub-regions of S1 cortex and their corresponding models, and the K-S statistic for cross-correlation between functionally unrelated subregions and the filtered stationary model at the window sizes of 60 s and 180 s. The correlations between functionally related subregion pairs in the monkey data are distributed similarly to the correlations derived from VAR and filtered stationary models at the window size of 60s, but depart substantially at the window size of 180s. However, the correlations between functionally unrelated subregions (two sub-regions from two different monkeys, for example, area 3a from monkey A, and area 3b from monkey B) in the monkey data are distributed similarly to the correlations derived from the filtered stationary model at both window sizes of 60s and 180s.

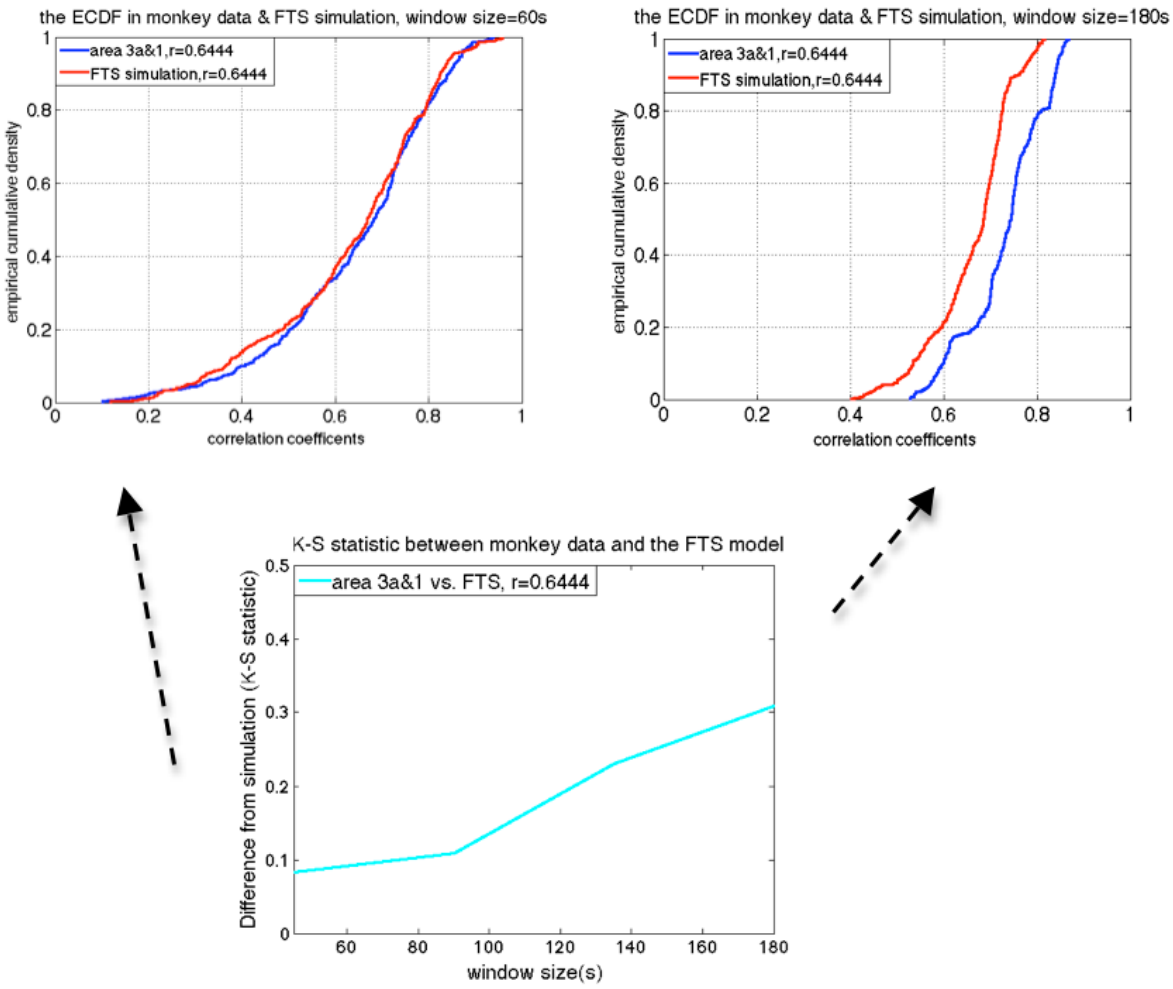

Figure 19 Example of the two-sample K-S statistic on correlations of monkey data and the filtered stationary null model simulation over a range of window sizes.

Additional window sizes can be seen in Figure 21. Figure 21a illustrates the K-S statistic for group of cross-correlations between two functionally related sub-regions area 3a–3b and its corresponding stationary models. The correlations between sub-region pair 3a–3b in the monkey data are distributed more similarly to the correlations derived from the filtered stationary null model than those derived from the VAR model. Specifically, K-S values of correlation coefficients between area 3a-3b of the monkey data and the filtered stationary null model (blue line) are always smaller than those between the same monkey data and the VAR null model (black line). Moreover, these K-S values increase as window sizes increase, which indicates that neither of these two stationary models matches real fMRI data very well at large window sizes. However, the

correlations between functionally unrelated sub-regions are distributed similarly to the stationary data from the filtered stationary null model simulation at all window sizes. Specifically, the red line, which represents K-S values between unrelated sub-regions of monkey data and the filtered stationary null model is always flat over a range of different window sizes.

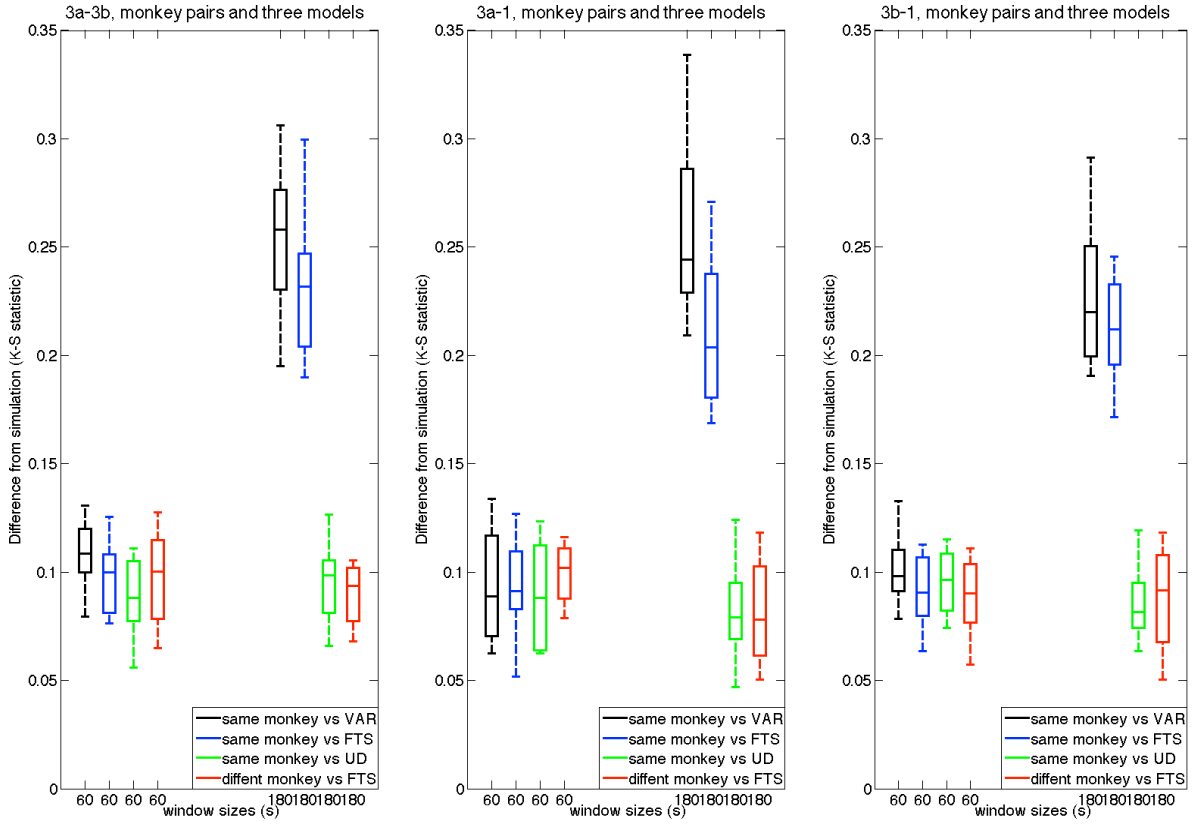

Figure 20 Group analysis on K-S statistic between functionally related monkey data and the VAR, filtered stationary, underlying dynamic models, along with K-S statistic between functionally unrelated monkey data and the filtered stationary model at window sizes 60s and 180s. Sliding window correlations in real data differed from stationary simulations only at the longer window size, as shown by the high K-S statistic (blue, black). Introducing a dynamic component to the simulation eliminated the difference (green), meaning that correlation distributions derived from dynamic simulations matched the real data. Sliding window correlations between two different monkeys' time series (uncorrelated by construction) were reproduced well by the stationary simulations and served as the negative control (red). Error bars indicate standard deviations.

Underlying Dynamic Model Simulation

In the dynamic correlation study, we generated an underlying dynamic null model and applied the same sliding window technique, the Fisher's z-transform and the two-sample K-S statistic. Figure 21b illustrates that correlations between functionally related sub-regions in the monkey data are distributed similarly to the correlations derived from the underlying dynamic null model at all window sizes. Specifically, the green line, which represents K-S values between functionally related ROIs in the monkey data and the underlying dynamic null model is flat over all different window sizes.

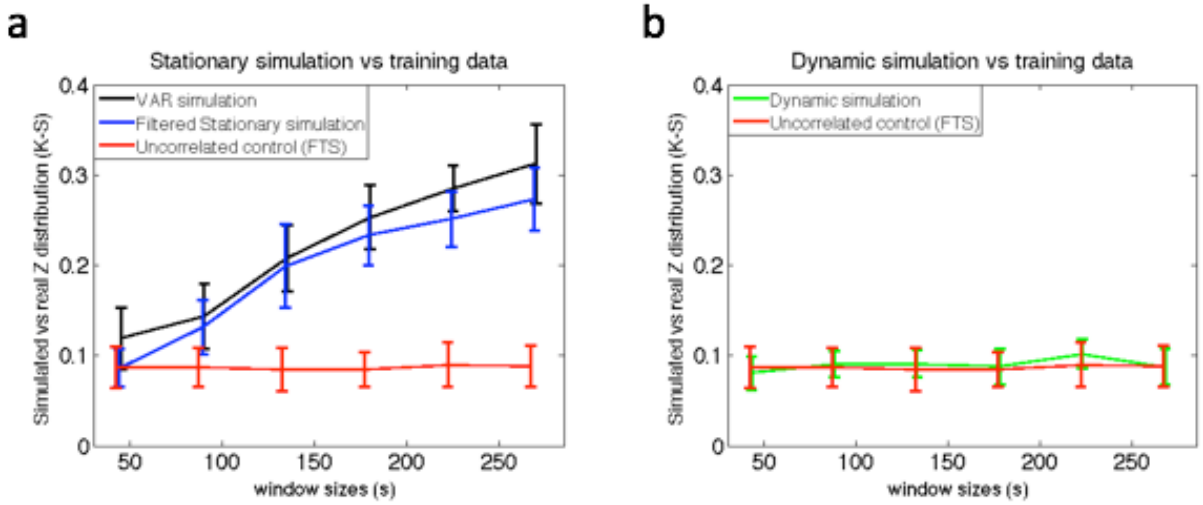

Figure 21 Group analysis on K-S statistic between functionally related monkey sub-region pair area 3a-3b and the stationary and dynamic models, along with K-S statistic between functionally unrelated monkey data and the filtered stationary null model over a range of window sizes. (a) Correlation distributions are indistinguishable from stationary simulations at the shortest window (45 sec) but begin to differ at longer windows (90 sec and up; blue and black). (b) Dynamic simulations reproduce the correlation distributions of real data at all window sizes (green). Error bars indicate standard deviations.

The Behavior of Connectivity in Different Monkeys

Figure 22a, b shows a group analysis of the K-S statistic between sub-region pair area 3a-3b within different monkeys and the stationary and dynamic models before centering the z-score. Figure 22c, d shows a K-S statistic between the same subregion pair in different monkeys and three models after centering the z-score. From Figure 22a-d, it can be seen that the K-S values decreased dramatically after z-score centering. This is because the average correlation coefficients of the nine datasets are different from each other, while their correlation distributions shapes are similar. From Figure 22c, d, it can be seen that the K-S values over different window sizes are as follows: the VAR model (black line) has the largest values, followed by the filtered stationary model (blue line), followed by the dynamic model (green line), and followed by the functionally unrelated monkey data simulation (red line). The two stationary models do not capture the similar correlation features across monkeys as closely as the dynamic model. However, the underlying dynamic model is good at simulating the trend of correlation functions across all three monkeys (9 sessions).

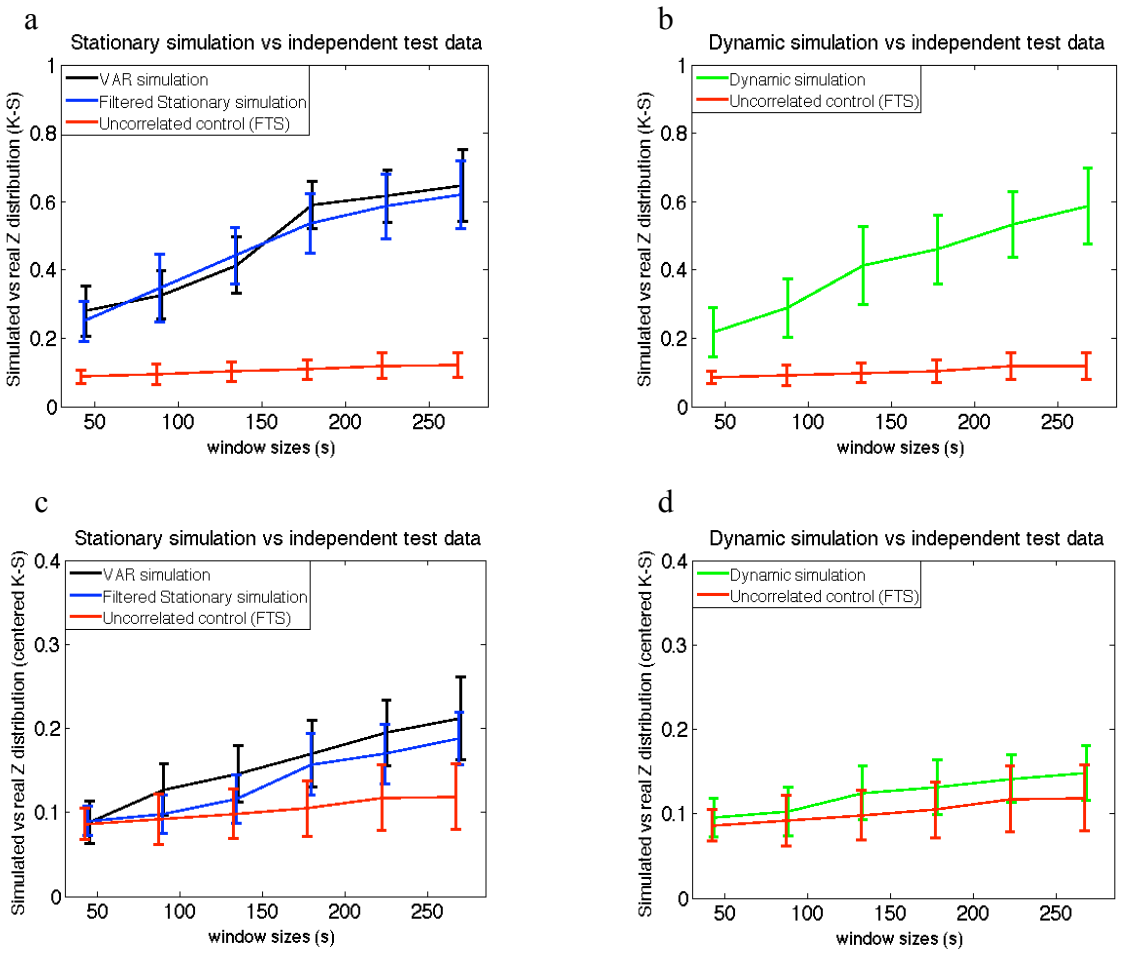

Figure 22 Group analysis on K-S statistic between sub-region pair area 3a-3b within different monkeys and the stationary and dynamic models before (a, b) and after (c, d) centering the z-score. Error bars indicate standard deviations.

To verify whether dynamic correlation similarities existed within identical subregion pairs of monkey data, we plotted the four major frequency components derived from the underlying dynamic model. These components were chosen based on the underlying correlations, which were fit using a sum of four sine functions. From Figure 23, it can be seen that different monkey datasets have similar dynamic correlation frequency components within identical subregion pairs. For these three subregion pairs, it was observed that variation frequency components between 0 and 0.003 Hz had significant contributions to the correlation coefficients.

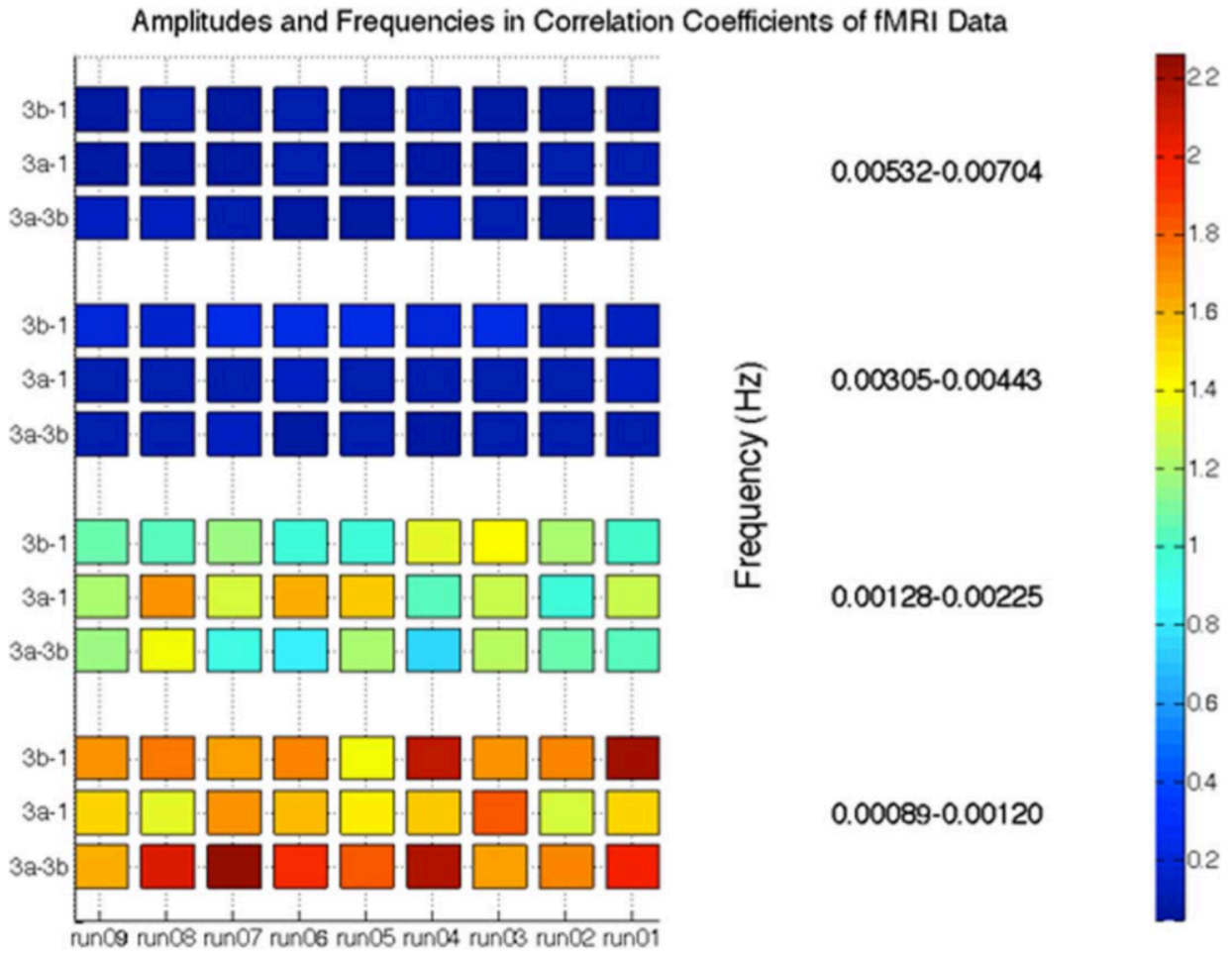

Figure 23 Spectral decomposition of the correlation coefficients for sub-region pairs of area 3a-3b, 3a-1, 3b-1.

Discussion

The aim of this study was to investigate the existence of dynamic correlations in real fMRI data acquired from somatosensory cortex of new world monkeys. It is widely accepted that apparent variations over time may arise from stationary signals when the sample duration is finite [Kiyani and Chapman, 2009; Nason, 2006]. Considering this factor, sliding window correlation analysis should be simulated with appropriate models and statistical tests. Based on our filtered stationary null model and the commonly used VAR model simulations for sliding window technique, we found that both stationary models reproduced the distribution of correlations of real fMRI signals well at short window sizes, but diverted at longer window sizes. This suggests that short window sizes are less reliable than long window sizes for detecting dynamic changes in functional correlations. In addition, a close representation of the behavior of resting-state data is obtained only when a dynamic correlation is introduced, suggesting that dynamic variations in connectivity are real.

Implication for the K-S Statistic on Correlations Between fMRI Data and the Null Models

As shown in Figure 19 and Figure 20, correlations between functionally related sub-regions in the monkey data are distributed similarly to the correlations derived from simulated stationary data at short window sizes, but depart substantially at larger window sizes. One possible explanation is that because we generated the filtered stationary null samples with only one prescribed single correlation coefficient that was calculated from the time series of the entire scan, the probability of realizing that prescribed correlation coefficient goes up as window size increases. The variance of the correlation coefficients decreases with larger window sizes, so the shape of the probability density function of correlations in the filtered stationary null model becomes narrower and taller. However, the probability density function of correlations in real fMRI data does not change as much with different window sizes, possibly because there are real dynamic changes within correlations between functionally related sub-regions. There clearly are some characteristics of correlations between functionally related sub-regions in the monkey data that the stationary null model cannot replicate. Given that the filtered stationary data are statistically stationary, these apparent dynamic changes at small window sizes arise from sampling variations

and more rigorous analysis is required to establish the existence of dynamic changes in connectivity.

The Underlying Dynamic Null Model in Time-Varying Correlations

As discussed above, correlations between functionally related sub-regions in monkeys are distributed similarly to the correlations derived from both stationary null models at short window sizes, but depart substantially at larger window sizes. Simultaneously, correlations between functionally unrelated pairs in the monkey data are distributed similarly to the stationary data from the filtered stationary null model simulation at all window sizes. One explanation for this phenomenon is that correlations between functionally related sub-regions are dynamically changing, while both stationary null models generate a static correlation through the entire series. However, for functionally unrelated sub-region pairs, it is clear that no correlation or dynamic changes exist within the data, so our filtered stationary null model can replicate it very well over a range of window sizes. To validate this hypothesis, we generated a dynamic null model using the underlying correlation function of the monkey data, applied the same sliding window technique, z transform and the two-sample K-S statistic as done to other two stationary null models. Figure 21b shows that correlations between functionally related sub-regions in the monkey data are distributed similarly to the correlations derived from the underlying dynamic null model regardless of window sizes, which indicates the underlying dynamic null model can replicate correlations between different functionally related subregions in the monkey data well. The underlying dynamic model is straightforwardly obtained by modifying the filtered stationary null model. Figure 22 indicates that the two stationary models do not simulate the trend of dynamic correlations within the monkey data. A closer representation of the behavior of monkey resting-state data is obtained only when a dynamic correlation is introduced. Whether there are additional features within the real monkey fMRI data that are not present in the underlying dynamic model simulated data remains unclear, but exploration of additional statistical metrics is underway.

Potential Limitations concerning Sliding Window Correlation Analysis

A sliding window correlation analysis is intended to identify pairwise variations in inter-regional time courses, but several potential limitations must be considered in applying this method and interpreting results. One limitation is that white noise can exhibit fluctuations in common functional connectivity metrics that are as large as those observed in real fMRI data. Before interpreting results about whether or not functional connectivity varies over a scan, one might need to consider whether the range of sliding window variability between ROIs is significantly different between two control populations (null model). Another limitation is the arbitrary manner in which window sizes are chosen. While many researchers tend to gravitate toward a short window size to better detect transient changes in connectivity, a large window is often necessary to allow for robust estimation of the correlation coefficient [Sakoglu et al., 2010]. As shown in the results of this article, a decrease in window size can lead to an overall increase in the variability of the functional connectivity since there are fewer time points available for computing correlation coefficients. Thus it will be difficult to distinguish between real phenomena related to brain signals and physiological noise. In our article, we developed a method for testing appropriate window sizes using a filtered stationary null model and K-S statistic.

Implications of Resting-State Functional Connectivity in Primary Somatosensory Cortex

The spectral decomposition analysis for the functional connectivity of three sub-region pairs (area 3a and 3b, area 3a and 1, area 3b and 1) has shown that the frequencies that dominated the cross-correlation coefficients for the functionally related sub-regions were below 0.003 Hz, which is reproducible across sub-region pairs and subjects. This may indicate that fluctuations in resting-state functional connectivity in primary somatosensory cortex are very slow.

Appendix

The correlation coefficient is one of several measures used to explore the idea of functional connectivity in the brain, particularly in the dynamic case. The correlation coefficient between two zero-mean signals is essentially a normalized version of the cross-correlation evaluated at the zero lag. Theoretically, the cross-correlation is evaluated using the ensemble average, i.e., via the expectation operator. In practice this is often impossible or at the very least impractical, and it is estimated by assuming stationarity and ergodicity and computing time averages. Even under these assumptions, the equivalence of the time average and the ensemble average is only guaranteed as the number of points, *N*, in the time average goes to infinity. The practical question becomes, how big does *N* need to be before we have a useful approximation to the theoretical ensemble average? Generally, this question does not have any simple answer, thus we attempt to analyze this particular cross-correlation problem.

We start by considering the case of computing the correlation of two stationary, partially correlated zero-mean random processes.

$$\varphi_{12}[m] = \frac{1}{N}(y_1[m] * y_2[-m])$$

where the * denotes convolution and

$$y_1[n] = x_1[n] + x_2[n]$$
$$y_2[n] = x_1[n] + x_3[n]$$

and the $x_i[n]$ signals are formed by filtering white noise through a bandpass filter with impulse response given by $h[n]$. The $w_i[n]$ signals are each zero-mean Gaussian white noise processes with variance σ_w^2.

$$x_1[n] = w_1[n] * h[n]$$
$$x_2[n] = w_2[n] * h[n]$$
$$x_3[n] = w_3[n] * h[n]$$

Thus we have the following expressions.

$$y_1[n] = (w_1[n] + w_2[n]) * h[n]$$
$$y_2[n] = (w_1[n] + w_3[n]) * h[n]$$

We can define $g[n] \triangleq h[n] * h[-n]$ to obtain $\varphi_{12}[m]$

$= \frac{1}{N} g[m] * \{(w_1[m] * w_1[-m]) + (w_2[m] * w_1[-m]) + (w_1[m] * w_3[-m]) + (w_2[m] * w_3[-m])\}$

Now define $\gamma_{ij}[m] \triangleq w_i[m] * w_j[-m]$ resulting in

$$\varphi_{12}[m] = \frac{1}{N} g[m] * \{\gamma_{11}[m] + \gamma_{21}[m] + \gamma_{13}[m] + \gamma_{23}[m]\}$$
$$= \frac{1}{N} g[m] * \gamma_{11}[m] + \frac{1}{N} g[m] * \gamma_{21}[m] \ldots$$
$$\ldots + \frac{1}{N} g[m] * \gamma_{13}[m] + \frac{1}{N} g[m] * \gamma_{23}[m]$$

The individual $\gamma_{ij}[m]$ terms simplify to the following.

$$\gamma_{ij}[m] = \begin{cases} \sum_{k=0}^{N-1-m} w_i[k+m] w_j[k] & , \quad m \geq 0 \\ \sum_{k=-m}^{N-1} w_i[k+m] w_j[k] & , \quad m < 0 \end{cases}$$

For $i \neq j$ each term in the sum is the product of two zero-mean independent Gaussians (each with variance σ_w^2), resulting in a *product normal* distributed random variable with zero-mean and variance of σ_w^4. Each term is *uncorrelated* with the others. For m=0, $\gamma_{ij}[m]$ is the sum of N of these random variables. For $m = \pm 1$ it is a sum of N-1 random variables, for $m = \pm 2$ it is a sum of N-2 random variables, and so on. For each value of m the sum is approximated by a zero-mean Gaussian random variable with a variance of $(N - m)\sigma_w^4$.

The same analysis holds for $i = j = 1$ and $m \neq 0$. For $m = 0$ we have $\gamma_{11}[0]$, the sum of the squares of *N* independent zero-mean Gaussian random variables each with a variance of σ_w^2. The resulting sum is distributed according to a *generalized Chi-square* distribution with a mean of $N\sigma_w^2$ and a variance of $2N\sigma_w^4$. The unnormalized cross-correlation that we actually want is $\varphi_{12}[m]$ evaluated at *m*=0. Combining all the above observations we find that $\varphi_{12}[0]$ can be modelled as a Gaussian random variable.

$$\varphi_{12}[0] \sim N(\mu, \sigma^2)$$

The expressions for the mean and variance are

$$\mu = g[0]\sigma_w^2$$

$$\sigma^2 = \frac{2g^2[0]}{N}\sigma_w^4 + \sigma_w^4 \sum_{k=1}^{N-1} \left(\frac{2}{N} g[k]\right)^2 (N-k) + 3\sigma_w^4 \sum_{k=-(N-1)}^{N-1} \left(\frac{1}{N} g[k]\right)^2 (N-k)$$

The behavior is most notably affected by the number of points *N* and the bandwidth of the low-pass filter.

In order to study the effect of the bandwidth of the filter on the variance of the correlation coefficient estimate, we should point out that is it well known that as the correlation approaches 1 or -1 the variance in the estimate decreases. This is due to fact that the estimate cannot exceed these limits, i.e., it's magnitude cannot exceed one. In order to minimize these endpoint effects and focus on the bandwidth effect we perform a simplified analysis with an underlying correlation of 0. This means that in the approach above, $x_1[n]$ and $w_1[n]$ are both zero. As a result we get $\varphi_{12}[m] = \frac{1}{N} g[m] * \gamma_{23}[m]$. This estimator of the covariance term (i.e., at *m*=0) can be shown to have a mean of zero and a variance of

$$\sigma^2 = \frac{g^2[0]}{N}\sigma_w^4 + \sigma_w^4 \frac{2}{N} \sum_{k=1}^{N-1} (g[k])^2 \left(\frac{N-k}{N}\right)$$

The correlation coefficient estimator is computed by dividing the covariance estimate by the square root of the products of the variances of $y_1[n]$ and $y_2[n]$, $\varphi_{11}[0]$ and $\varphi_{22}[0]$. It is straightforward to show that each of these variance estimators has a mean

$$\mu_1 = \mu_2 = g[0]\sigma_w^2$$

and a variance of

$$\sigma_1^2 = \sigma_2^2 = \frac{g^2[0]}{N}\sigma_w^4 + \sigma_w^4 \frac{2}{N}\sum_{k=1}^{N-1}(g[k])^2\left(\frac{N-k}{N}\right)$$

which is the same variance as for the covariance estimate.

Now we note that the mean of the variance estimates is nonzero and variances decrease with increasing *N*. For large *N* these variances can be made small relative to the mean value, so as a simplification we assume large *N* and replace the variance estimates with the means. In this case the estimator of the correlation coefficient becomes

$$\rho = \frac{\varphi_{12}[0]}{\sqrt{\mu_1\mu_2}}$$

Treating the denominator as a constant it is straightforward to show that the variance of the correlation coefficient estimator is given by

$$Var(\rho) = \frac{1}{N} + \frac{2}{N}\sum_{k=1}^{N-1}\left(\frac{g[k]}{g[0]}\right)^2\left(\frac{N-k}{N}\right)$$

The $g[k]/g[0]$ term can be viewed as a normalized function that has a value of 1 at *k*=0. This function will be broader and flatter as the bandwidth of the filter decreases, thus $Var(\rho)$ will increase with decreasing bandwidth.

References

Achard, S., Salvador, R., Whitcher, B., Suckling, J. and Bullmore, E. (2006) A resilient, low-frequency, small-world human brain functional network with highly connected association cortical hubs. *J Neurosci.,* **26**, 63–72.

Allen, E.A., Damaraju, E., Plis, S.M., Erhardt, E.B., Eichele, T. and Calhoun, V.D. (2014) Tracking whole-brain connectivity dynamics in the resting state. *Cereb Cortex,* **24**, 663–676.

Biswal, B., Yetkin, F.Z., Haughton, V.M. and Hyde, J.S. (1995) Functional connectivity in the motor cortex of resting human brain using echo-planar MRI. *Magn Reson Med.,* **34**, 537–541.

Chakravarti, L.R. (1967) Handbook of Methods of Applied Statistics, Volume I. *John Wiley and Sons*, 392–394.

Chang, C and Glover, G.H. (2010) Time-frequency dynamics of resting- state brain connectivity measured with fMRI. *Neuroimage,* **50**, 81–98.

Cordes, D., Haughton, V.M., Arfanakis, K., Wendt, G.J., Turski, P.A., Moritz, C.H., Quigley, M.A. and Meyerand, M.E. (2000) Mapping functionally related regions of brain with functional connectivity MR imaging. *AJNR Am J Neuroradiol.,* **21**, 1636–1644.

Cribben, I., Wager, T.D. and Lindquist, M.A. (2013) Detecting functional connectivity change points for single-subject fMRI data. *Front Comput Neurosci.,* **7**, 143.

Damoiseaux, J.S., Rombouts, S.A., Barkhof, F., Scheltens, P., Stam, C.J., Smith, S.M. and Beckmann, C.F. (2006) Consistent resting-state networks across healthy subjects. *Proc Natl Acad Sci USA,* **103**, 13848–13853.

Dosenbach, N.U., Fair, D.A., Miezin, F.M., Cohen, A.L., Wenger, K.K., Dosenbach, R.A., Fox, M.D., Snyder, A.Z., Vincent, J.L., Raichle, M.E., Schlaggar, B.L. and Petersen, S.E. (2007) Distinct brain networks for adaptive and stable task control in humans. *Proc Natl Acad Sci USA,* **104**, 11073–11078.

Fransson, P. (2005) Spontaneous low-frequency BOLD signal fluctuations: An fMRI investigation of the resting-state default mode of brain function hypothesis. *Hum Brain Mapp.,* **26**, 15–29.

Friston, K.J., Buechel, C., Fink, G.R., Morris, J., Rolls, E. and Dolan, R.J. (1997) Psychophysiological and modulatory interactions in neuroimaging. *NeuroImage,* **6**, 218–229.
Hacker, R.S. and Hatemi-J, A. (2005) A test for multivariate ARCH effects. *Appl Econ Lett*., **12**, 411–417.

Handwerker, D.A., Roopchansingh, V., Gonzalez-Castillo, J. and Bandettini, P.A. (2012) Periodic changes in fMRI connectivity. *Neuroimage,* **63**, 1712–1719.

Hindriks, R., Adhikari, M.H., Murayama, Y., Ganzetti, M., Mantini, D., Logothetis, N.K. and Deco, G. (2016) Can sliding-window correlations reveal dynamic functional connectivity in resting-state fMRI? *Neuroimage,* **127**, 242–256.

Hutchison, R.M., Womelsdorf, T., Gati, J.S., Everling, S. and Menon, R.S. (2013) Resting-state networks show dynamic functional connectivity in awake humans and anesthetized macaques. *Hum Brain Mapp.,* **34**, 2154–2177.

Jones, D.T., Vemuri, P., Murphy, M.C., Gunter, J.L., Senjem, M.L., Machulda, M.M., Przybelski, S.A., Gregg, B.E., Kantarci, K., Knopman, D.S., Boeve, B.F., Petersen, R.C. and Jack, C.R. Jr. (2012) Non-stationarity in the "resting brain's" modular architecture. *PLoS One,* **7**, 39731.

Kiyani, K.H. and Chapman, S.C. (2009) Pseudononstationarity in the scaling exponents of finite-interval time series. *Phys Rev E.,* **79**, 036109.

Marsaglia, G., Tsang, W.W. and Wang, J. (2003) Evaluating Kolmogorov's Distribution. *J Stat Softw.,* **8**, 1–4.

McKeown, M.J., Makeig, S., Brown, G.G., Jung, T.P., Kindermann, S.S., Bell, A.J. and Sejnowski, T.J. (1998) Analysis of fMRI data by blind separation into independent spatial components. *Hum Brain Mapp.,* **6**, 160–188.

Mezer, A., Yovel, Y., Pasternak, O., Gorfine, T. and Assaf, Y. (2009) Cluster analysis of resting-state fMRI time series. *Neuroimage,* **45**, 1117– 1125.

Nason, G.P. (2006) Stationary and non-stationary time series. In: Mader H, Coles SC, editors. *Statistics in Volcanology. The Geological Society*, 129–142. Chapter 11.

Sakoglu, U., Pearlson, G.D., Kiehl, K.A., Wang, Y.M., Michael, A.M., Calhoun, V.D. (2010) A method for evaluating dynamic functional network connectivity and task-modulation: Application to schizophrenia. *Magma,* **23**, 351–366.

Shah, A., Khalid, M.U. and Seghouane, A.K. (2012) Comparing causality measures of fMRI data using PCA, CCA and vector autoregressive modelling. *Conf Proc IEEE Eng Med Biol Soc.,* **2012**, 6184–6187.

Stephens, M.A. (1974) Edf statistics for goodness of fit and some comparisons. *J Am Stat Assoc.,* **69**, 730–737.

Sun, F.T., Miller, L.M. and D'Esposito, M. (2005) Measuring temporal dynamics of functional networks using phase spectrum of fMRI data. *Neuroimage,* **28**, 227–237.

Zalesky, A., Fornito, A., Cocchi, L., Gollo, L.L. and Breakspear, M. (2014) Time-resolved resting-state brain networks. *Proc Natl Acad Sci USA,* **111**, 10341–10346.

CHAPTER V

MARKOV MODEL-BASED ANALYSIS OF FUNCTIONAL CONNECTIVITY

Abstract

Functional MRI relies on detecting hemodynamic changes in neural tissues as revealed by BOLD signals to infer underlying local neuronal activity, while correlations between fluctuations in BOLD signals in a resting state are interpreted as measures of functional connectivity. To establish the relationships between BOLD signal fluctuations and underlying neural activity in a resting state, we compared spatial functional connectivity profiles between the coherence of different frequency bands of LFP signals from multielectrode array recordings and high resolution BOLD data at 9.4T within primary somatosensory (S1) cortex in monkeys. To characterize dynamic changes in functional connectivity, we measured the temporal variations of connectivity in both modalities and compared their probability distributions and changes using a modified Markov chain model-based approach. We found that within S1 cortex, low frequency LFP signal fluctuations dominated resting state LFP coherence, while evoked responses to stimuli were dominated by high frequency LFP responses. In addition, the coherences of low frequency LFPs varied significantly more frequently over time than those of high frequency LFPs. The dynamic changes of BOLD functional connectivity behaved more similarly to the LFP low frequency signal coherence than the LFP high frequency coherence. These results suggest that resting state BOLD connectivity measures are driven more by low frequency LFP signals and dynamic changes in their coherence.

Introduction

The identification of patterns of correlated, low frequency fluctuations in BOLD signals in a resting state has provided a remarkable tool to assess functional connectivity between regions in the brain, providing insights into how distributed cortical areas work together to achieve specific functions. However, BOLD signals are produced by hemodynamic effects that are only indirect indicators of underlying neural activity. Previous studies of the relationships between simultaneously recorded electrophysiological activity and hemodynamic changes in sensory systems have suggested that BOLD signals temporally correlate most strongly with local field potentials [Heeger et al., 2000; Mukamel et al., 2005]. Furthermore, our recent studies have indicated that at a columnar level, BOLD signals recorded at high magnetic field faithfully reflect underlying neuronal activity during stimulation, and the spatial profiles of local correlations in BOLD signals match those of LFP signals from the same region [Shi et al., 2017].

Although resting state correlations are already widely used to assess the functional architecture of the brain, the interpretation and application of fMRI-based functional connectivity studies rely on our understanding of the precise relationships between changes in neural activity and changes in cerebral hemodynamics. However, it remains unclear to what degree resting state fMRI connectivity reflects underlying neural couplings, and what features of electrical activity best align with BOLD metrics. In non-human primates, prominent LFP oscillations span a broad range of frequencies that are separable into delta (1-4 Hz), theta (5-8 Hz), alpha (9-14 Hz), beta (15-30 Hz), gamma low (31-50 Hz), gamma high (50-100 Hz), and gamma very high (100-150 Hz) bands. To date, there have been consistent reports of close relationships between BOLD signals and electrophysiological activity in gamma oscillations during stimulation, but there is no consensus yet about what LFP frequencies correspond to resting state signals. Specifically, in stimulation or task conditions, several fMRI studies have demonstrated strong temporal correlations between BOLD responses and power in the gamma band (30-150 Hz) of LFP signals [e.g. Shmuel et al., 2006]. However, in a resting state, while some studies suggest that lower frequency band fluctuations (< 20 Hz) may predominantly correspond to changes in BOLD signals [Lu et al., 2007; Wang et al., 2012; Wilson et al., 2016], other evidence suggests that slow changes in the gamma band of LFP signals contribute most to the spontaneous fluctuations in BOLD signals [Nir et al., 2008]. Moreover, resting state correlations of BOLD signals between regions appear to vary over time, and these apparent dynamic changes of fMRI connectivity may represent another

level of neural modulation, but few studies have directly compared the dynamic variations of connectivity seen in fMRI with corresponding LFPs, nor have they established which frequency bands are most relevant to these changes [Pan et al, 2011; Thompson et al., 2015]. No study, to our knowledge, has examined both the spatial relationships and the dynamic features of functional connectivity between BOLD signals and LFPs in different frequency bands within a well-defined, mesoscale functional network in a resting state.

The purpose of this study was to evaluate what frequency ranges of LFP coherences most parallel the dynamic features of BOLD functional connectivity in a resting state. We acquired high resolution (sub-millimeter) BOLD images at high field (9.4T) and multi-channel electrode array LFP recordings from primary somatosensory cortex (S1) in non-human primates. We first measured the spatial extents of BOLD activations in response to tactile stimuli as well as the spatial profiles of single-voxel local correlations in a resting state. We then quantitatively compared these with the spatial extents of LFPs in each of seven frequency bands, and their inter-electrode coherences, in the same conditions and brain regions. In order to compare dynamic features of resting state connectivity, we devised a modified Markov chain model-based approach combined with a sliding window correlation analysis. We aimed to quantitatively compare the time-varying patterns of functional correlations between BOLD and frequency-specific LFPs in individual monkeys, and to determine what frequency ranges of the LFP coherence dominate changes in dynamic BOLD functional correlations in S1 cortex.

Local field potentials recording and analysis

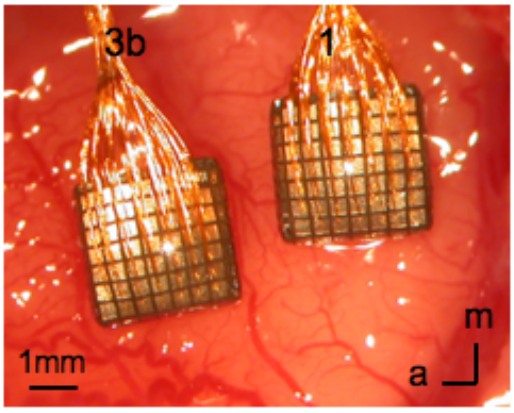

Figure 24 Blood vessel map shows the two 7 x 7 multi-channel electrode arrays were inserted in the digit regions of areas 3b and 1 under surgical microscope guidance in one representative monkey.

Guided by MRI maps and blood vasculature patterns, two 7 × 7 multichannel Utah electrode arrays (Figure 24, 98 channels in total, spacing between each electrode, 400 μm) were carefully inserted into area 3b and area 1 cortex [Shi et al., 2017]. LFP signals were sampled at 500 Hz and then band-pass filtered into eight frequency ranges using a second order, zero-phase Chebyshev type-1 filter. The frequency ranges were the following: delta (1-4 Hz), theta (5-8 Hz), alpha (9-14 Hz), beta (15-30 Hz), gamma low (30-50 Hz), gamma high (50-100 Hz), gamma very high (100-150 Hz) and broad band (1-150 Hz). For the stimulation condition, a time-frequency analysis was conducted to evaluate the temporal structure of the LFP signals and their stimulus response preferences. A Fourier transform was performed on each single trial and the resulting spectrograms were averaged. Computed spectrograms of stimulus-evoked LFPs were transformed into a dB scale ($10 \times \log_{10}$) and used for further analysis. To estimate more accurately the mean power of the steady-state LFP responses, we excluded the data from the first 10 sec after the stimulus onset in our calculation, according to previous observations. For LFP resting state coherence analysis in all frequency bands, magnitude squared coherence was calculated between each selected seed electrode and the other electrodes.

FMRI data acquisition

MR imaging was performed with a 9.4 T 21 cm bore magnet and Varian/Agilent Inova spectrometer (Varian Inc., Palo Alto, CA), using a 3-cm surface transmit-receive coil secured over the sensory cortex. Scout images obtained using a fast gradient-echo sequence were used to define a volume covering the primary somatosensory cortex in which static magnetic field homogeneity was optimized, and to plan four oblique slices for structural and functional imaging. T_2^*-weighted gradient-echo structural images [repetition time (TR) = 200 ms; echo time (TE) = 16 ms; four slices, FOV = 35 × 35 mm^2, 512 × 512 matrix; spatial resolution = 0.068 × 0.068 × 2 mm^3; number of excitations = 6] were acquired to identify venous structures on the cortical surface to help locate S1 cortex and as structural features for co-registration of fMRI images. Within each imaging session, multiple runs (up to 6) of stimulus-evoked and resting state fMRI data were acquired with identical image acquisition sequences (gradient echo-planar sequence; TR = 750 ms; TE = 16 ms, number of excitations = 4), and slice placement. Functional images were obtained at imaging resolutions of 0.274 × 0.274 × 2 mm^3. Each high resolution stimulation run contained 150 continuous volumes. For resting state fMRI runs, 300 continuous image volumes were acquired. MR images were reconstructed on the MR console (Varian VnmrJ) and exported to Matlab (Mathworks) for analysis.

Markov Chain

Previous studies have shown that correlations between regions vary over time, so that resting state connectivity changes dynamically. We consider the instantaneous degree of correlation between regions to represent a brain state, so that changes in connectivity correspond to transitions between brain states. The number of such states is unknown but we assume they may span the range between perfectly correlated and perfectly anti-correlated, and this range can then be divided into a finite number of discrete intervals. Measurements of the variations over time in correlation values allow the

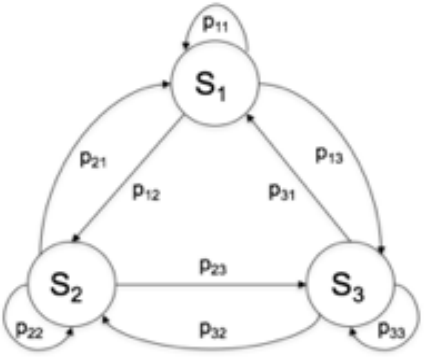

Figure 25 Example of a probability transition diagram for 3-state Markov chain.

construction of a probability distribution of the states, along with probabilities for transitions from any one state to another. A discrete-time Markov chain model is a tool for representing probability distributions over a sequence of states in which the probability of moving to the next state depends only on the present state [Markov, 1913]. Markov chains are often illustrated by a sequence of directed graphs (see Figure 25) representing the probabilities of going from one state at time *t* to any other states at time *t+1*.

Markov model-based approach combined with a sliding window technique

A sliding window correlation analysis technique is a method for capturing variations in inter-regional synchrony, and is commonly used to investigate dynamic changes in correlations between time courses in various modalities. Resting state correlations between the BOLD time series derived from areas 3b and 1 within S1 cortex were calculated using a sliding window technique with a window size of 60 sec. The window was shifted in time in 3 sec increments (equal to time between image volumes) along the entire time series and the correlation coefficient was recalculated. As the sampling distribution of Pearson's r is not normally distributed, correlation coefficients were converted to z-scores using Fisher's z transform. The z-scores from -1 to 1 were binned into 50 equal steps, which represent 50 possible brain states characterized by their differing degree of correlations between areas 3b and 1. A similar sliding window technique was used to classify the LFP signals. In this analysis, however, the magnitude squared coherence values for each frequency band were computed from the raw LFPs instead of Pearson's correlation coefficients. We then quantified the resemblance of the temporal variations in the correlations between BOLD and frequency-specific LFP signals by constructing the empirical cumulative distribution functions (ECDFs) for jumps between states, which represent the probability functions for transitions between different degrees of connectivity. A two-sample Kolmogorov-Smirnov (K-S) statistic was used to evaluate whether the BOLD and LFP ECDFs were derived from the same population with a specific distribution, based on measurements of the distance between two ECDFs. This test is sensitive to differences in both the location and shape of the ECDFs of the two samples. Lower K-S values between BOLD and LFP in a certain frequency band suggest increased similarity in the nature of the dynamic changes in functional connectivity.

Measurements of the PSFs of BOLD and LFP Signals in Stimulation and Resting States

We identified activation foci in areas 3b and 1, whose shapes could be well approximated as elliptical. In each animal, activation maps of three different digit tips (digits 2, 3, 4) were typically obtained. A threshold of 0.7 was used to identify the center of mass in each ROI. The axis along the individual digit activation centers was then determined as the lateral to medial axis within each area (3b and 1). The perpendicular anterior-posterior direction of this axis was then determined along the digit bottom to tip representation. From the fitting, the major (in the lateral to medial direction) and minor (in the anterior to posterior direction) axes of the ellipse were determined, and all values above 0.2 along the major and minor axes within the sub-region were used in the subsequent Gaussian fitting. The point spread functions (PSFs) of the single digit tactile stimulation evoked BOLD fMRI activation maps were measured in both areas 3b and 1. The coordinates of the center of mass, and the major and minor axes of the ellipse were determined by fitting. The spatial distributions of percentage of BOLD signal changes along the major and minor axes were then fit with Gaussian functions. The full-width of half maximum (FWHM) of each fitted Gaussian was then computed. For resting state fMRI runs, ROI seeds were identified based on the vibrotactile stimulus-evoked activation maps. The voxels with the highest % BOLD signal change were chosen as the seeds for each digit in either areas 3b or 1. Resting state BOLD signal time courses were extracted from the seed voxels and then used as the reference models in subsequent voxel-wise correlation analyses. Correlation coefficients were computed for each voxel surrounding the seed, and then local functional connectivity maps were generated for each seed. Identical spatial fitting procedures were applied to derive the FWHM and area of Gaussian PSFs of fitted local correlation profiles.

The same spatial ellipsoid fitting method was used to quantify the PSFs of LFP signals in each of the eight frequency bands. Multi-channel electrode array response maps were computed based on the percentages of signal power changes between 20 sec of stimuli presentations and 20 sec of the pre-stimuli periods for single digit stimulations. Activation maps were then resampled at higher resolution (0.10×0.10 mm^2) for further sub-voxel processing. Within each LFP stimulus run, the percentages of signal power changes of cortical activation areas were normalized to their maximum values during each run. A similar approach as described above was used to compute the point-spread functions of stimulus local field potential responses of areas 3b and 1 in S1 cortex. For resting-state local field potentials, ROI seeds were identified based on the array stimulus

response maps. Electrodes with the largest percentage of signal power change for single digit stimulations were selected as seeds. To evaluate the spatial profiles of resting-state LFP correlations, we first placed one ROI seed (either area 3b or area 1) and computed its functional connectivity map based on functional coherence between this seed and the rest of the electrodes. We then used the same approach as described above to compute the PSFs of resting-state LFP correlations of this area.

The spatial extents of frequency-specific LFPs in stimulation and resting states

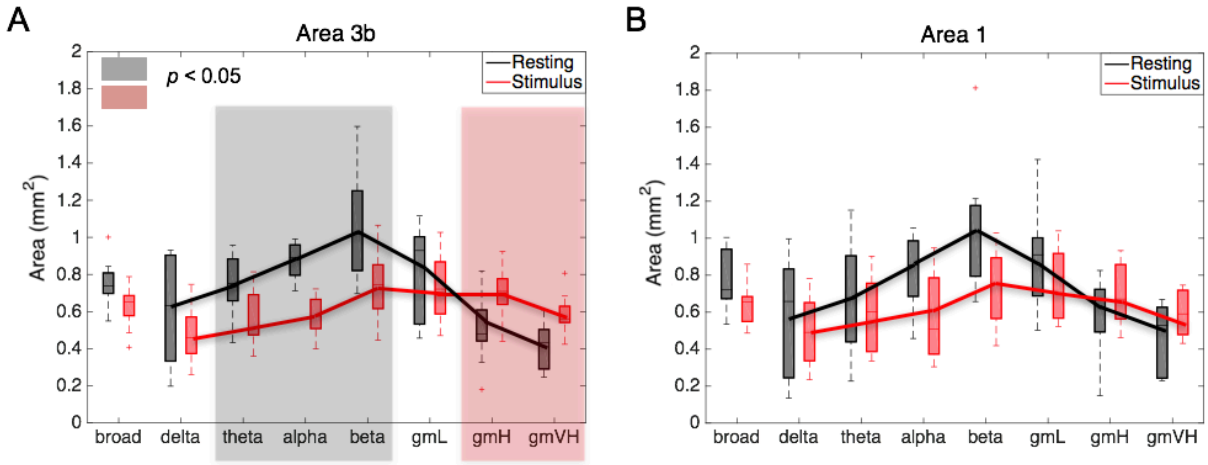

Figure 26 Comparison of spatial extents of LFP signals in eight frequency bands in areas 3b and 1, between resting state and stimulation. (A-B) The area values of areas 3b and 1, respectively, in both resting (black boxes) and stimulus (red boxes) conditions, significance at p<0.05 (Figure 26A: Wilcoxon signed-rank test, as shown in the grey and pink background). A total of 9 runs from three monkeys were analyzed for LFP measurements.

Figure 26 reports the spatial changes in power and coherence characteristics of the LFP signals in different frequency bands during stimulation and resting states. Wilcoxon signed-rank test showed that in a resting state (black boxes), in area 3b, the local correlation profiles of LFP signals in the frequency ranges between 5 and 30 Hz were significantly broader in extent than those in the frequency ranges between 50 and 150 Hz. In addition, the local correlation profiles of the broadband (1-150 Hz) LFPs had no significant differences from those of low frequency (1-15 Hz) and gamma low (30-50 Hz) LFPs. Direct comparisons of the area values between stimulation and resting states showed that, in area 3b, the spatial extents of resting state electrode-electrode coherence in the frequency ranges between 5 to 30 Hz and the broad band were significantly wider than those of stimulation responses (Wilcoxon signed-rank test: $p < 0.05$; Figure 26A, the grey background), while the spatial extents of resting state coherence in the frequency ranges between 50 and 150 Hz are significantly narrower than those of stimulation responses ($p < 0.05$; Figure 26A, the pink background), a feature that was not statistically significant in area 1 (Figure 26B).

These comparisons revealed that the local correlation profiles of broadband resting state LFPs were closer to those of low frequency LFPs than high frequency LFPs. In addition, low frequency LFP signal fluctuations spatially dominated resting state LFP coherence, while stimulus responses were dominated by high frequency LFP responses.

The behavior of LFP coherence in different frequency ranges

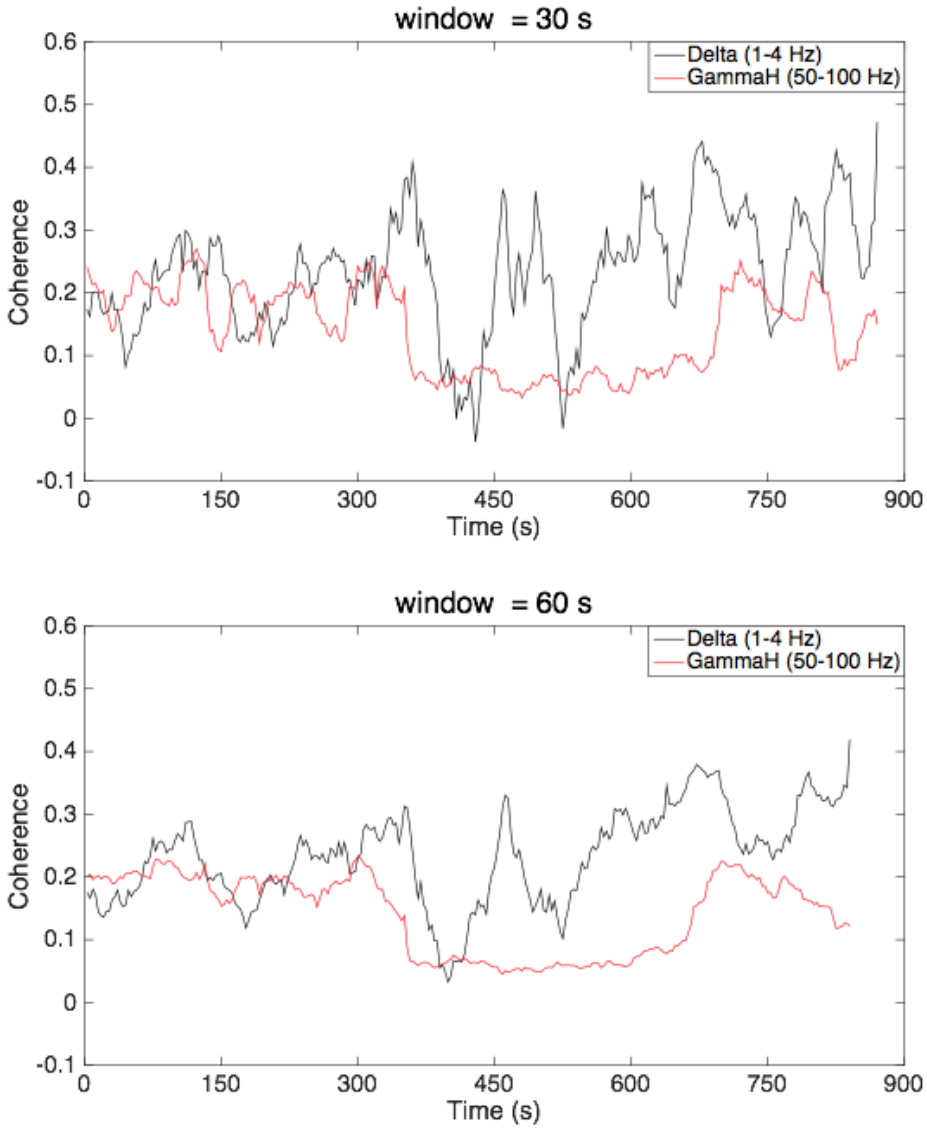

Figure 27 Examples of a sliding window coherence analysis between areas 3b and 1, comparing delta band LFPs (black line: 1-4 Hz) and gamma high band LFPs (red line: 50-100 Hz), with a window size of 30 sec and 60 sec, respectively.

We next investigated the dynamic changes in frequency-specific LFP coherences using a sliding window technique. The selection of window size was based on our previous studies [Shi et al., 2016], but we also qualitatively evaluated whether smaller window sizes would reveal additional apparent changes in resting state connectivity than large window sizes. Figure 27 shows an example of a sliding window coherence analysis between areas 3b and 1, comparing delta band LFPs (low frequency: 1-4 Hz) and gamma high band LFPs (high frequency: 50-100 Hz), with a window size of 30 sec and 60 sec, respectively. Here, there are no significant differences in the dynamic patterns of functional correlations. The low frequency LFP coherence changes faster over time than high frequency LFP coherence. We quantified this difference by analyzing the spectral composition of the coherence between areas 3b and 1 in resting state BOLD signals and frequency-specific LFPs. We quantitatively compared the cumulative percentage of frequency components derived from the resting state BOLD correlations and frequency-specific LFP coherence. Figure 28 shows a group analysis of the spectral decomposition of the coherence between areas 3b and 1 in resting state BOLD signals and LFPs in seven frequency bands. From Figure 28B, a Wilcoxon signed-rank test showed that variations in frequency components >0.02 Hz contributed significantly more to the resting state BOLD correlations and low frequency LFP coherence (1-15 Hz), than high frequency LFP coherence (15-150 Hz). From Figure 28F, it was observed that variation frequency components between 0 and 0.0025 Hz had significant more contributions to the resting state high frequency LFP coherence, than low frequency LFP coherence and BOLD correlations. Results of LFP coherence in seven frequency bands showed that coherence of low frequency (1-15 Hz) LFP signals contained significantly more <50 sec cycles than that of high frequency (15-150 Hz) LFP signals, while coherence of high frequency LFPs contained significantly more >400 sec cycles than that of low frequency LFPs.

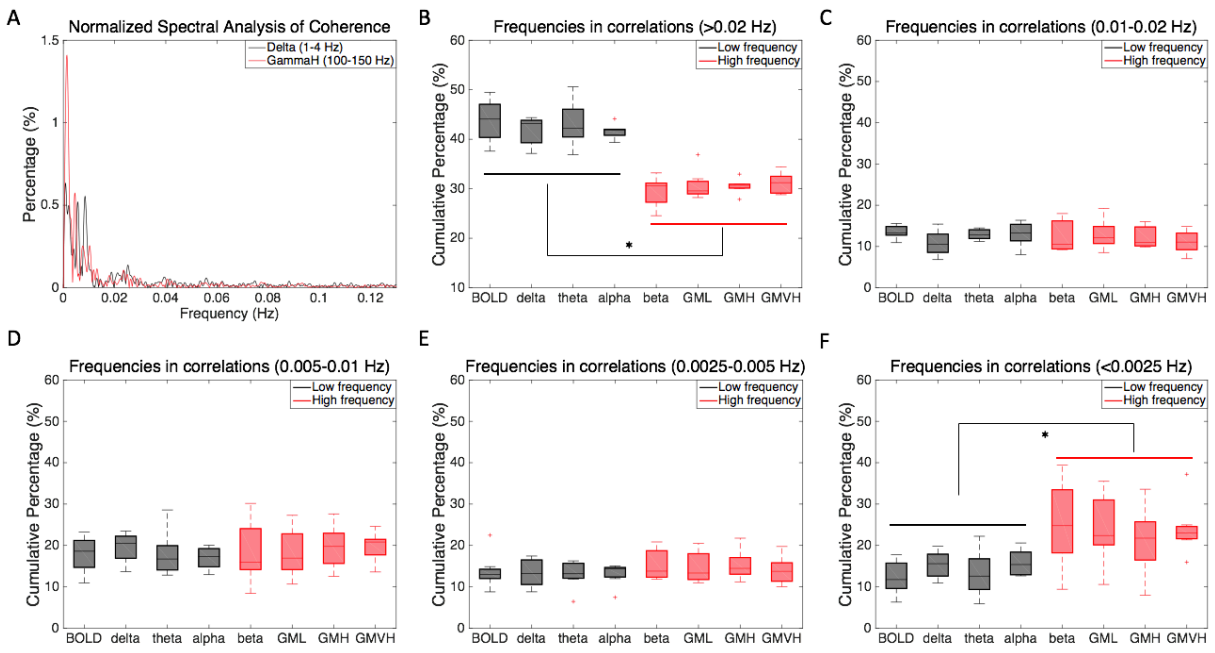

Figure 28 Group analysis on the spectral decomposition of the coherence between areas 3b and 1 in resting state BOLD signals and LFPs in seven frequency bands. (A) Normalized percentage of spectral analysis of sliding window coherence, comparing LFP delta (black) and gamma high (red) bands. (B-F) Cumulative percentage of variation frequency components in correlations at different frequency bands; (B) over 0.02 Hz; (C) between 0.01 and 0.02 Hz; (D) between 0.005 and 0.01 Hz; (E) between 0.0025 and 0.005 Hz; (F) less than 0.0025 Hz. Wilcoxon signed-rank test at $p<0.05$. A total of 9 runs from three monkeys were analyzed for BOLD and LFP measurements, respectively.

Comparisons of dynamic connectivity between BOLD and frequency-specific LFPs

We finally investigated the dynamic changes of functional connectivity in BOLD and frequency-specific LFPs using a Markov chain model-based approach combined with a two sample K-S statistic. We quantitatively compared the time-varying patterns of correlations between areas 3b and 1, between BOLD and LFP signals in eight frequency bands. Figure 29 showed the K-S statistic for group differences of fMRI correlations and their corresponding monkey's LFP coherence between areas 3b and 1, in eight frequency bands. The correlations derived from resting state BOLD signals were distributed more similarly to the LFP coherence in broad band (1-150 Hz) and low frequency bands (1-15 Hz, black boxes), than to the LFP coherence in high frequency bands (30-150 Hz, red boxes), with substantial differences appearing between

50 and 150 Hz. Specifically, K-S values of correlation coefficient distributions between areas 3b and 1 of the BOLD signals and LFPs in broad band and low frequency bands were significantly smaller than those of the same BOLD signals and LFPs in high frequency bands. These results indicated that the dynamic changes of BOLD functional correlations behaved more closely to those of low frequency than high frequency LFP coherence.

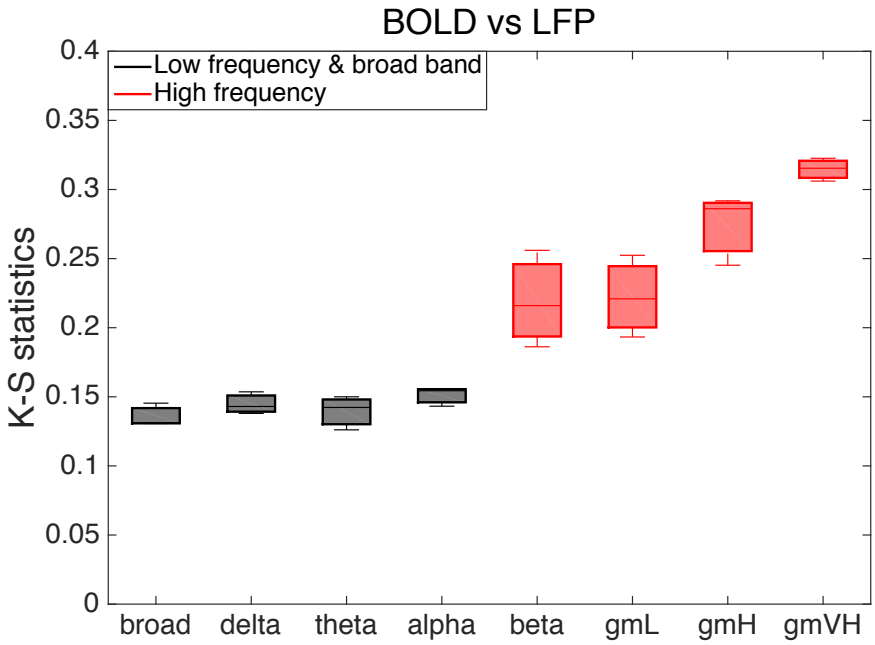

Figure 29 Group analysis on Kolmogorov-Smirnov statistic between BOLD fMRI correlations and their corresponding monkey's LFP coherence in eight frequency bands, between areas 3b and 1. Dynamic changes in sliding window correlations in BOLD data were distributed more closely to low frequency LFPs (black, 1-15 Hz) and broad band LFPs (black boxes, 1-150 Hz) coherence, while differed from LFP coherence at high frequency bands (red boxes, 15-150 Hz).

Discussion

The aim of this study was to investigate in what frequency ranges LFP coherence shared the strongest characteristics with BOLD functional connectivity in a resting state, both spatially and temporally, at a columnar level meso-scale in the primary somatosensory cortex of nonhuman primates. Currently, there is no consensus as to whether low or high frequency LFP signals contribute most to the spontaneous fluctuations in fMRI signals [Lu et al., 2007; Nir et al., 2008; Thompson et al., 2015]. We spatially compared the local correlation profiles of resting state BOLD signals with those of 'gold standard' electrophysiological LFP measurements, and investigated the temporal dynamic changes in functional connectivity of both modalities. We found that within S1 cortex, low frequency LFP signal fluctuations spatially dominated resting state broadband LFP coherence. In addition, our Markov model-based approach combined with a sliding window technique showed that coherences of low frequency LFPs changed significantly faster over time than those of high frequency LFPs. Finally, our results suggested that the dynamic changes of BOLD functional connectivity behaved more closely to those of LFP low frequency coherence than those of high frequency coherence. These indicate that resting state BOLD dynamic connectivity are reflective more of low frequency LFP coherence than high frequency LFP coherence.

Low frequency LFP signal fluctuations spatially dominate resting state LFP coherence

The local correlation profile of LFP signals within S1 cortex in a resting state directly measures the contributions from the intrinsic spatial distribution of the neural activity involved, and can potentially reflect how neurons spatially work together at a columnar level. No previous study, to our knowledge, has reported the spatial relationships of LFP signals in different frequency ranges during stimulation or in a resting state. We found that in a resting state, the local correlation profiles of LFP signals from the frequency ranges between 50 and 150 Hz were significantly smaller than those of the frequency ranges between 5 and 30 Hz. This may suggest that in a resting state, neurons generating high frequency LFP signals (50-150 Hz) may intrinsically communicate more focally within a finer-scale cortical microcircuit [Borgers et al., 2005; Fries et al., 2007; Fries, 2009], than those generating low frequency LFP signals (1-15 Hz). In addition, evidence has shown that the neural oscillations of frequency-specific LFP signals may be generated by various types of neurons in different neuronal process pathways [Buzsaki and Draguhn, 2004; Logothetis

et al., 2007; Berens et al., 2008]. The primary somatosensory cortex is a cortical region receiving a convergence of anatomical connections from structures in the cortico-thalamic and cortico-cortical loops [Lin et al., 1979; Iwamura, 1998; Reed et al., 2008]. Low frequency oscillations can occur in a cortico-thalamic feedback loop. These slow oscillations are described to be modulated by global neuronal inputs [Steriade et al., 1993; Steriade, 2006; Berens et al., 2008]. However, high frequency LFPs, such as gamma-waves, most likely arise locally within cortical microcircuits that include pyramidal cells and interneurons [Mann et al., 2005; Berens et al., 2008; Cardin et al., 2009; Sohal et al., 2009], and therefore, present a constrained local spatial correlation profile. Our results also showed that in a resting state, the local correlation profiles of broadband LFPs had no significant difference from those of low frequency LFPs (1-15 Hz) and gamma low band (30-50 Hz). Furthermore, we directly compared the spatial profiles between stimulation and resting state conditions in both areas 3b and 1, respectively. We found that in area 3b, the spatial extents of resting state electrode-electrode coherence in the broad band (1-150 Hz) and the frequency ranges between 5 and 30 Hz were significantly larger than those of stimulation responses. However, in the frequency ranges between 50 and 150 Hz, the spatial extents of resting state coherence were significantly smaller than those of stimulation responses, a feature that was not statistically significant in area 1. These comparisons revealed that low frequency LFP signal fluctuations spatially dominated resting state LFP coherence, while stimulus responses were dominated by high frequency LFP responses. This resting state phenomenon could be insignificant (e.g., area 1), or potentially vary in different brain regions. For example, in the hippocampus, strong theta oscillations (5-8 Hz) are the most prominent feature in LFP signals and are believed to be critical for hippocampal-cortical interactions [Siapas et al., 2005; Sirota et al., 2008], while in visual cortex, fast oscillations in the gamma band between 30 and 90 Hz are dominant during resting states [Niessing et al., 2005; Berens et al., 2008].

BOLD resting state dynamic connectivity behaves more closely to low frequency than high frequency LFP coherence

Our previous studies found that the inter-center distance variation between BOLD and LFP modalities was less than 0.35 mm in S1 cortex of nonhuman primate brain [Shi et al., 2017]. Despite the high spatial correspondence between high-resolution fMRI and LFP, separate identifications of the ROI seeds for BOLD and LFP experiments can potentially increase the

accuracy of comparisons between both modalities, especially in a resting state seed-based analysis. Therefore, we identified the ROI seeds in BOLD fMRI and LFP separately, according to their activation maps, and used the seeds for resting state analysis in each individual monkey. In Figure 27 and Figure 28, the resting state sliding window LFP coherence analysis between areas 3b and 1 in seven frequency bands shows that coherences of low frequency (1-15 Hz) LFP signals change significantly faster over time than those of high frequency (15-150 Hz) LFP signals. As shown in Figure 29, the correlations derived from resting state BOLD signals between areas 3b and 1 were distributed more similarly to the LFP coherence in broad band (1-150 Hz) and low frequency bands (1-15 Hz), than in high frequency bands (30-150 Hz). These results indicate that in a resting state, the dynamic changes of BOLD functional correlations behave more closely to those of low frequency than high frequency LFP coherence in S1 cortex. One possible hypothesis is that in S1 cortex, the frequency ranges from 0.01 to 0.1 Hz of resting state BOLD fMRI signals that are standard in preprocessing procedures are more reflective of the cortico-thalamic feedback loop. Another possible hypothesis could be that, based on what is reported in the literature, it can be generally assumed that large vessels located on the pial surface of the brain have the strong contribution to the BOLD signals for superficial-superficial layer connectivity [Jin and Kim, 2008; Huber et al., 2016], where some electrophysiological studies have shown that delta (1-4 Hz) and alpha (9-14 Hz) generators were present in each of the cortical layers, with a strong source in superficial layers [Carracedo et al., 2013; Haegens et al., 2015]. It is worth further investigating the laminar profile of LFP signals in different frequency ranges, and the spatial and temporal relationships between cortical layer-specific BOLD signals and their corresponding LFPs.

References

Berens, P., Keliris, G.A., Ecker, A.S., Logothetis, N.K. and Tolias, A.S. (2008) Feature selectivity of the gamma-band of the local field potential in primate primary visual cortex. *Front Neurosci.,* **2**, 199-207.

Borgers, C., Epstein, S. and Kopell, N.J. (2005) Background gamma rhythmicity and attention in cortical local circuits: a computational study. *Proc. Natl. Acad. Sci. USA,* **102**, 7002–7.

Buzsaki, G. and Draguhn, A. (2004) Neuronal Oscillations in Cortical Networks. *Science,* **304**, 1926-1929.

Cardin, J.A., Carlen, M., Meletis, K., Knoblich, U., Zhang, F., Deisseroth, K., Tsai, L. and Moore, C.I. (2009) Driving fast-spiking cells induces gamma rhythm and controls sensory responses. *Nature,* **459**, 663- 667.

Carracedo, L.M., Kjeldsen, H., Cunnington, L., Jenkins, A., Schofield, I., Cunningham, M.O., Davies, C.H., Traub, R.D. and Whittington, M.A. (2013) A neocortical delta rhythm facilitates reciprocal interlaminar interactions via nested theta rhythms. *J. Neurosci.*, **33**, 10750-10761.

Fries, P. (2009) Neuronal gamma-band synchronization as a fundamental process in cortical computation. *Annu Rev Neurosci.,* **32**, 209–224.

Fries, P., Nikolic, D. and Singer, W. (2007) The gamma cycle. *Trends in Neurosciences,* **30**, 309-316.

Haegens, S., Barczak, A., Musacchia, G., Lipton, M.L., Mehta, A.D., Lakatos, P. and Schroeder, C.E. (2015) Laminar profile and physiology of the α rhythm in primary visual, auditory, and somatosensory regions of neocortex. *J. Neurosci*., **35**, 14341-14352.

Heeger, D.J., Huk, A.C., Geisler, W.S. and Albrecht, D.G. (2000) Spikes versus BOLD: What does neuroimaging tell us about neuronal activity? *Nat Neurosci.,* **3**, 631–633.

Huber, L., Goense, J., Kennerley, A.J., Trampel, R., Guidi, M., Reimer, E., Ivanov, D., Neef, N., Gauthier, C.J., Turner, R. and Moller, H.E. (2015) Cortical lamina-dependent blood volume changes in human brain at 7 T. *Neuroimage,* **107**, 23-33.

Iwamura, Y. (1998) Hierarchical somatosensory processing. *Curr Opin Neurobiol.,* **8**, 522–528.

Jin, T. and Kim, S.G. (2008) Cortical layer-dependent dynamic blood oxygenation, cerebral blood flow and cerebral blood volume responses during visual stimulation. *Neuroimage,* **43**, 1-9.

Lin, C.S., Merzenich, M.M., Sur, M. and Kaas, J.H. (1979) Connections of Areas 3b and 1 of the parieta) somatosenaory strrp with the ventroposterior nucleus in the owl monkey (Aotus tricirgatus). *J. comp. Neurol.,* **185**, 355-371.

Logothetis, N.K., Kayser, C. and Oeltermann, A. (2007) In Vivo Measurement of Cortical Impedance Spectrum in Monkeys: Implications for Signal Propagation. *Neuron,* **55**, 809-823.

Lu, H., Zuo, Y., Gu, H., Waltz, J.A., Zhan, W., Scholl, C.A., Rea, W., Yang, Y. and Stein, E.A. (2007) Synchronized delta oscillations correlate with the resting-state functional MRI signal. *Proc Natl Acad Sci USA,* **104**, 18265–18269.

Mann, E.O., Radcliffe, C.A. and Paulsen, O. (2005) Hippocampal gamma-frequency oscillations: from interneurones to pyramidal cells, and back. *J Physiol.,* **562**, 55-63.

Markov, A.A. (1913) An example of statistical investigation of the text Eugene Onegin concerning the connection of samples in chains. (In Russian) *Bulletin of the Imperial Academy of Sciences of St. Petersburg,* **7**, 153–162.

Mukamel, R., Gelbard, H., Arieli, A., Hasson, U., Fried, I. and Malach, R. (2005) Coupling between neuronal firing, field potentials, and FMRI in human auditory cortex. *Science,* **309**, 951–954.

Niessing, J., Ebisch, B., Schmidt, K.E., Niessing, M., Singer, W. and Galuske, R.A.W. (2005) Hemodynamic Signals Correlate Tightly with Synchronized Gamma Oscillations. *Science,* **309**, 948-951.

Nir, Y., Mukamel, R., Dinstein, I., Privman, E., Harel, M., Fisch, L., Gelbard-Sagiv, H., Kipervasser, S., Andelman, F., Neufeld, M.Y., Kramer, U., Arieli, A. and Fried, I., Malach, R. (2008) Interhemispheric correlations of slow spontaneous neuronal fluctuations revealed in human sensory cortex. *Nat Neurosci.,* **11**, 1100–1108.

Pan, W.J., Thompson, G., Magnuson, M., Majeed, W., Jaeger, D. and Keilholz, S. (2011) Broadband local field potentials correlate with spontaneous fluctuations in functional magnetic resonance imaging signals in the rat somatosensory cortex under isoflurane anesthesia. *Brain Connect.,* **1**, 119–131.

Reed, J.L., Pouget, P., Qi, H.X., Zhou, Z., Bernard, M.R., Burish, M.J., Haitas, J., Bonds, A.B., and Kaas, J.H. (2008) Widespread spatial integration in primary somatosensory cortex. *Proc. Natl. Acad. Sci. USA,* **105**, 10233-10237.

Shi, Z., Rogers, B.P., Chen, L.M., Morgan, V.L., Mishra, A., Wilkes, D.M. and Gore, J.C. (2016) Realistic models of apparent dynamic changes in resting-state connectivity in somatosensory cortex. *Hum Brain Mapp.,* **37**, 3897–910.

Shi, Z., Wu, R., Yang, P.F., Wang, F., Wu, T.L., Mishra, A., Chen, L.M. and Gore, J.C. (2017) High spatial correspondence at a columnar level between activation and resting state fMRI signals and local field potentials. *Proc Natl Acad Sci USA,* **114**, 5253-5258.

Shmuel, A., Augath, M., Oeltermann, A. and Logothetis, N.K. (2006) Negative functional MRI response correlates with decreases in neuronal activity in monkey visual area V1. *Nat Neurosci.,* **9**, 569–577.

Siapas, A.G., Lubenov, E.V. and Wilson, M.A. (2005) Prefrontal Phase Locking to Hippocampal Theta Oscillations. *Neuron,* **46**, 141-151.

Sirota, A., Montgomery, S., Fujisawa, S., Isomura, Y., Zugaro, M. and Buzsaki, G. (2008) Entrainment of Neocortical Neurons and Gamma Oscillations by the Hippocampal Theta Rhythm. *Neuron,* **60**, 683- 697.

Sohal, V.S., Zhang, F., Yizhar, O. and Deisseroth, K. (2009) Parvalbumin neurons and gamma rhythms enhance cortical circuit performance. *Nature,* **459**, 698-702.

Steriade, M. (2006) Grouping of brain rhythms in corticothalamic systems. *Neuroscience,* **137**, 1087- 1106.

Steriade, M., McCormick, D. and Sejnowski, T. (1993) Thalamocortical oscillations in the sleeping and aroused brain. *Science,* **262**, 679-685.

Thompson, G.J., Pan, W.J. and Keilholz, S.D. (2015) Different dynamic resting state fMRI patterns are linked to different frequencies of neural activity. *Journal of Neurophysiology*, **114**, 114-24.

Wang, L., Saalmann, Y.B., Pinsk, M.A., Arcaro, M.J. and Kastner, S. (2012) Electrophysiological low-frequency coherence and cross-frequency coupling contributes to BOLD connectivity. *Neuron,* **76**, 1010–1020.

Wilson, G.H., 3rd, Yang, P.F., Gore, J.C. and Chen, L.M. (2016) Correlated inter-regional variations in low frequency local field potentials and resting state BOLD signals within S1 cortex of monkeys. *Hum Brain Mapp.,* **37**, 2755–2766.

CHAPTER VI

SUMMARY AND FUTURE DIRECTION

Summary

The purpose of this thesis was to investigate to what extent functional MRI signals reflect underlying neural activities in both stimulation and resting states, and to evaluate the dynamic nature of functional connectivity in both fMRI and electrophysiological data. This dissertation reports that BOLD signal changes within single-digit representation columns in the primary somatosensory cortices of areas 3b and 1 aligned spatially very closely with LFP signals in response to tactile stimulation. In addition, resting state BOLD fMRI and LFP signals also exhibited very similar intervoxel spatial correlation profiles. These findings indicate that at a columnar level, BOLD signals faithfully reflect underlying neuronal activity both during information processing and at rest. Importantly, the spread of BOLD activity and correlations at high field are no greater than the extent of LFP signals.

The broad band LFP signals probably reflect assorted contributions from several different neural processing pathways, and are traditionally decomposed and analyzed in the frequency domain, with the hypothesis that each frequency band may represent corresponding underlying neural process. For example, some studies have reported that the oscillations of resting state low frequency LFPs are modulated by global neuronal signals [Steriade et al., 1993; Steriade, 2006], while resting state high frequency LFPs generated in different brain regions tend to communicate locally within a finer-scale micro-organization [Borgers et al., 2005; Fries et al., 2007; Berens et al., 2008]. In addition, S1 cortex is a cortical region receiving a convergence of anatomical connections from structures in the cortico-thalamic and cortico-cortical loops [Lin et al., 1979; Iwamura, 1998]. Low frequency LFP signals may arise in a cortico-thalamic feedback loop [Berens et al., 2008], while high frequency LFPs probably are generated by pyramidal cells and interneurons within local cortical microcircuits [Mann et al., 2005; Cardin et al., 2009].

Sliding window technique is one of the most commonly used approach to estimate variations in fMRI functional correlations between dynamic signals, however, apparent variations over time may also arise from stationary signals when the sample duration is finite. While stationary models replicate several features of real data, we showed that a closer representation of the behavior of resting-state data acquired from S1 in new world monkeys is obtained only when

an underlying dynamic or non-stationary correlation is introduced. This suggests that dynamic changes in resting-state connectivity within the primary somatosensory cortex of non-human primates are not artifacts of limited sampling duration. The spectral decomposition analysis demonstrates that coherences of low frequency (1-15 Hz) LFP signals change significantly faster over time than those of high frequency (15-150 Hz) LFP signals. Moreover, the Markov model-based approach shows that the dynamic changes of BOLD functional connectivity behave more closely to those of LFP low frequency coherence than those of high frequency coherence.

These results suggest that submillimeter resolution fMRI at high magnetic field has the ability to delineate brain activity at the columnar level, and resting state BOLD dynamic connectivity are reflective more of low frequency LFP coherence than high frequency LFP coherence.

Future direction

The relationship between BOLD and infra-slow LFP signals

Several previous studies of fMRI-electrophysiology in animal models have simultaneously recorded the resting state BOLD signals and underlying neural electrophysiology data, including both LFPs and spike, from exactly the same anatomical locations. Our previous research found that the inter-center distance variation between BOLD and LFP modalities was approximately 0.35 mm in the S1 cortex of nonhuman primate brains. In addition to the high spatial correspondence between high-resolution fMRI and LFP, simultaneous recordings of both modalities can also provide more precise temporal relationships between fMRI and LFP than with separate experiments. Recently, there has been an increasing interest in investigating the relationship between BOLD and the corresponding frequency-specific LFP signals in distributed brain regions during resting state. While some studies report that lower frequency band fluctuations have the strongest relationship to changes in BOLD signals, other evidence have shown that the oscillations in high frequency LFP signals predominantly contribute to the BOLD signal variations. Moreover, some researchers have hypothesized that resting state BOLD signals between 0.01-0.1 Hz directly correlate to variations in the corresponding underlying neuronal signal frequency range and that infra-slow LFP signals below 1 Hz contribute the most to resting state BOLD signals [Pan et al., 2011; Thompson et al., 2015]. In order to acquire infra-slow LFP signals, glass electrodes with silver-silver chloride leads need to be inserted in the cranial regions of interest since traditional metal electrodes can suffer from signal drifting issues below 1 Hz. In addition, deep anesthesia using isoflurane or dexmedetomidine during LFP signal recording can also help stabilize the infra-slow LFP signals. However, evidence has also shown that anesthesia levels and agents can change the relationship between resting state fMRI signal fluctuations and electrophysiological signal in various ways and even in different frequency bands [Lu et al., 2007; Hutchison et al., 2014; Wu et al., 2016]. As such, the relationship between modalities needs to be interpreted with great caution with the consideration that BOLD and LFP signals are both affected by physiological conditions. For these reasons, the spatial and temporal relationships between BOLD and simultaneous infra-slow LFP signals in both stimulation and resting states require further study.

Laminar profiles of BOLD and LFP in stimulation and resting states

The cerebral cortex displays a laminar structure and the analysis of spontaneous fluctuations in neuronal activity in various cortical layers with different depths is a crucial aspect for understanding the intrinsic functional architecture of the brain. Evidence has shown that information is processed by populations of neurons in multi-layered neural circuits [Thomson and Bannister, 2003]. Different types of neurons can cross communicate between different cortical regions and across distributed cortical layers. For example, the primary somatosensory (S1) cortex is known to have six horizontal laminae which are grouped into three classes: supra-granular layers (I-III), a granular layer (IV), and two infra-granular layers (V-VI). In each layer, the percentages of type of neurons are different, and therefore the neuronal oscillation generators can be different and lead to distinct functional roles. However, in this thesis, the slice thickness of all BOLD images is 2 mm and almost covers the entire six horizontal laminae in S1 cortex of new world monkeys.

Recently, there has been an increasing interest for investigating cortical circuits using resting state layer-specific BOLD fMRI with high resolution in both human and animal studies [Chen et al., 2013; Huber et al., 2015; Chen et al., 2017]. Several electrophysiological studies have shown that frequency-specific LFP neuronal oscillation generators are present in different cortical layers. For example, it has been shown that delta (1-4 Hz) and alpha (9-14 Hz) oscillations have strong sources in the superficial layers. Additionally, it was found that even with high resolution BOLD functional images at high field strength, the spatial sensitivity of BOLD signals would decrease due to the contribution of large vessels and could potentially lead to a loss or mix of detailed information regarding the underlying neural activity in a laminar structure. Several studies have pointed out that large vessels are most likely located on the superficial layers of the cortical cortex and have speculated that the main contribution to both measured BOLD activations and resting state correlations could be from these large vessels. With the improvement of imaging spatial resolution, several studies have demonstrated that resting state fMRI (e.g., BOLD, CBV) signals are sensitive at resolving layer-specific functional connectivity [Chen et al., 2017; Rockland, K.S., 2017; Huber et al., 2017; Petridou and Siero, 2017], and can detect and analyze layer-specific functional connectivity differences at very high (submillimeter) resolution in both human and animal studies (e.g., $0.7 \times 0.7 \times 1$ mm^3 resolution for humans at 7 T, $0.5 \times 0.5 \times 0.8$ mm^3 resolution for nonhuman primates at 9.4 T). It is worth investigating the laminar profile of fMRI (both BOLD and CBV) and LFP signals in different frequency ranges in order to better

understand the spatial and temporal relationships between cortical layer-specific BOLD signals and their corresponding electrophysiological signatures.

References

Berens, P., Keliris, G.A., Ecker, A.S., Logothetis, N.K. and Tolias, A.S. (2008) Feature selectivity of the gamma-band of the local field potential in primate primary visual cortex. *Front Neurosci.,* **2**, 199-207.

Borgers, C., Epstein, S. and Kopell, N.J. (2005) Background gamma rhythmicity and attention in cortical local circuits: a computational study. *Proc. Natl. Acad. Sci. USA,* **102**, 7002–7.

Cardin, J.A., Carlen, M., Meletis, K., Knoblich, U., Zhang, F., Deisseroth, K., Tsai, L. and Moore, C.I. (2009) Driving fast-spiking cells induces gamma rhythm and controls sensory responses. *Nature,* **459**, 663- 667.

Chen, G., Wang F., Gore J.C. and Roe A.W. (2013) Layer-specific BOLD activation in awake monkey V1 revealed by ultra-high spatial resolution functional magnetic resonance imaging. *Neuroimage,* **64**, 147-55.

Chen, L.M., Yang, P.F., Wang, F., Mishra, A., Shi, Z., Wu, R., Wu, T.L., Wilson, G.H., Ding, Z. and Gore, J.C. (2017) Biophysical and neural basis of resting state functional connectivity: evidence from non-human primates. *Magn Reson Imaging,* **39**, 71–81.

Fries, P., Nikolic, D. and Singer, W. (2007) The gamma cycle. *Trends in Neurosciences,* **30**, 309-316.

Huber, L., Goense, J., Kennerley, A.J., Trampel, R., Guidi, M., Reimer, E., Ivanov, D., Neef, N., Gauthier, C.J., Turner, R. and Moller, H.E. (2015) Cortical lamina-dependent blood volume changes in human brain at 7 T. *Neuroimage,* **107**, 23-33.

Huber, L., Uludag, K. and Moller, H.E. (2017) Non-BOLD contrast for laminar fMRI in humans: CBF, CBV and $CMRO_2$. *NeuroImage,* 2017, in press.

Hutchison, R.M., Hutchison, M., Manning, K.Y., Menon, R.S. and Everling, S. (2014). Isoflurane induces dose-dependent alterations in the cortical connectivity profiles and dynamic properties of the brain's functional architecture. *Hum. Brain Mapp*., **35**, 5754–5775.

Iwamura, Y. (1998) Hierarchical somatosensory processing. *Curr Opin Neurobiol.,* **8**, 522–528.

Lin, C.S., Merzenich, M.M., Sur, M. and Kaas, J.H. (1979) Connections of Areas 3b and 1 of the parieta) somatosenaory strrp with the ventroposterior nucleus in the owl monkey (Aotus tricirgatus). *J. comp. Neurol.,* **185**, 355-371.

Lu, H., Zuo, Y., Gu, H., Waltz, J.A., Zhan, W., Scholl, C.A., Rea, W., Yang, Y. and Stein, E.A. (2007) Synchronized delta oscillations correlate with the resting-state functional MRI signal. *Proc Natl Acad Sci USA,* **104**, 18265–18269.

Mann, E.O., Radcliffe, C.A. and Paulsen, O. (2005) Hippocampal gamma-frequency oscillations: from interneurones to pyramidal cells, and back. *J Physiol.,* **562**, 55-63.

Pan, W.J., Thompson, G., Magnuson, M., Majeed, W., Jaeger, D. and Keilholz, S. (2011) Broadband local field potentials correlate with spontaneous fluctuations in functional magnetic resonance imaging signals in the rat somatosensory cortex under isoflurane anesthesia. *Brain Connect.,* **1**, 119–131.

Petridou, N. and Siero, J.C.W. (2017) Laminar fMRI: What can the time domain tell us? *NeuroImage,* 2017, in press.

Rockland, K.S. (2017) What do we know about laminar connectivity? *NeuroImage,* 2017, in press.

Steriade, M. (2006) Grouping of brain rhythms in corticothalamic systems. *Neuroscience,* **137**, 1087-1106.

Steriade, M., McCormick, D. and Sejnowski, T. (1993) Thalamocortical oscillations in the sleeping and aroused brain. *Science,* **262**, 679-685.

Thompson, G.J., Pan, W-J. and Keilholz, S.D. (2015) Different dynamic resting state fMRI patterns are linked to different frequencies of neural activity. *Journal of Neurophysiology*, **114**, 114-24.

Thomson, A.M. and Bannister, A.P. (2003) Inter-laminar connections in the neocortex. *Cereb Cortex,* **13**, 5-14.

Wu, T.L., Mishra, A., Wang, F., Yang, P.F., Gore, J.C. and Chen, L.M. (2016) Effects of isoflurane anesthesia on resting-state fMRI signals and functional connectivity within primary somatosensory cortex of monkeys. *Brain and behavior*, **6**, 12.